ECal/MPD

Dubna, January 2018, Rev. 2.1

MPD NICA

Technical Design Report

of the

Electromagnetic calorimeter (ECal)

Dubna 2018

Contents

1 Introduction....4

1.1 The NICA/MPD experiment....4

1.2 Physics motivation....4

1.2.1 Probing chiral symmetry restoration in A+A....5

1.2.2 Electromagnetic probes : study of flow signal....7

1.2.3 Electromagnetic probes : correlations....8

1.3 General design considerations....9

1.3.1 Basic requirements....10

1.3.2 Required time resolution of the ECal system of MPD....18

2 ECal performances....22

2.1 Charged particle reconstruction....22

2.2 Photons reconstruction....25

2.3 New geometry - projective....35

3 ECal design....39

3.1 ECal module....41

3.2 FE electronics....46

3.3 Slow Control....47

3.3.1 High Voltage....47

2.3.2 LED Generator....49

3.3.3 Temperature and pressure....50

3.4 Power consumption and cooling....50

4 Test results....52

4.1 Calibration....52

4.3 Energy resolution....56

4.4 Time resolution....60

4.5 Coordinate resolution....61

4.6 Heat extraction.....62
5 Projective geometry.....64
5.1 Fundamentals of the Design of the ECal.....64
5.2 Block assembling.....70
5.3 Sector assembling.....73
6 Time table and cost estimation.....76
. Reference.....78

1 Introduction

Investigation of hot and dense baryonic matter is a challenging task in modern physics. It provides information on the in-medium properties of hadrons and nuclear matter equation of state, allows a search for possible manifestations of the deconfinement and/or chiral symmetry restoration, phase transition, mixed phase and critical end point, and sheds light on the evolution of the Early Universe and formation of neutron stars.

1.1 The NICA/MPD experiment

An essential part of the JINR scientific program resulted from many discussions in view of the Dubna Nuclotron upgrade is dedicated to the study of hot and dense baryonic matter. Realization of this ambitious goal is related to the construction of a new JINR accelerator complex – the Nuclotron-based Ion Collider fAcility (NICA) to provide collisions of heavy-ions over a wide range of atomic masses, from Au+Au collisions at a centre-of-mass energy of $\sqrt{s_{NN}}$ = 11GeV (for Au^{79+}) and an average luminosity of $L = 10^{27}cm^{-2}s^{-1}$, to proton-proton collisions with $\sqrt{s_{PP}}$ = 20GeV and $L \approx 10^{30}cm^{-2}s^{-1}$.

Two interaction points are foreseen at the NICA collider, which provide a possibility for two detectors to operate simultaneously. One of these detectors, the MultiPurpose Detector (MPD), is optimized for the study of properties of hot and dense matter in heavy-ion collisions and, in particular, for the search a manifestation of possible deconfinement and/or chiral symmetry restoration phase transitions, critical end-point and mixed quark-hadron phase [1].

1.2 Physics motivation

The main goal of the NICA heavy-ion program at JINR is an experimental investigation of the properties of nuclear matter in the energy region of the maximum baryonic density [2-4]. Lattice QCD calculations predict the deconfinement phase transition to be happened at high enough energy densities achieved in head-on collisions of relativistic nuclei. Recent experimental data on hadron

production at SPS [5] indicate that this transition may happen within the energy range of the NICA collider (4-11AGeV). Among the observables that give insight into the state of matter created in heavy-ion interactions electromagnetic probes are very attractive because of two reasons: 1) direct photons and lepton pairs are produced over the entire evolution of the reaction from the initial collision until the hadronization process and freeze-out, thus all stages of the fireball evolution can be probed; 2) once produced the gammas and leptons escape the interaction region unaffected by subsequent strong interactions carrying to the detectors information about the properties of the medium at the time of their creation.

All models of QGP formation require information about the rate of its thermalization, thus, of particular interest is the extent to which the measured particle yields show equilibration. The degree of equilibrium can be tested by analyzing particle abundances and ratios, while the transverse distributions probe the temperature evolution in the source from a high temperature deconfinement phase to the decoupling stage at the thermal freeze-out. Therefore, photon and dilepton rates, transverse momentum and azimuthal angle distributions, as well as correlations of $e/\gamma/\pi^o$ provide us valuable (and complement to hadron probes) information about the nature, bulk properties and sizes of the matter created in heavy-ion collisions.

1.2.1 Probing chiral symmetry restoration in A+A

The deconfinement phase transition in heavy-ion collisions can be accomplished by partial restoration of the chiral symmetry [6, 7]. A prompt signal for the chiral symmetry restoration in A+A interactions could come from domains of disoriented chiral condensate. The most likely origin of a coherent low-energy excitation of the pion field would be a collective isosinglet excitation of the Goldstone boson field (σ, π) associated with the spontaneous breaking of chiral symmetry describing as a nonlinear wave in the sigma model [8, 9]. The latter corresponds to coherent excitations of the pion field decaying into neutral and charged pions with the probability distribution with quite large deviations from isospin neutrality. Thus, a very strong signature of the chiral phase transition would be pion charge ratios $N_{\pi^o}/N_{\pi^\pm}$ significantly different from 1/3. Such a scenario is more likely to occur

in a relativistic heavy-ion collision, because the chiral transition is accompanied by a large change in the energy density. Thus, in order to probe chiral symmetry restoration, the MPD detector will capable to measure all three pion species.

In addition, partial restoration of the chiral symmetry manifests itself in modifications of hadronic spectral functions in dense hadronic matter. The correlated electron-positron pairs (dileptons) from decays of vector mesons (ρ, ω, φ) are the best candidates to study such in-medium modifications since they escape the interaction region unaffected by subsequent strong interactions. Production of low-mass dileptons in heavy-ion collisions has been studied at the CERN-SPS at center-of-mass energy of 8.8, 17 and 19AGeV [10-14]. The CERES Collaboration has observed a strong excess in the invariant-mass spectrum of electron-positron pairs in the region dileptons invariant mass $0.2<M_{e^+e^-}<0.7$ [GeV/c^2] above the expectations from the superposition of the known hadron decay channels based on their vacuum properties. At the Brookhaven Lab., the PHENIX [15] and STAR [16] experiments measured the dilepton production from the top RHIC energy 200AGeV down to the top SPS energy and also reported on the excess in the dilepton spectra below the w-meson. The dilepton spectra from the DLS [17] and HADES [18] experiments taken at much lower incident energies (1-2AGeV) in smaller colliding systems (C+C and Ar+Ar) are well described by a superposition of elementary nucleon-nucleon collisions, in contrast to higher energies and heavier nuclei.

Until now, no dilepton measurements have been performed at center-of-mass energies of several GeV and the dilepton program at NICA is aimed to close this gap. The range of collision energies from 4 to 11AGeV is very promising for dilepton studies since the effect of modifications is expected to be sensitive to the baryon density, while the latter happens to reach the maximum in central Au+Au collisions at NICA [19].

The experimental study of dileptons in heavy-ion collisions is a challenging task. The main difficulty is a huge combinatorial background of uncorrelated lepton pairs which mainly come from π^o Dalitz decays and photon conversion in the detector material. A special attention should be paid to reduce this background as much as possible. The main task for MPD ECal is to reduce the false

identification of hadrons as electrons(positrons) to large extent.

1.2.2 Electromagnetic probes : study of flow signal

An important probe in heavy-ion collisions providing information about the nature of nuclear matter is flow. Azimuthal anisotropy (relative to the reaction event plane) in the particle emission have been studying as a function of collision energy, event centrality, and transverse momentum provide insight into the details of nuclear matter equation of state, its transport properties and velocity of sound. Using π^0 as a probe in the flow analysis has an advantage that neutral pions are easy to reconstruct at any Pt. Moreover, the strength of the flow signal for π^0 (or, even, for gammas from π^0-decays) is the same as for charged pions (see Figure 1.2.2.1).

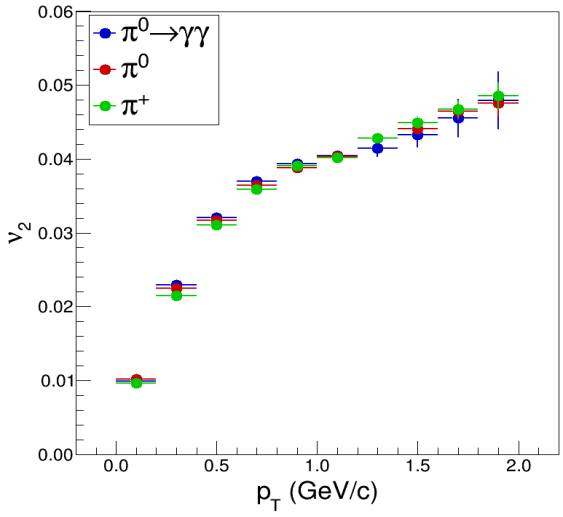

Figure 1.2.2.1: *Elliptic flow v2 as a function of Pt from mid-central Au+Au collisions (UrQMD model) for charged pions, π^o and photons from π^o decays.*

In addition, in a non-central heavy-ion collision the charged spectators produce a strong magnetic field which interacts with the quark-gluon matter created in the reaction and might result in the phenomena of electric charge separation along the magnetic field axis - Chiral Magnetic Effect (CME) [20]. In addition, if the deconfinement phase is accompanied by a chiral symmetry restoration, the separation of chiral charges (characterizing left or right handedness) along the axis of the magnetic field is expected to be present in the case of finite density of electric charges. In this case, a propagation of chiral charge density in a long wave-length hydrodynamic mode, i.e. Chiral

Magnetic Wave (CMW), theoretically expected to modify the elliptic flow of charged hadrons leading to an increase (decrease) of the v2 parameter of negative (positive) particles [21]. Recently, the STAR Collaboration at RHIC has measured the sizable difference in the elliptic flow parameter v2 between π^+ and π^- on an event-by-event basis [22]. Despite of interpretation of these observations as a result of CMW, the measurements below 19GeV are suffering of low statistics and are not convincing. Moreover, the effect is measured on top of the v2 'base line' which may be different between π^+ and π^- because of several other possible physical mechanisms [23, 24]. We suggest perform high statistics measurements of the elliptic flow coefficients for all pion species (π^+, π^-, π^0) at NICA energies to overcome both the difficulties mentioned above. Reconstructed via the ECal information π^0's and their azimuthal asymmetry will be used as a 'base line' in CMW-effect studies. We plan to perform a detailed study of the azimuthal distributions for charged particles as well as for neutral pions and gammas. For this, the MPD ECal must provide azimuthal symmetry and high granularity.

1.2.3 Electromagnetic probes : correlations

Interferometry of two identical particles is widely employed to get insight into the space-time structure of the interaction zone: this technique allows measure the size and lifetime of the fireball. Results on hadron correlations in A+A were obtained over the region from SIS to LHC energies (for a review see [25] and references therein). However, strongly interacting probes are mainly appear in the late stage of the fireball evolution when the dense and hot nuclear matter is getting cooler and more dilute. In contrast, photon correlations carry information about the whole story of the source evolution, since gammas are produced starting from the very early moments of the reaction and suffer practically no interactions in the interior of the medium. Thus, direct photons emitted from the early hot phase of the collision and their correlations serve as a valuable QGP signature and allow to obtain an image of the early hot and dense phase in heavy-ion collisions [26-28]. In MPD photons can be reconstructed in two ways: by using the gamma-conversion method in the material or by measuring the flux of gammas in the ECAL. Thus, in the suggested correlation analysis three

different combinations of photon pairs are possible: ECal-ECal, conversion-conversion, and ECal-conversion. The Correlation Function (CF) for the photon pairs reconstructed in ECAL can be affected by detector "non-ideality" (ECal segmentation, thresholds, etc.) and analysis cut-offs (acceptance, quality selections, etc.), while correlations of photons from the conversion process depends heavily on the tracking details in MPD (for example, on the 2-track resolution). We suppose that combining conversion photons with those from ECal the systematic errors imposed by the experimental 2-track resolution and CF Pt-cut (+other detector issues) can be eliminated (or compensated) because two different detector parts will be used in the analysis.

In summary, the particular goals of the MPD ECal are to measure of spatial positions and energy of photons and electrons in order to:

- obtain the measure of the yields, transverse momentum and azimuthal angle distributions of photons, π^0- (and eta-mesons) and electron-positron pairs produced in central as well as peripheral heavy-ion collisions at an energy of 4-11AGeV;
- study in detail the effects of collective flow of electromagnetic probes in heavy-ion collisions;
- search for femtoscopic correlation effects in two- (and four-) photon distributions;
- obtain new experimental data on the yields of neutral mesons in Au+Au collisions from two-, three-, and four-photon invariant mass distributions;
- search for thermal and direct photon emission in Au+Au collisions at NICA (or define its upper limit).

1.3 General design considerations

The calorimeter should satisfy many criteria of different nature and significance. Most important of requirements are coming from the of physics tasks which we are going to study with the use of calorimeter. Technological capabilities of the modern experimental physics should be estimated and taken into account in choosing type of calorimeter to be built. The price and possibility of realization should be taken into account as well to make project realistic.

1.3.1 Basic requirements

The expected high multiplicity environment (Figure 1.3.1.1) implies the high segmentation of the calorimeter, large enough distance to the vertex, and use of a dense active medium with the small Moli'ere radius. To have an adequate space resolution and to allow the separation of overlapping showers, the transverse cell size should be of the order of the Moli'ere radius. Reliable reconstruction of photons and mesons is only possible at small shower overlaps. The particle occupancy should not exceed 5% to determine the photon reconstruction efficiency with high accuracy. Above-mentioned requirements are the common ones and can be satisfied with the help of different types of calorimeters. But there are some requirements which reject out many solutions

- Calorimeter must be able to operate in the magnetic field up to 0,5T − PM is difficult to use.
- Time resolution should be at least below 1ns to cut pile-up and noise events and close to 100 ps to participate in the time of-flight particle identification − most of crystals with reasonable price are much slow.

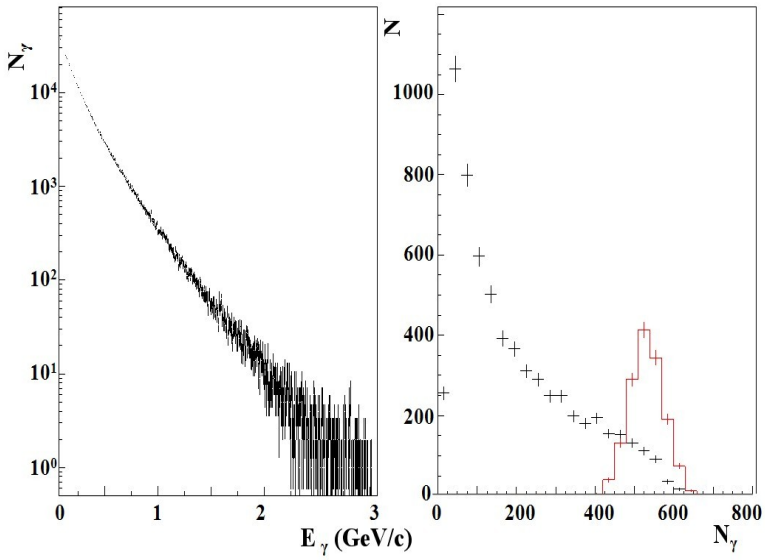

Figure 1.3.1.1: *The energy spectrum of photons (left panel) and photon multiplicity distribution (right panel) in the central (red) and minimum bias (black) Au+Au collision (9 AGeV).*

Due to the last requirements, already at this stage of a choice, our attention became concentrated on the "shashlyk" type calorimeter with MAPD photons detectors [29].

MC study is done on the basis of the UrQMD event generator to fix which is the energy

spectrum and multiplicity of the photons is expected in the heavy ions collisions on the NICA complex (Figure 1.3.1.1).

Full MPD Monte Carlo simulation was used to estimate average occupancy of MPD barrel ECal detector. Detector sell of 4x4 cm^2 was used. As it is clear from the plot (Figure 1.3.1.2) ECal occupancy for the most complicated for the detection-reconstruction events (Au+Au 11 AGeV) is very high (about 20%). In such condition increase of the detector sell size above 4x4 cm^2 will complicate already difficult situation with events detection-reconstruction. MC simulation of the same events with the ECal when tower size is increased to the 6x6 cm^2 shows increase of occupancy up to 45% (Figure 1.3.1.3) which is totally unacceptable. Further reduction of the cell size may help in event reconstruction even in the case of Moli'ere radius of about 62 mm, but is unacceptable due to huge increase in the cost of ECal. Thus, the choice of ECal cell size of 4x4 we believe is optimal.

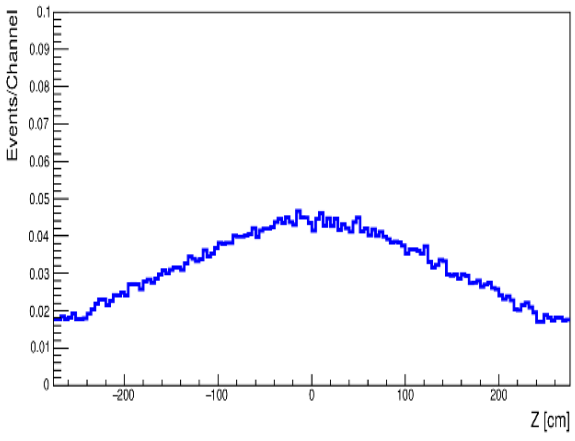

Figure 1.3.1.2: *Average number of particles per channel for the barrel part of MPD ECal detector with 4×4cm² detector element. UrQMD Au+Au collision, 11 AGeV, central events .*

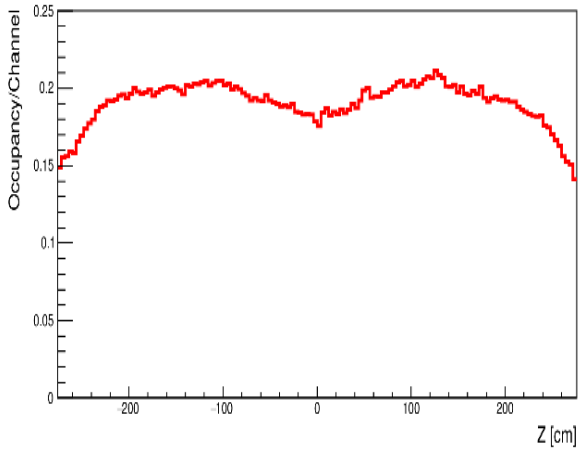

Figure 1.3.1.2: *Average occupancy (charged particles + electromagnetic showers) per channel for the barrel part of MPD ECal detector with 4×4cm² detector element. UrQMD Au+Au collision, 11 AGeV, central events .*

Thus, the choice of ECal cell size of 4x4 we believe is optimal.

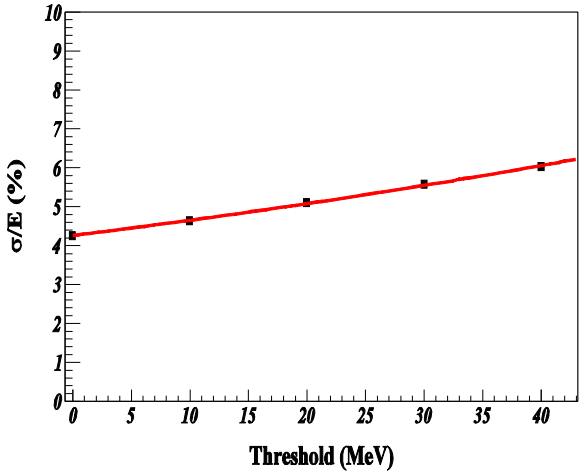

Figure 1.3.1.4: *Energy resolution vs threshold (e^- 1GeV).*

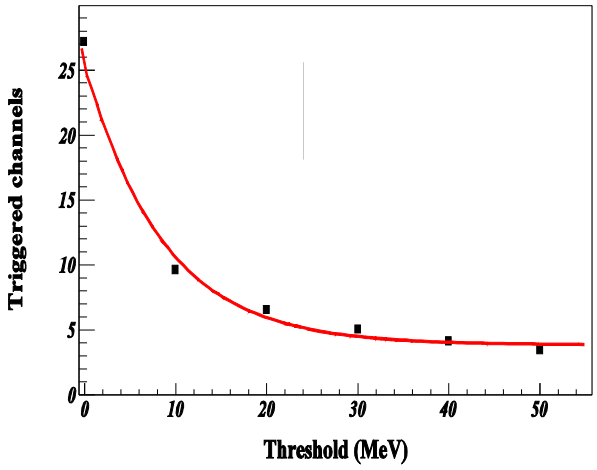

Figure 1.3.1.5: *Number of cells vs threshold (e^- 1GeV).*

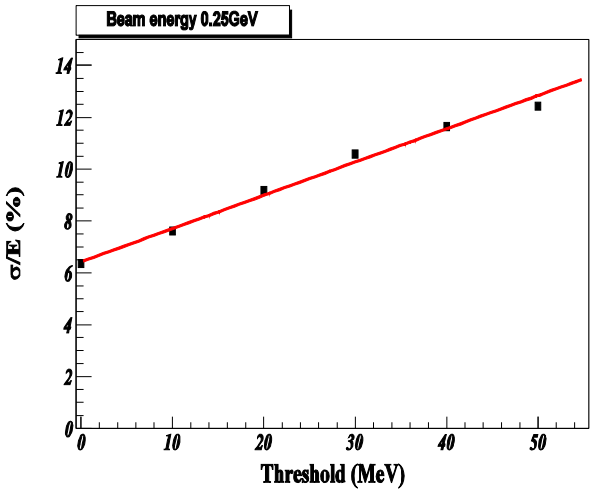

Figure 1.3.1.6: *Energy resolution vs threshold (e^- 0.25GeV).*

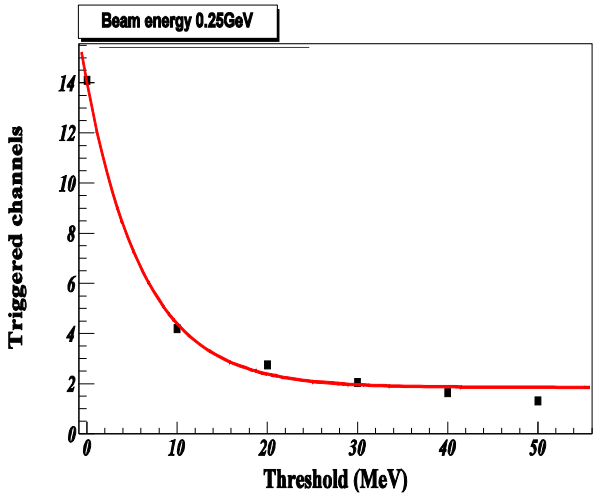

Figure 1.3.1.7: *Number of cells vs threshold (e^- 0.25GeV)*

The special efforts in the software together with threshold tuning should be done to reach effective and accurate registration of electromagnetic showers in this high particle multiplicity environment. The choice of registration threshold is a compromise between energy resolution and the number of active cells. Obviously (Figure 1.3.1.4) that to reach high energy resolution we have to collect all hits (even very small) that means low registration threshold. Low registration threshold, in turn, leads to the big number of cells involved N vs Th (Figure 1.3.1.5) .

The energy resolution of the photon detector is a critical point in the conditions of high photon multiplicity. Achievement of the best possible energy resolution (at least of 5% for the 1GeV

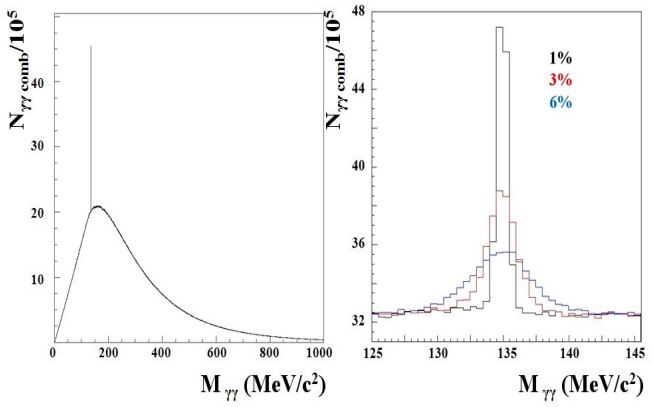

Figure 1.3.1.8: *π^0 reconstruction in the intermediate π^0 transverse momentum regions for different photon detector energy resolutions. Left panel – ideal detector. Au+Au collision (at $\sqrt{s_{NN}}$ = 9 AGeV).*

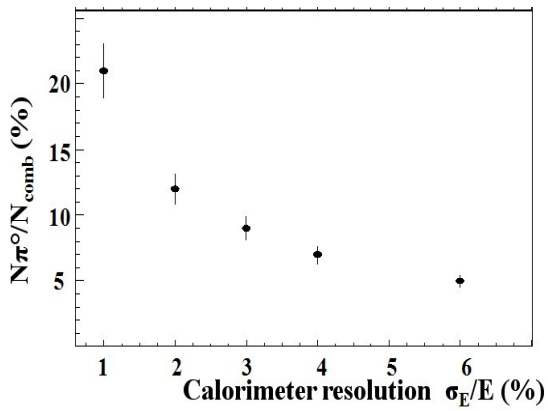

Figure 1.3.1.9: *The ratio of number of reconstructed π^0 mesons to a number of events from combinatorial background vs the calorimeter energy resolution.*

photons) is highly desirable. This can be illustrated on the example of π^0 reconstruction and measurements of π^0 flux (Figure 1.3.1.8 and Figure 1.3.1.9).

According to the KOPIO study [30], sampling ratio, i.e. the relation between thicknesses of lead and scintillator tiles, dominates in the energy resolution of the "shashlyk" . But, its value is smaller than the cumulative effect of other contributions. So, photostatistics and nonuniformity of light collections add to the total energy resolution 2.1%/√E and 1.8%/√E, respectively. And, many attention should be paid to improving the quality of scintillator, optical and mechanical, and to selecting the photo-detector with higher quantum efficiency.

Unfortunately, space available for the ECal in the MPD is rather small (40 cm for the active part) what a priori does unattainable the maximum energy resolution. Shower leakage even for the low energy particles is rather big (Figure 1.3.1.10).

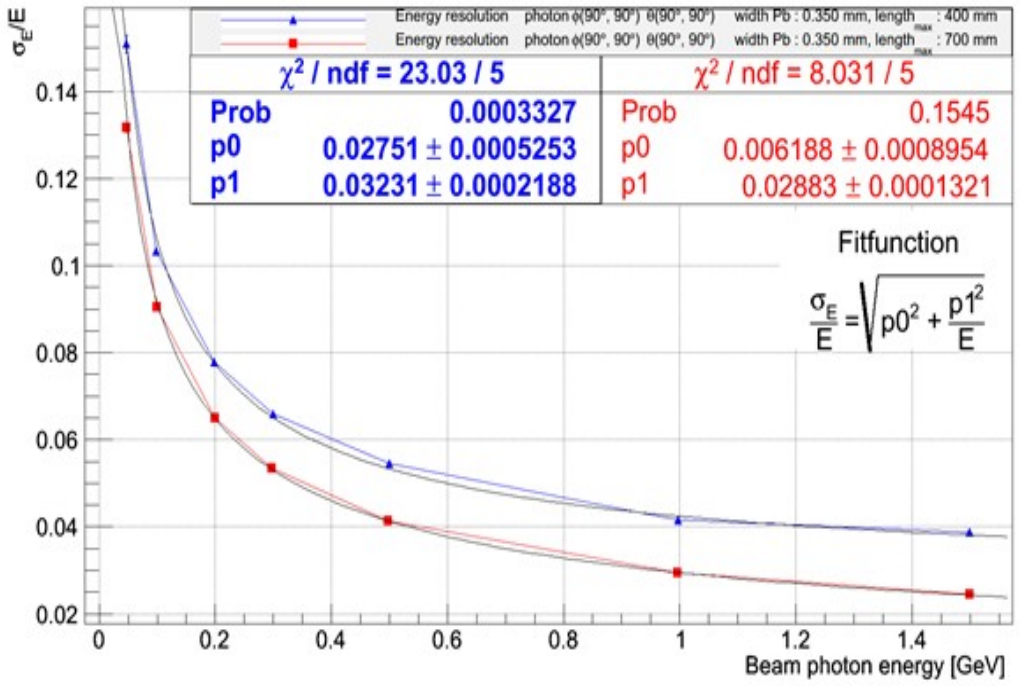

Figure 1.3.1.10: *Energy resolutions of the calorimeter with two different lengths of the modules – 400mm and 700mm.*

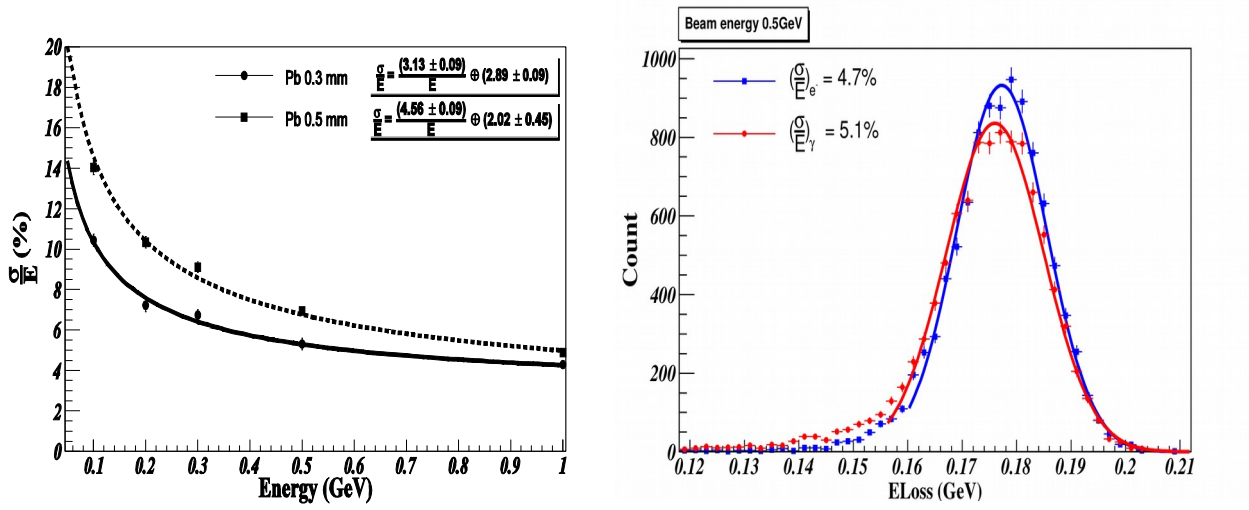

Figure 1.3.1.11: *Comparison of energy resolution for modules with lead thickness 0.5mm and 0.3mm (left). The ECal response from electron and photons (right).*

In this situation sampling study was done to choose optimal lead thickness - increase of lead thickness reduce shower leakage but increase a sampling contribution to the energy resolution and vice versa. Comparison of energy resolution for 0.5mm lead plate and 0.3mm one (Figure 1.3.1.11) is a clear illustration of this feature. Lead plate thickness have been fixed as 0.3mm because further reduction of this value will make calorimeter too transparent.

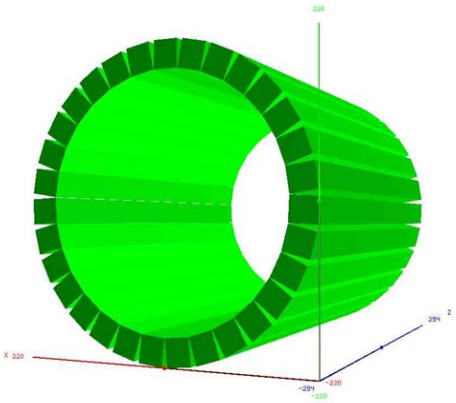

Figure 1.3.1.12: *Geometry of ECal (rectangular modules).*

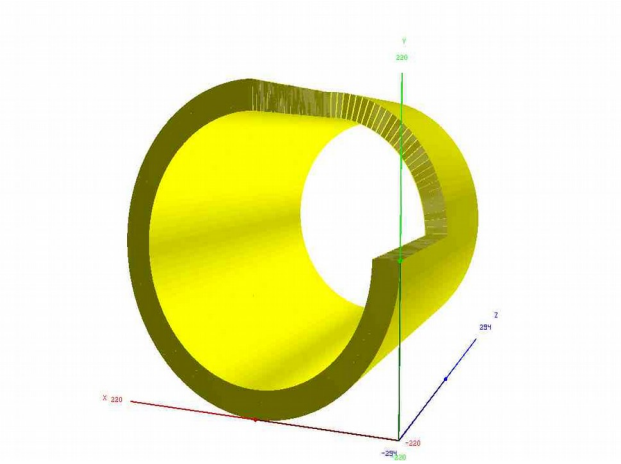

Figure 1.3.1.13: *Geometry of ECal (trapezoidal modules).*

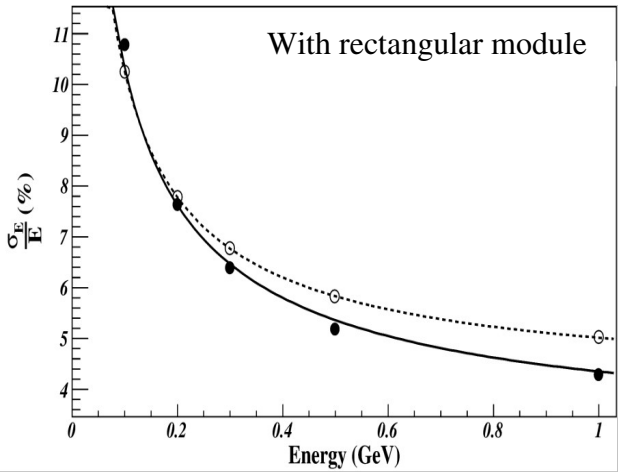

Figure 1.3.1.14: *Comparison of energy resolution when particles hit in center of the rectangular module and particles flow randomly distributed in the barrel. The results from used photons.*

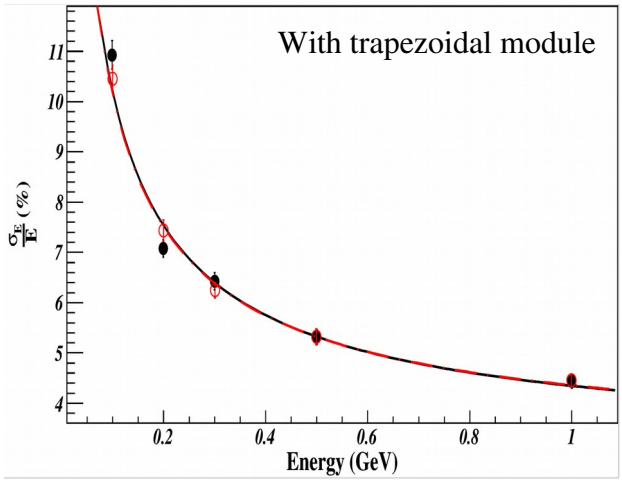

Figure 1.3.1.15: *Comparison of energy resolution when particles hit in center of module and particles flow randomly distributed in the barrel. The results from used photons.*

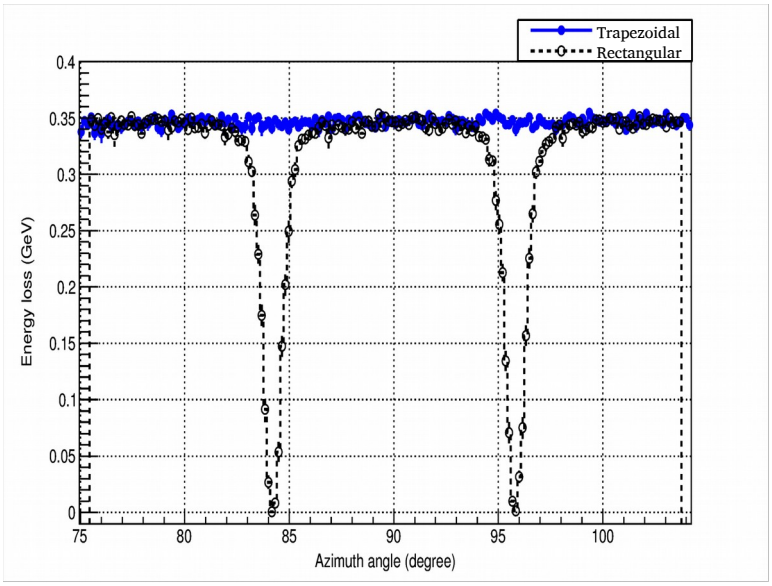

Figure 1.3.1.16: *Energy resolution of the azimuth angle in the geometries composed with rectangular and trapezoidal modules.*

If the barrel part of ECal will be built from the usual square shaped modules (Figure 1.3.1.12) dead spaces between modules will certainly reduce energy resolution in average.

This effect is illustrated on figure 1.3.1.14 where MC comparison is presented of energy resolution for the case when particles hit the module in their center and when particle flow randomly distributed in the barrel.

To reduce the dead zones effect all modules will be cut from two sides at an angle 1.5 degree. After such a cut modules will have a trapeze shape in the rφ plain. This modification will significantly reduce dead zones effect (Figure 1.3.1.13 and Figure 1.3.1.15). On the figure 1.3.1.16 shows the comparison of the geometry composed of the rectangular and trapezoidal modules.

One more important factor which gives impact on the energy resolution of calorimeter is the material budget in front of ECal. This influence was studied by the MC simulation program which is using full information about all MPD sub-detectors and the distribution of the material in these sub-detectors. Certainty, effect of material leads to the degradation of the ECal energy resolution (Figure 1.3.1.17), essentially in the low energy region. This degradation is not dramatic, but it is an indication - all efforts should be done to reduce amount of material in the MPD detector. Effect of the registration threshold is very small and it can be illustrated by the π^o reconstruction efficiency

(Figure 1.3.1.18).

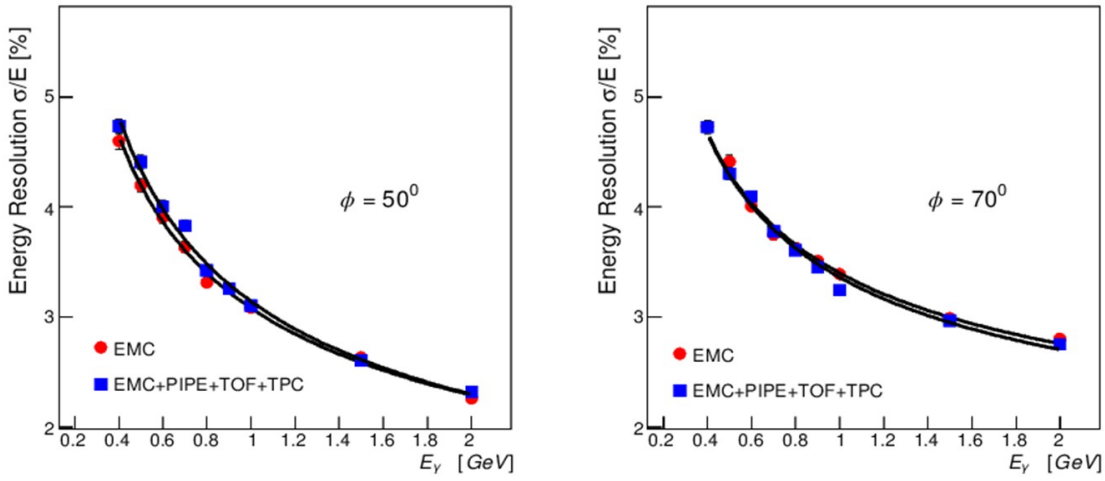

Figure 1.3.1.17: *Coordinate resolution at an azimuth angle of 50 degrees and 70 degrees.*

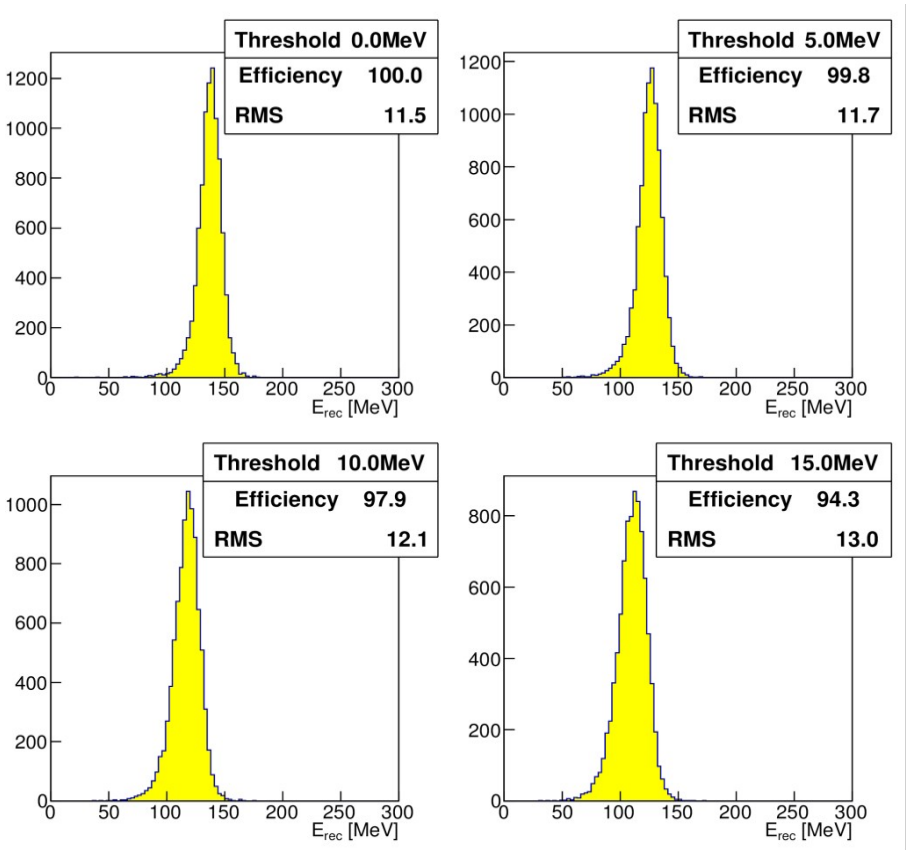

Figure 1.3.1.18: *π^0 distributions at different threshold values and calculated efficiency of registration.*

1.3.2 Required time resolution of the ECal system of MPD

Important feature of the "shashlyk" calorimeter is the possibility to make precise time measurements of the signals from the device. There are three fields where time measurements is extremely useful.

1. First, time resolution of the order of 10ns is necessary to reduce of background and pile-up noise. Simple calculations shows (which later have been confirmed by the measurements. See section 3.4) that 10ns time resolution will reduce undesirable registrations practically to zero.
2. The order of magnitude higher time resolution required for the suppression of the secondary photons from the interaction in the material of the MPD detector (Figure 1.3.2.1). Most of such photons originate from the reaction with the neutrons and arrive in the ECal with sufficient delay. Monte Carlo study shows that time resolution of the order of 1ns will be sufficient to suppress such background down to the negligible level. The task becomes complicated the fact that this 1ns time resolution should be achieved for the very soft photons (100MeV and even lower).

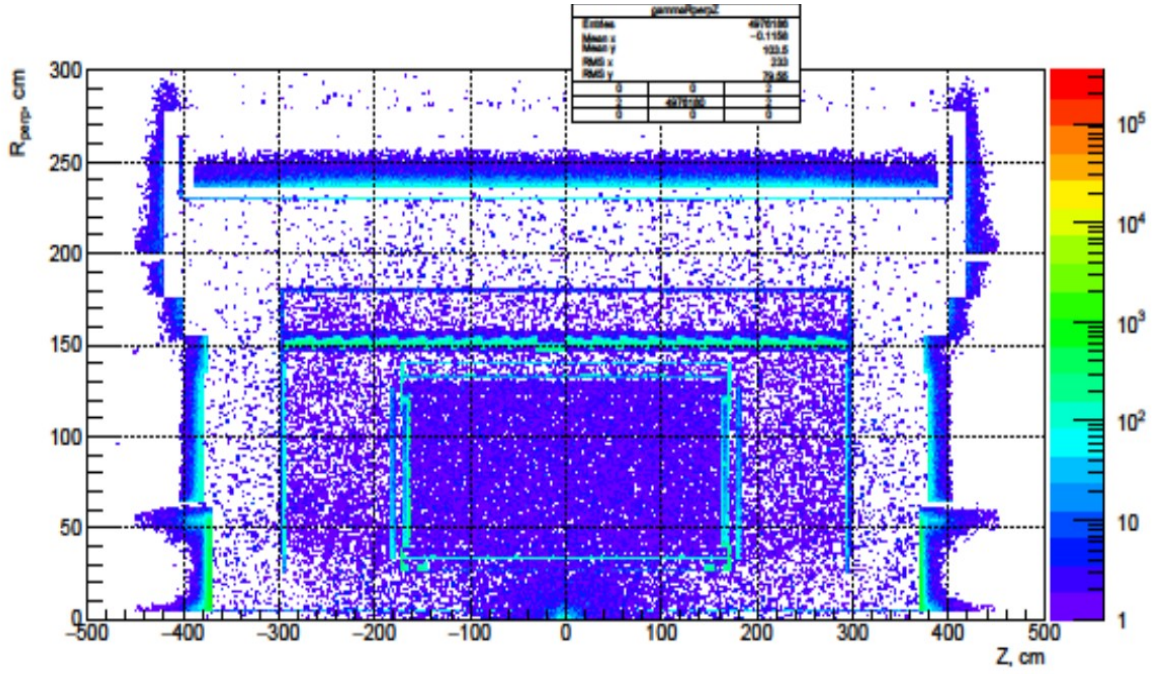

Figure 1.3.2.1: *Spatial distribution of points where photons which have been registered by a calorimeter was born.*

Using arrival time cut, which depends from the path of the photons in the detector (entry point in to the calorimeter) number of secondary photons can be significantly reduced (Figure 1.3.2.2).

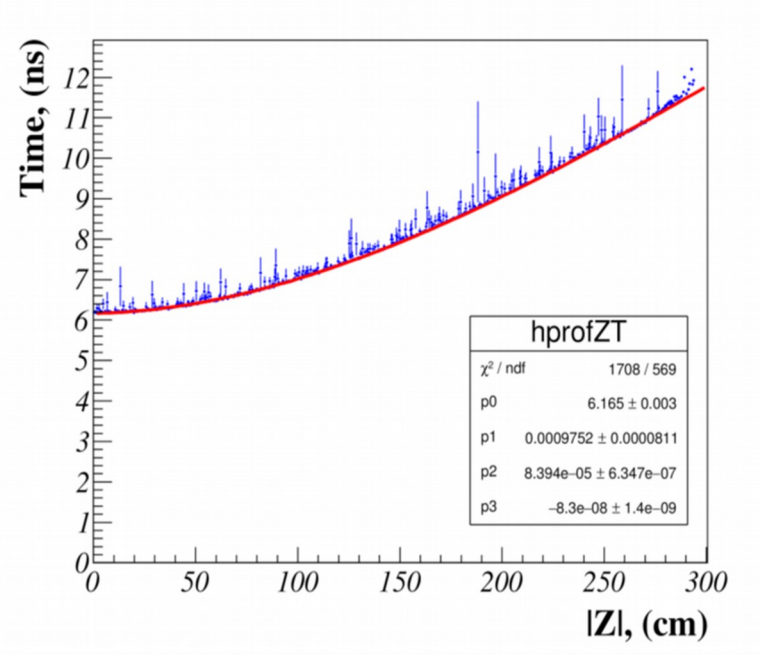

Figure 1.3.2.2: *MC results – photons arrival time vs arrival Z position.*

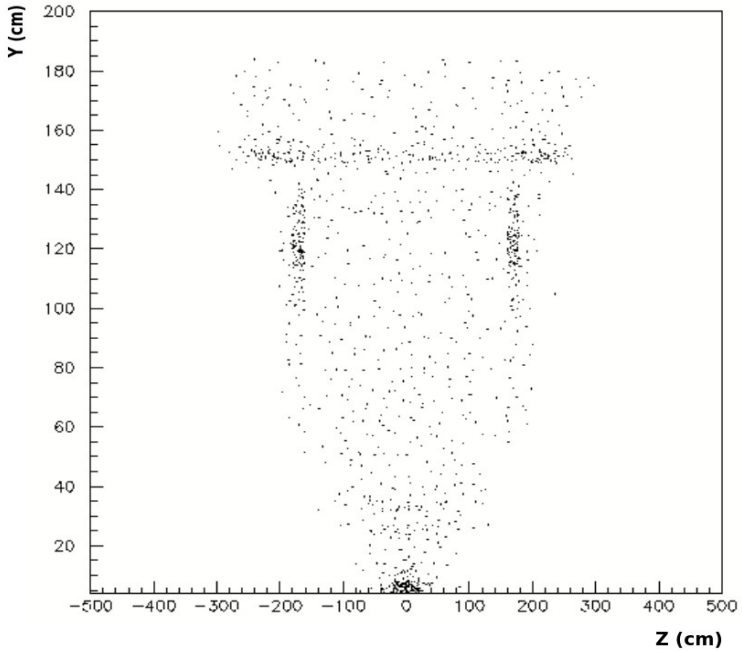

Figure 1.3.2.3: S*patial distribution of points where photons have been registreted by a calorimeter was born. After time cut.*

For the events generated by UrQMD generator for the 11GeV, Au+Au, central events, such cut reduce number of secondary photons detected by the calorimeter to the value about 3% form the total number of photons detected.

Last modification of the ECal (with 6x6mm² HAMAMATSU photo-detectors) was tested on the electron test beam at DESY and time resolution reached in those tests is batter than 1ns almost in all energy region (Figure 1.3.2.4).

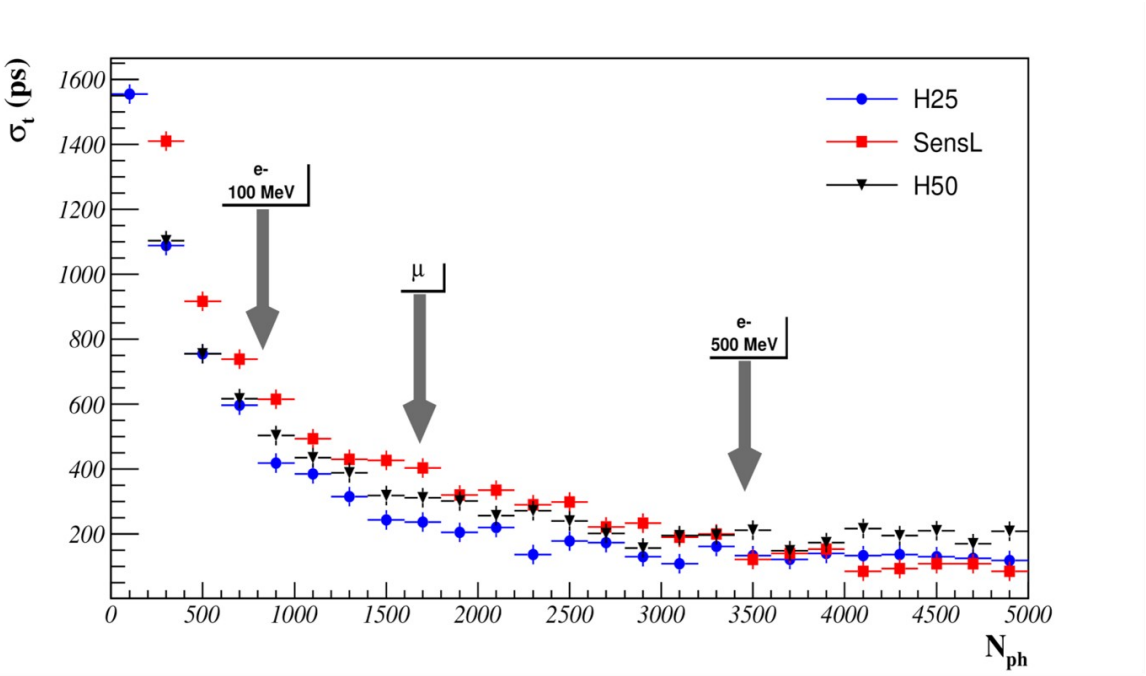

Figure 1.3.2.4: *Time resolution with new 6x6mm² photo-detectors.*

Sub-nanosecond time measurements in the ECal will allow to use this device as a time-of-flight device in the support to the main TOF detector. According KOPIO data [30] the conservative estimation of the calorimeter time resolution is:

$$\sigma_t(ps) \approx \frac{100}{\sqrt{E}(GeV)}$$

Such a time resolution have been attributed to the calorimeter and MC study of particle identification was performed. Particle identification done with the use of time measurements from the calorimeter is illustrated by the figures 1.3.2.5 and 1.3.2.6.

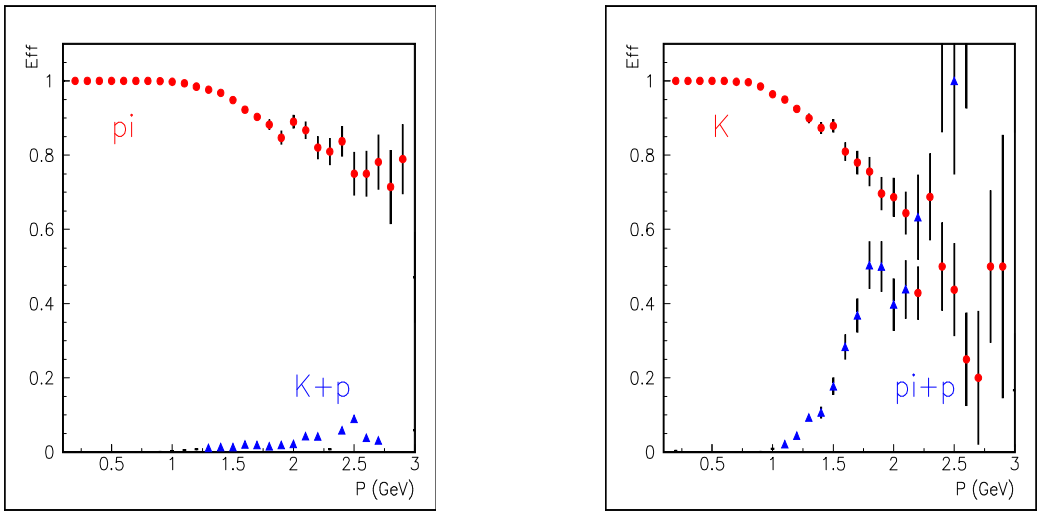

Figure 1.3.2.5: *Efficiency versus momentum: left – Separation of pions from kaons and protons; righ – Separation of kaons from pions and protons.*

Decision was taken to concentrate efforts on the first two tasks. The ECal operation in the TOF mode is possible but require not only much higher manpower efforts, but also require new /fe electronics. Such FE electronics will be more expensive and more power consuming.

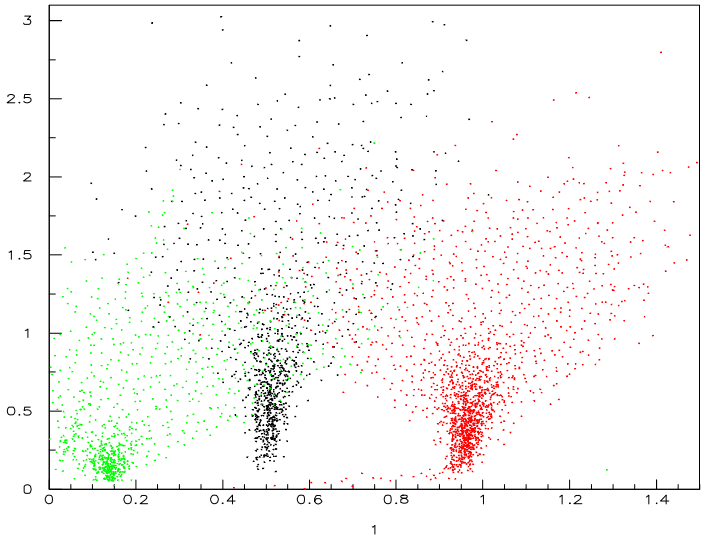

Figure 1.3.2.6: *Particle identification with the use of time measurement.*

2 ECal performances

The main goals of the calorimeter are the participation in particles identification (namely - final cleaning of the selected e+- sample) and measurements of the photons flux as well as reconstruction of some decays with participation of the photons. In these tasks final result depends on performances of all or most of MDP detectors. Some studies of the efficiency of combined event reconstruction with the use of most important MPD detectors (TPC, TOF and ECal) will be presented below.

This study was done by the Monte Carlo simulation based on the reliable description of MPD sub-detectors. MC simulation of the ECal was tested many times during beams tests at CERN and DESY and cosmic ray tests and found as a very realistic.

2.1 Charged particle reconstruction

The trajectories of charged particles inside the MPD detector are reconstructed using dedicated tracking detector - TPC. This device gives precise trajectory of the charged particle as well as its dE/dx which is used for the particle identification. The TOF detector is the dedicated device for the charged particles identification on the basis of time of flight measurements. These detectors described in the relevant chapters. To improve charged particle identification and make measurements of the flux of neutral particles (photons) the energy deposition from the charged particles in the ECal should be matched to the reconstructed trajectories.

First, hits detected in the ECal, in the correct time interval and with energy deposition higher certain threshold (10MeV) was joined into the clusters according simple rules -

1. Hits should have common border;

2. Hits should have energy deposition above threshold (10MeV);

3. Number of such hits should be higher than N_{tr} (3 hits) to form a cluster;

Then, charged particle trajectory, reconstructed in the TPC is extended into the volume of the ECal

and if some cluster fit to this track extinction then such cluster is matched with this track. One example, when charged (pion) track reliably associated with cluster in the ECal, is presented on the figure 2.1.1. Clear elongated structure presented in most of clusters. Elongation in the z direction is due to the non projective structure of ECal. In azimuthal (φ) direction it is due to the rotation of charged particles trajectory in the magnetic field. The size of first type of elongation depends from the particle polar angle. The size of second type of elongation depends from the particle momentum. Second type of elongation is inherent only for the charged particles. In future these features of the cluster shape can be used for the improvement of the event reconstruction.

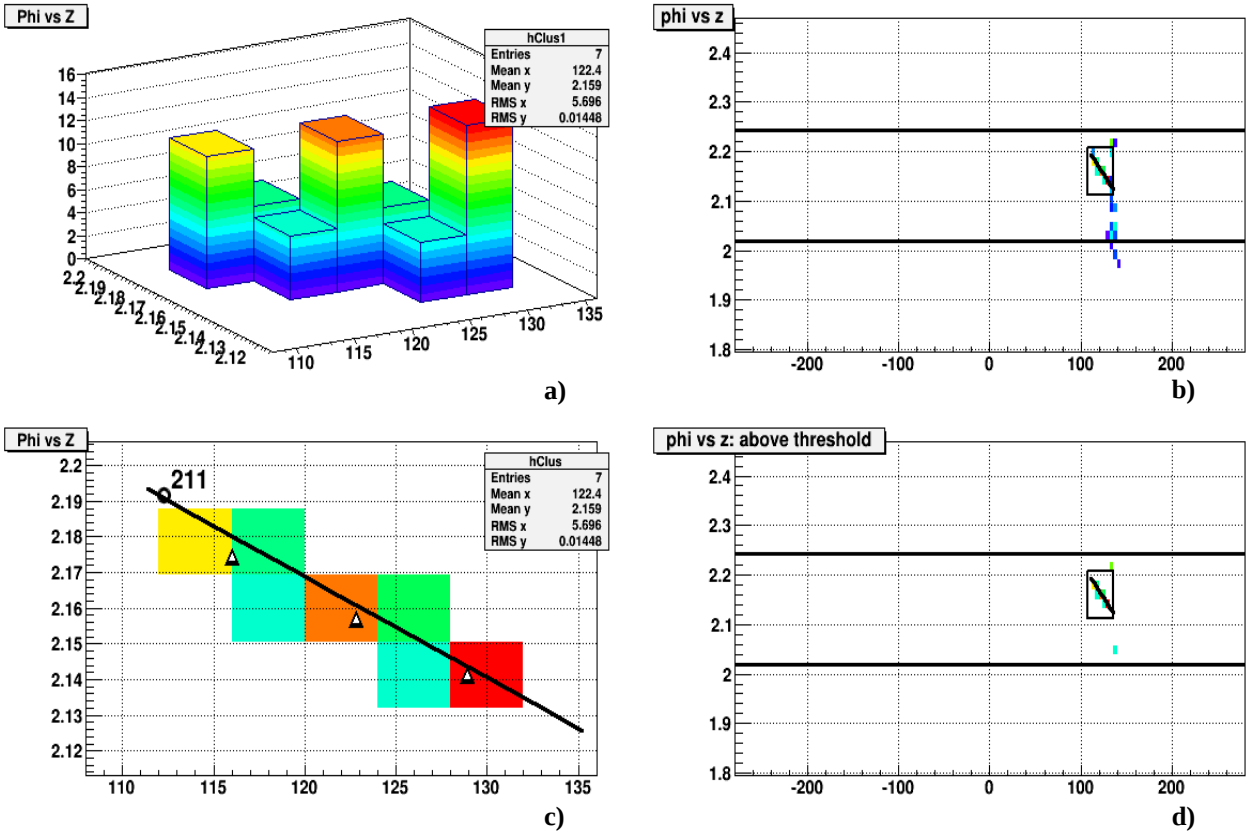

Figure 2.1.1: Cluster in ECal which formed by the charged pion with momentum of 0.5GeV/c. a,b,c) Z-φ plots without threshold; d)Plot Z-φ with threshold of 10MeV;

In some cases pions, crossing ECal, starts hadronic shower. In such case shape of cluster in the ECal becoming more complicated (Figure 2.1.2). This leads to the reduction of the accuracy of matching clusters to the tracks. As it is seen from the plot, some fraction of hits produced in such case do not matched to the pion track. For the electrons fraction of unmatched hits is close to zero.

Efficiency of hits matching to the charged pions tracks was calculated for the MC generated tracks created in the central AuAu interaction (7GeV). Dependencies of the efficiency of the clusters matching to the track versus the particles momentum and rapidity are shown on figures 2.1.3 and 2.1.4.

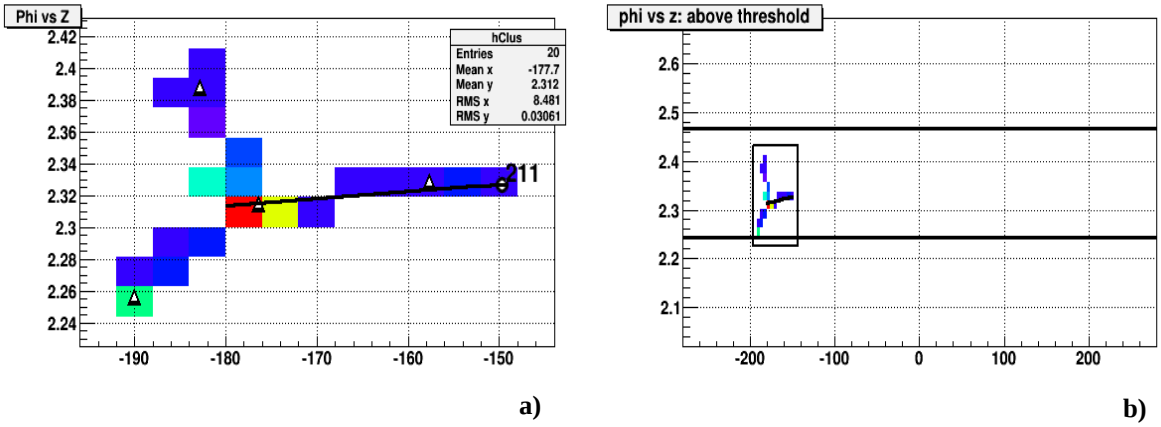

Figure 2.1.2: Clusters in ECal which are produced by charged pion, which is initiated hadronic shower. Both plots (**a,b**) with threshold of 10MeV.

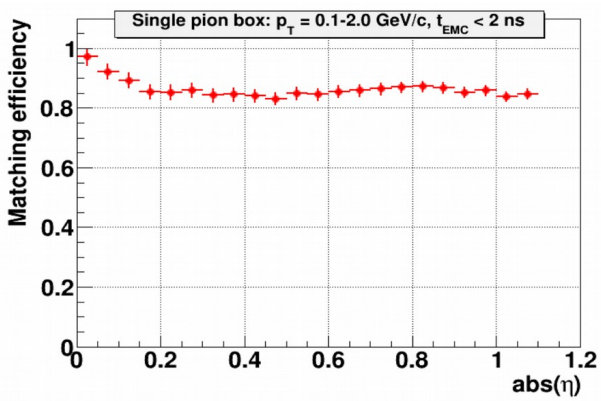

Figure 2.1.3: *Dependency of the efficiency of the clusters matching to the track from the particles momentum.*

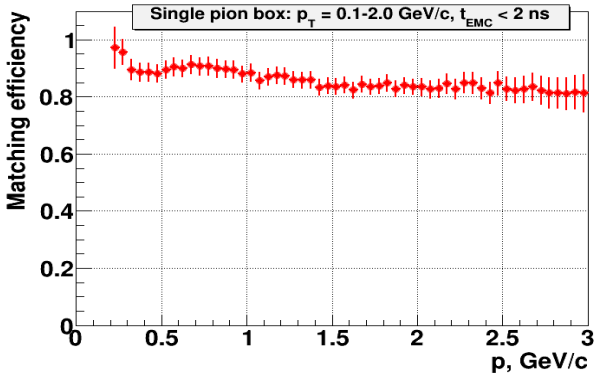

Figure 2.1.4: *Dependency of the efficiency of the clusters matching to the track from the particles rapidity.*

Unmatched hits will give fake contribution to the neutral particles multiplicity and energy. Fortunately this effect will concern only very low energy part of spectra.

2.2 Photons reconstruction

When some hits the in the ECal are associated with the trajectories of the charged particles then the rest of hits is the basis for the neutral particles reconstruction. Again, hits detected in the ECal, in the correct time interval and with energy deposition higher than certain threshold (10MeV) was joined into the clusters according simple rules -

1. Hits should have common border;
2. Hits should have energy deposition above threshold (10MeV);
3. Number of such hits should be higher than N_{tr} (3 hits) to form a cluster.

In case of neutral particles there is no elongation of the clusters in the φ direction (due to the rotation of particles trajectory in the magnetic field). Clear elongation in the *Z* direction should be presented and it should be *Z* dependent. First study of neutral particles reconstruction efficiency was done for the 250MeV photons and presented below on figures 2.2.1-2.2.4.

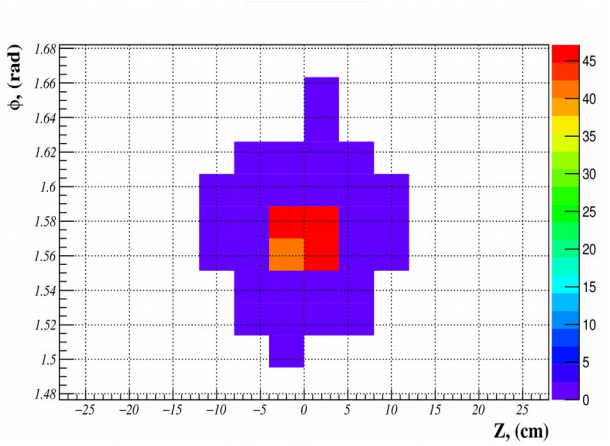

Figure 2.2.1: *Distribution (Z-φ) of clusters produced by the 250MeV photon hitting the 90 degree of polar angle (θ).*

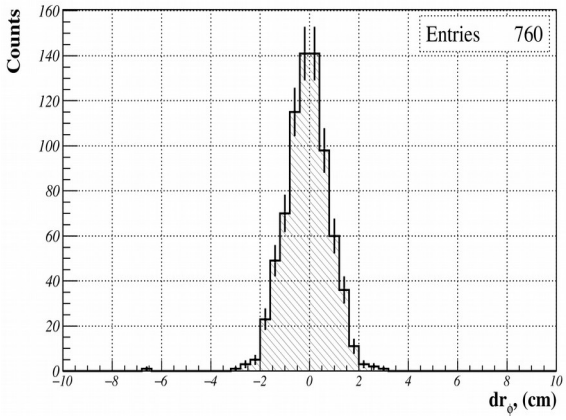

Figure 2.2.2: *Distribution of residuals between photon entry position (in the φ direction) and centre of gravity of the reconstructed cluster, when the particles hit in the 90 degree of θ (250MeV).*

In this case cluster size is the same in the *Z* and φ directions and no elongation in the *Z* direction can be seen (Figures 2.2.1-2.2.4). Residuals distribution between particles position in the φ direction (known from the MC) and centre of gravity of the reconstructed cluster is presented on figure 2.2.2. On the basis of this distribution the cut was chosen to be used in the procedure of neutral particle reconstruction. The cut $|dr\varphi|<4cm$ ($dr\varphi$ – distance in φ direction) is used on the next steps of procedure.

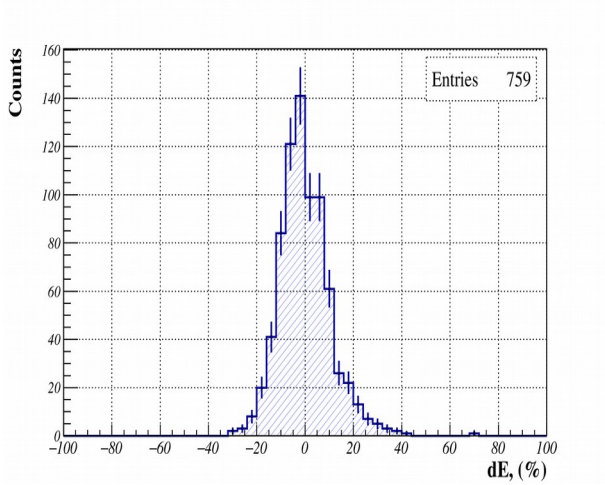

Figure 2.2.3: *Distribution of the difference between photon energy and the reconstructed cluster energy (250MeV, 90 degree of θ).*

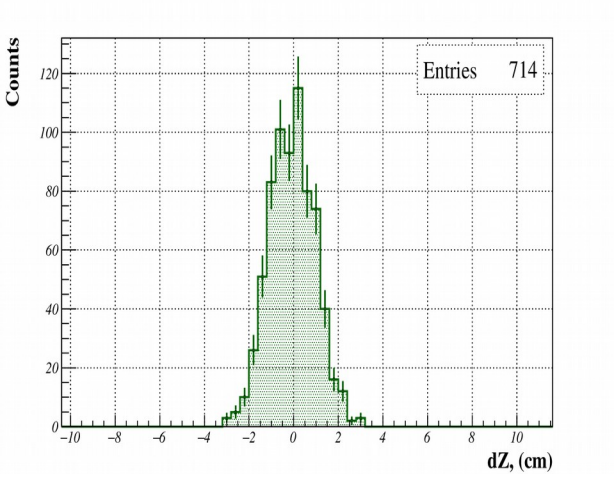

Figure 2.2.4: *Distribution of the difference between photon Z position and the reconstructed cluster Z position (250MeV, 90 degree of θ).*

Difference between photon energy and the reconstructed cluster energy (which satisfy $|dr\varphi|<4cm$ criteria) is plotted on the figure 2.2.3. For these low energy photons the cut of $|dE|<20\%$ can be used to calculate cluster reconstruction efficiency.

Last distribution is just an illustration, and will be not used in the selection procedure because of the elongation of the particle spot in the *Z* direction (Figure 2.2.4).

On the following pictures the same distributions are presented for the incidence polar angle (θ) of 70 degree are presented.

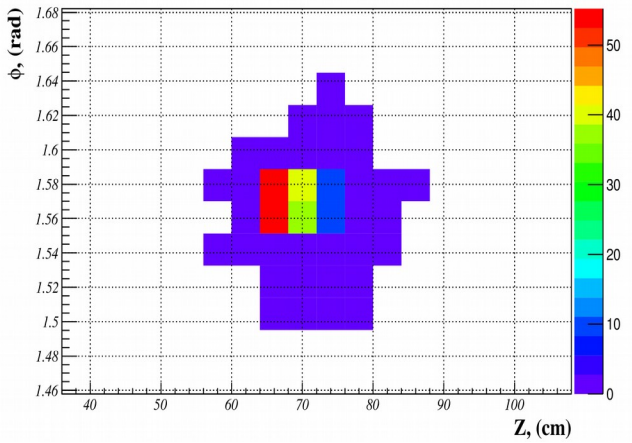

Figure 2.2.5: *Distribution (Z-φ) of clusters produced by the 250MeV photon hitting the 70 degree of θ.*

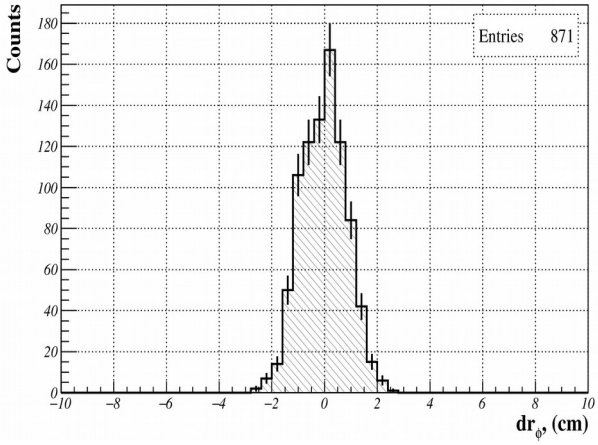

Figure 2.2.6: *Distribution of residuals between photon entry position (in the φ direction) and centre of gravity of the reconstructed cluster, when the particles hit in the 70 degree of θ (250MeV).*

All of them except the last one (Figure 2.2.8) are very similar to the previous figures. Shift from the zero in the figure 12 is reflects expected *Z* – elongation.

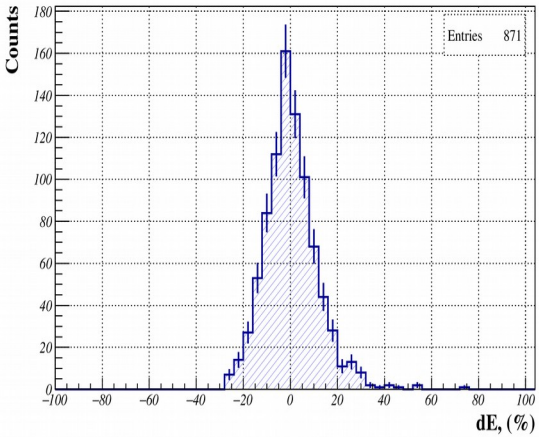

Figure 2.2.7: *Distribution of the difference between photon energy and the reconstructed cluster energy (250MeV, 70 degree of θ).*

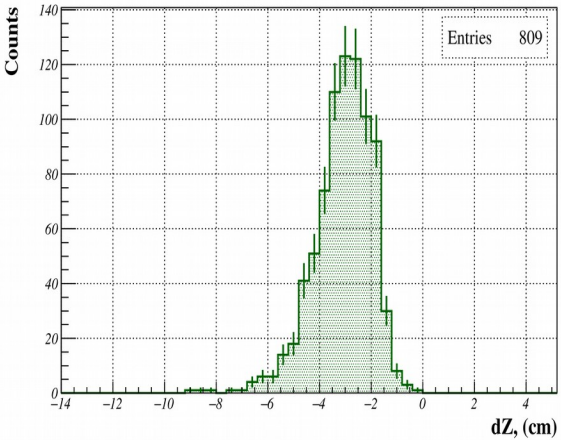

Figure 2.2.8: *Distribution of the difference between photon Z position and the reconstructed cluster Z position (250MeV, 70 degree of θ).*

On the next set of pictures the same distributions are presented for the incidence polar angle

of 50 degree are presented.

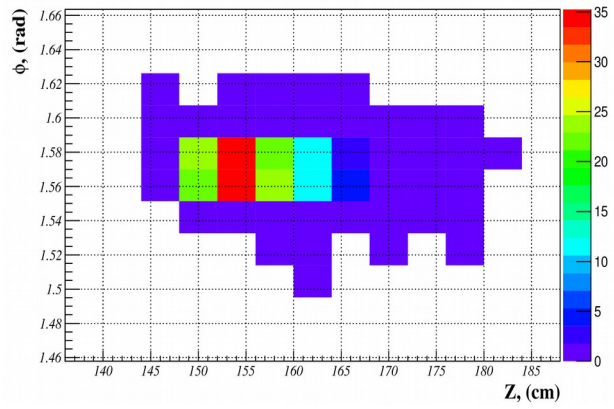

Figure 2.2.9: *Distribution (Z-φ) of clusters produced by the 250MeV photon hitting the 50 degree of θ.*

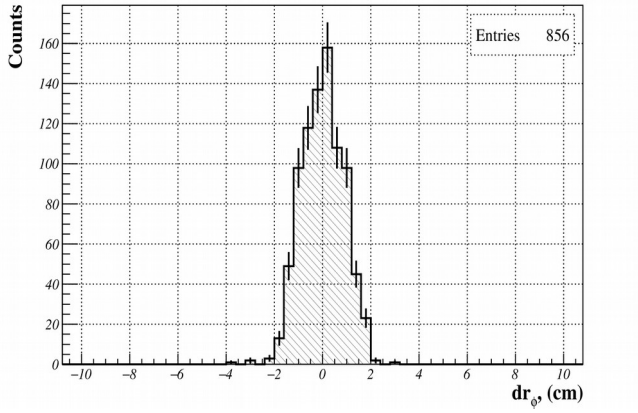

Figure 2.2.10: *Distribution of residuals between photon entry position (in the φ direction) and centre of gravity of the reconstructed cluster, when the particles hit in the 50 degree of θ (250MeV).*

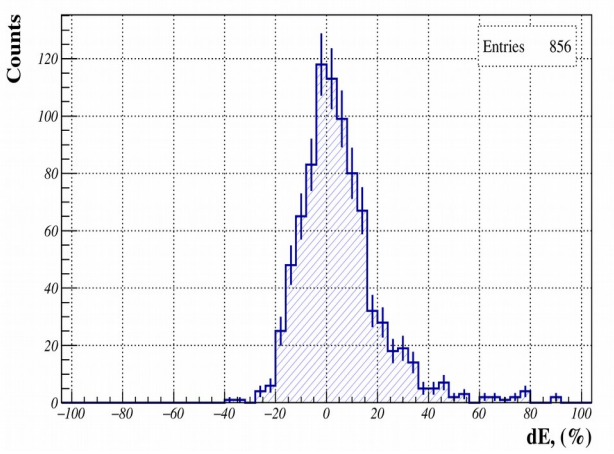

Figure 2.2.11: *Distribution of the difference between photon energy and the reconstructed cluster energy (250MeV, 50 degree of θ).*

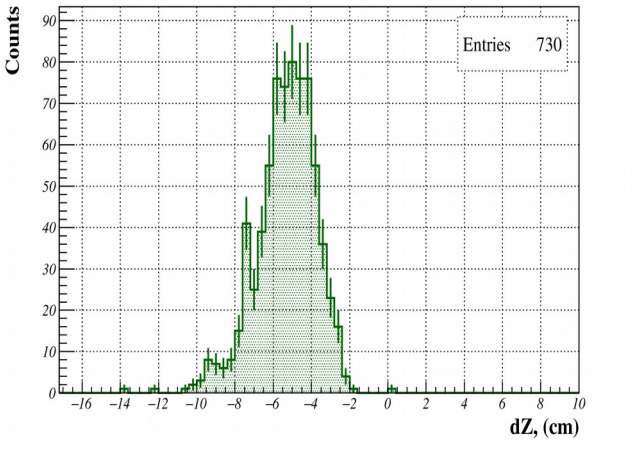

Figure 2.2.12: *Distribution of the difference between photon Z position and the reconstructed cluster Z position (250MeV, 50 degree of θ).*

Here elongation becoming more serious and even begins to impede for the effective detector hits association to the cluster (see figure 2.2.12). Efficiencies of the low energy photons reconstruction

in the ECal are summarized in the table 1.

Theta(deg)	90	70	50
|drφ| < 4cm	99.9	100	100
drφ| < 4cm && |dE| < 20%	99.3	92.9	85.3

Table 1: *Efficiencies of the low energy photons reconstruction.*

Next set of similar tests was done for the higher energy photons - 1 GeV.

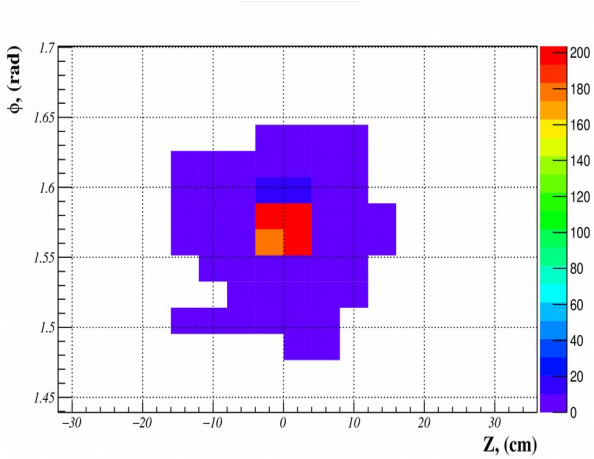

Figure 2.2.13: *Distribution (Z-φ) of clusters produced by the 1GeV photon hitting the 90 degree of θ.*

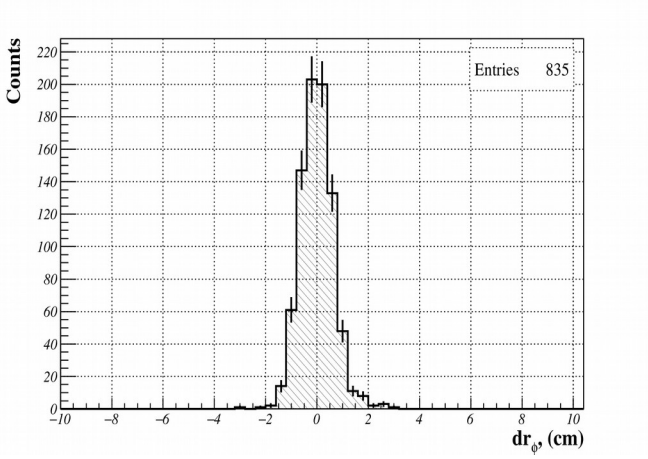

Figure 2.2.14: *Distribution of residuals between photon entry position (in the φ direction) and centre of gravity of the reconstructed cluster, when the particles hit in the 90 degree of θ (1GeV).*

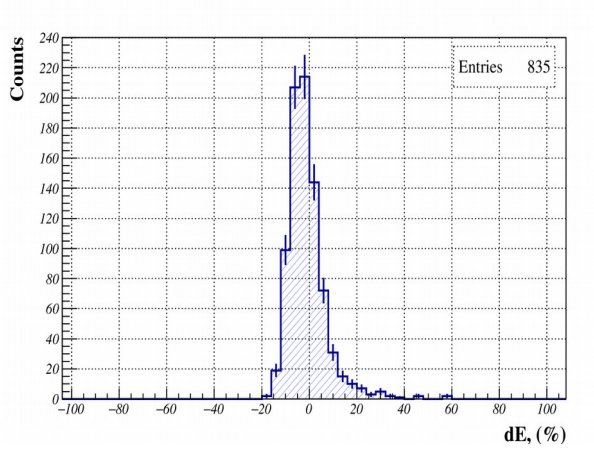

Figure 2.2.15: *The distribution of the difference between photon energy and the reconstructed cluster energy (1GeV, 90 degree of θ).*

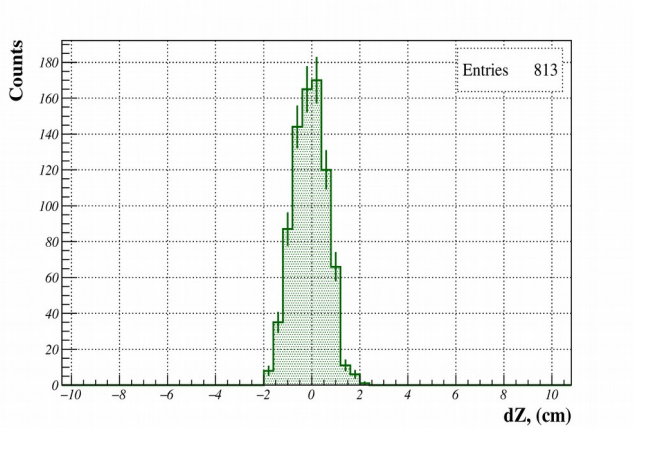

Figure 2.2.16: *The distribution of the difference between photon Z position and the reconstructed cluster Z position (1GeV, 90 degree of θ).*

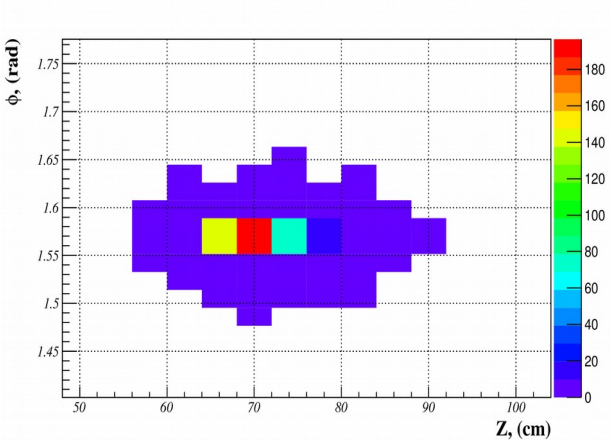

Figure 2.2.17: *Distribution (Z-φ) of clusters produced by the 1GeV photon hitting the 70 degree of θ.*

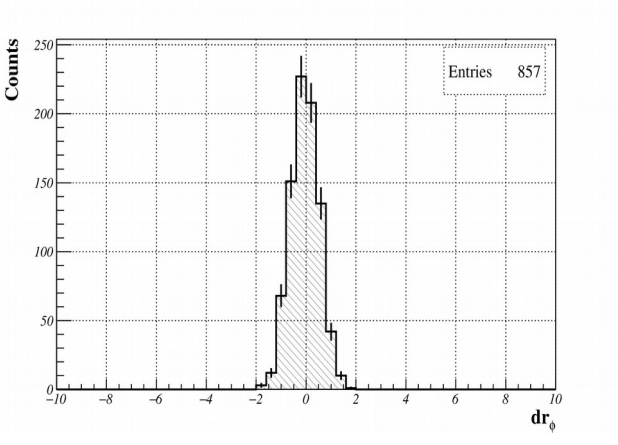

Figure 2.2.18: *Distribution of residuals between photon entry position (in the φ direction) and centre of gravity of the reconstructed cluster, when the particles hit in the 70 degree of θ (1GeV).*

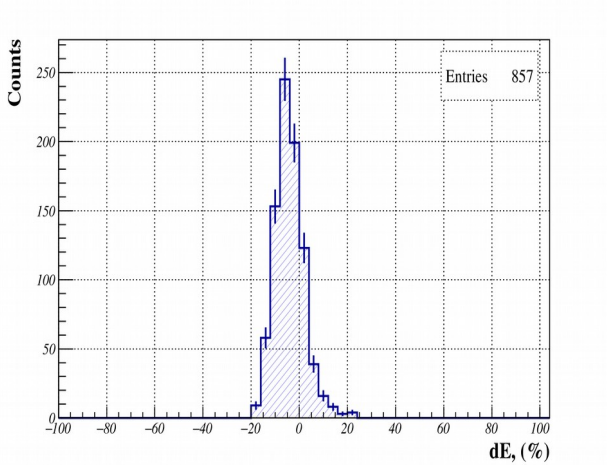

Figure 2.2.19: *Distribution of the difference between photon energy and the reconstructed cluster energy (1GeV, 70 degree of θ).*

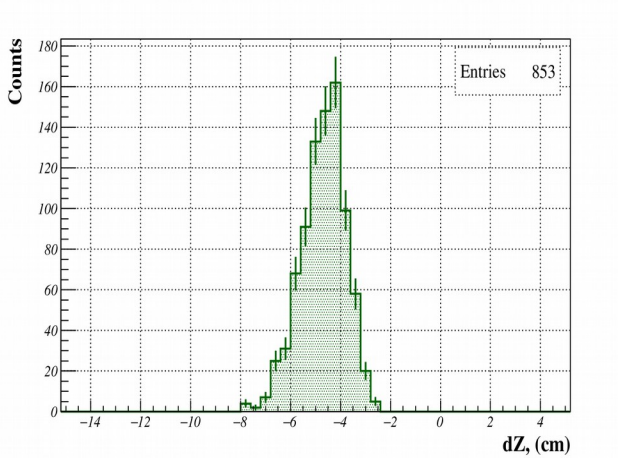

Figure 2.2.20: *Distribution of the difference between photon Z position and the reconstructed cluster Z position (1GeV, 70 degree of θ).*

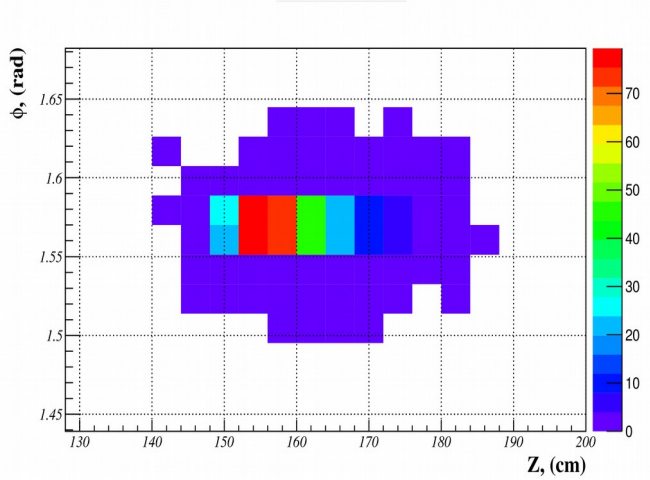

Figure 2.2.21: *Distribution (Z-φ) of clusters produced by the 1GeV photon hitting the 50 degree of θ.*

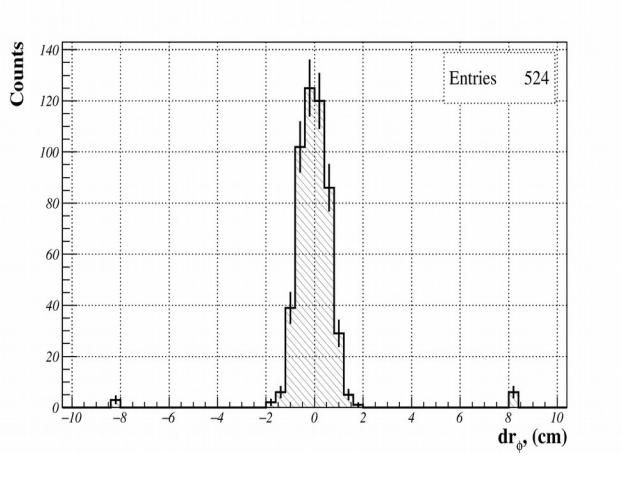

Figure 2.2.22: *Distribution of residuals between photon entry position (in the φ direction) and centre of gravity of the reconstructed cluster, when the particles hit in the 50 degree of θ (1GeV).*

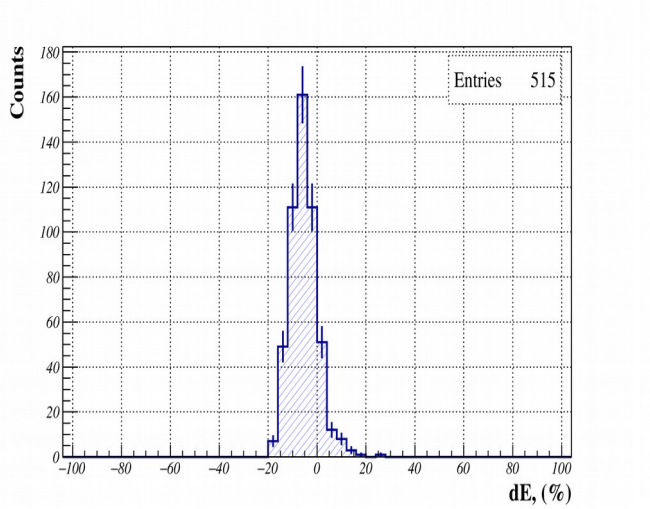

Figure 2.2.23: *Distribution of the difference between photon energy and the reconstructed cluster energy (1GeV, 50 degree of θ).*

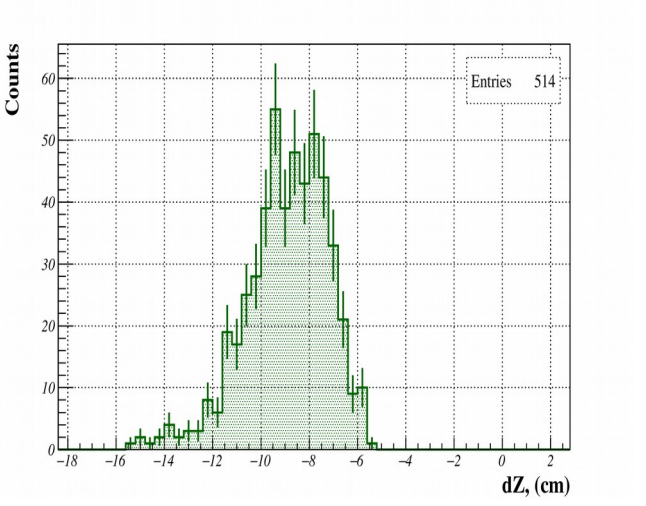

Figure 2.2.24: *Distribution of the difference between photon Z position and the reconstructed cluster Z position (1GeV, 50 degree of θ).*

Theta(deg)	90	70	50
|drφ| < 4cm	100	100	98.3
drφ| < 4cm && |dE| < 20%	97.4	99.5	98.1

Table 2: *Efficiencies of the 1GeV photons reconstruction.*

All previous results was obtained for the isolated photons. Events generated by the UrQMD generator for the 7GeV/c Au-Au minimal bias interactions has been used to estimate efficiency of the photons reconstruction in the events with different particles multiplicity. Search of clusters around each entry point of the photon to the ECal have been performed. Cluster has been considered as associated with photon if it distance from the generated track below 4cm in the φ direction and below 50cm in the *Z* direction.

Number of gammas					
Range of energy		$100<=E_\gamma<200$ (MeV)	$200<=E_\gamma<300$ (MeV)	$300<=E_\gamma<500$ (MeV)	$500<=E_\gamma$ (MeV)
I	**Wtihout Cut**	3781	2131	1936	1183
II	**Cut** $\lvert r_{MC} - r_{CL}\rvert$<4cm && $\lvert z_{MC} - z_{CL}\rvert$<50cm)	3093	1725	1557	904
II/I (%)		81.8	80.9	80.4	76.4

Table 3: *Efficiencies of the cluster matching to photons.*

Efficiencies of the clusters matching to the generated particles are presented in the table 3, for the different intervals of photon energy. Such studies has been performed for the events with the different impact parameters (different multiplicities of the photons) and no significant dependence of the photon reconstruction efficiency from the event multiplicity is observed.

Last test was done to study how the reconstructed neutral particles (multiplicity and total energy) correlated with the generated numbers of photons and were total energy. Results of these tests are presented on the figures 2.2.25 and 2.2.26. Strong correlation between reconstructed and generated variables clearly seen from the distributions. Unfortunately, correlations are not linear. In the high multiplicity region, it becomes weaker for both variables (N_γ and E_γ).

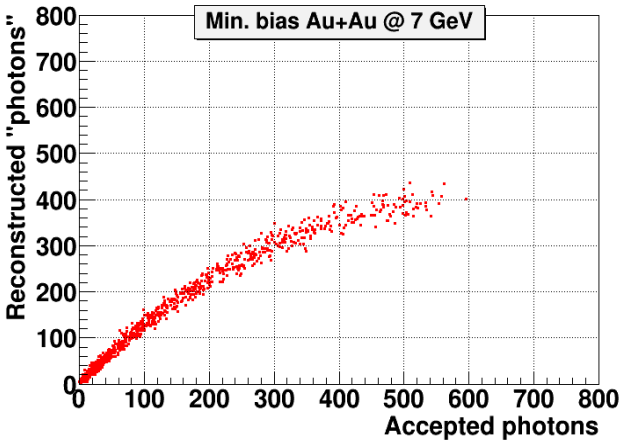

Figure 2.2.25: *Distribution of reconstructed numbers of neutral particles vs generated number of photons.*

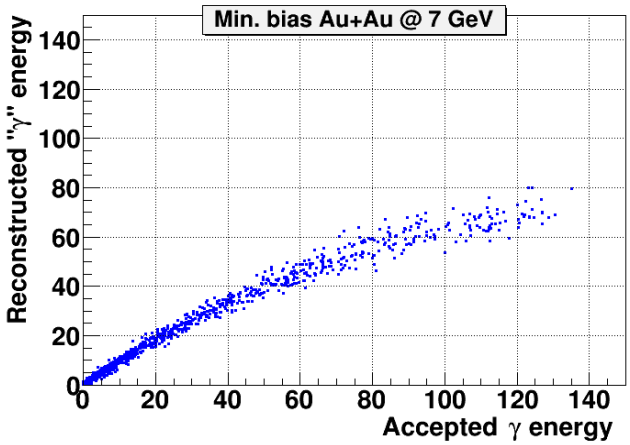

Figure 2.2.26: *Distribution of reconstructed neutral particles energy vs generated number of photons.*

Correction procedure which takes into account dependencies from the figures 2.2.25 and 2.2.26, including nonlinearities, has been developed. To estimate accuracy with which number of photons and their total energy can be reconstructed, events generated by the UrQMD generator for the 7GeV/c Au-Au minimal bias interactions have been used. Dependencies of the neutral particles flux reconstruction accuracy from the generated photon multiplicity is presented on figure 2.2.27. Similar dependence for the photon energy is presented on figure 2.2.27.

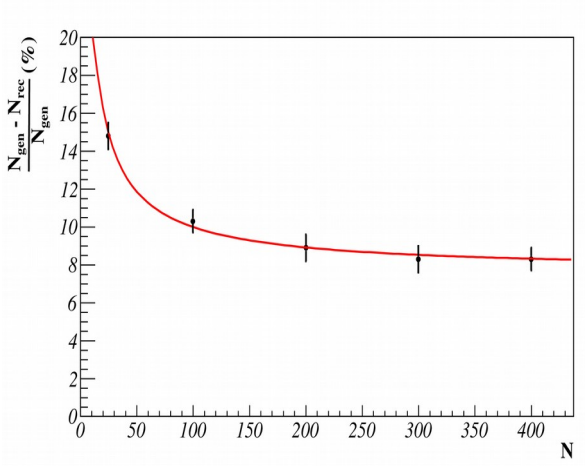

Figure 2.2.27: *Dependencies of the neutral particles flux reconstruc-tion accuracy from the generated photon multiplicity.*

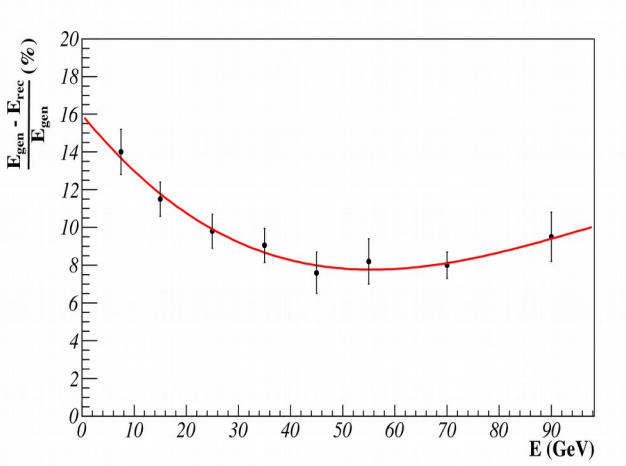

Figure 2.2.28: *Dependencies of the neutral particles flux reconstruction accuracy from the photon energy.*

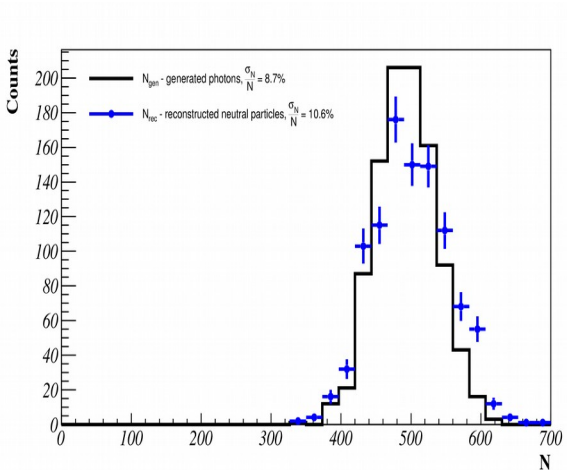

Figure 2.2.29: *Distribution of generated numbers of photons and the numbers of neutral particles after full reconstruction procedure.*

Events generated by the UrQMD generator for the 7GeV/c Au-Au central interactions have been used to illustrate effect of reconstruction on the measurements of the photon flux. On the figure 2.2.29 generated number of photons is shown as a solid line. Distribution with error bars is presenting the same events after full reconstruction procedure.

2.3 New geometry - projective

It was shown above that projective geometry in the polar angle direction is absolutely necessary to avoid died space and as a result drop of particle detection efficiency and degradation of calorimeter energy resolution. Situation in azimuthal direction is very different because there are no died space in this direction. Dependence of calorimeter energy resolution from the particle entrance angle to the detector was studied. It was shown that energy resolution is not degradation up to very high angles oh particle entry with respect to calorimeter axis. In those studies energy response of the calorimeter calculated by collecting of total response of the calorimeter But more recent studies, which was based on the new generation of the software developed for the MPD detector, demonstrated that involvement of the cluster finding algorithm (which is absolutely necessary in the conditions extremely high particle multiplicity- high occupancy of the detector) change the situation. Two different geometry – no projective to Z plane (Figure 2.3.1) and projective (Figure 2.3.2) have been used to simulate calorimeter response taking into account full event reconstruction procedure.

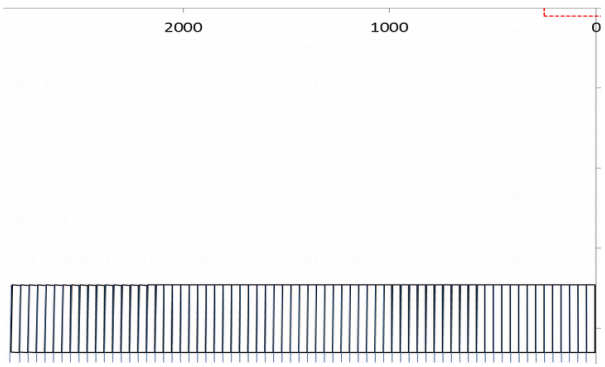

Figure 2.3.1: *View of the some modules of the no projective geometry in the Z plane.*

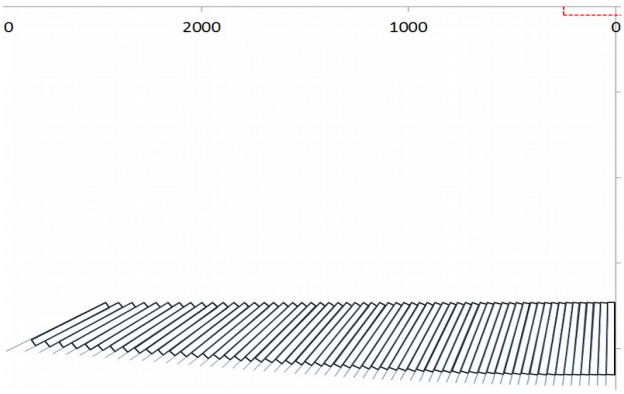

Figure 2.3.2: *View of the some modules of the projective geometry in the Z plane.*

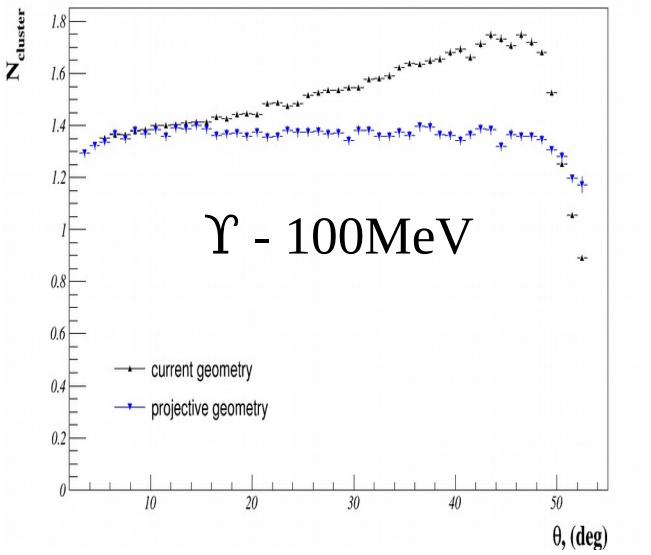

Figure 2.3.3: *Distribution of the number of clusters vs angle θ (Photons beam with energy 100MeV).*

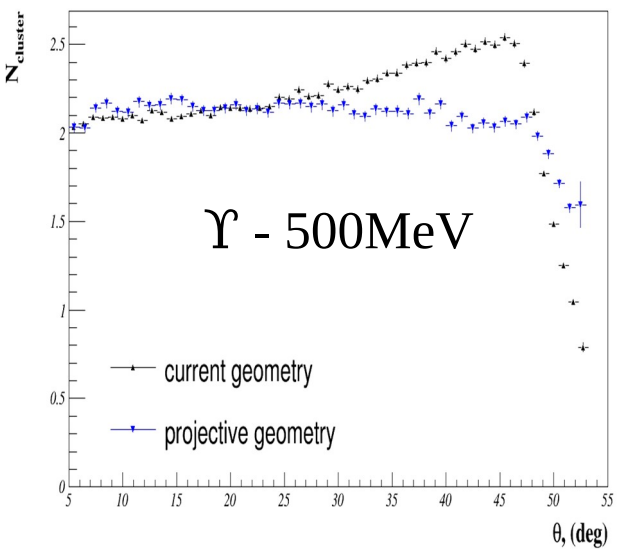

Figure 2.3.4: *Distribution of the number of clusters vs angle θ (Photons beam with energy 500MeV).*

It was discovered that number of clusters raising with the rise of particle incident angle (Figures 2.3.3 and 2.3.4). As a result, in spite of independence full energy deposition from the incident angle, the energy deposition per cluster is degrading with raise of incident angle (Figures 2.3.5 and 2.3.6). As a consequence, energy resolution and particle reconstruction efficiency becoming also dependent from the particle polar angle. In the same time it was demonstrated that making calorimeter projective in the polar angle direction, angular dependency can be completely suppressed (Figures 2.3.7 and 2.3.8).

Construction of the calorimeter which is projective in the polar direction becoming much more complicated. But the positive effect from such modification is very important for the quality of the MPD and decision was taken by the collaboration to change calorimeter design on the projective.

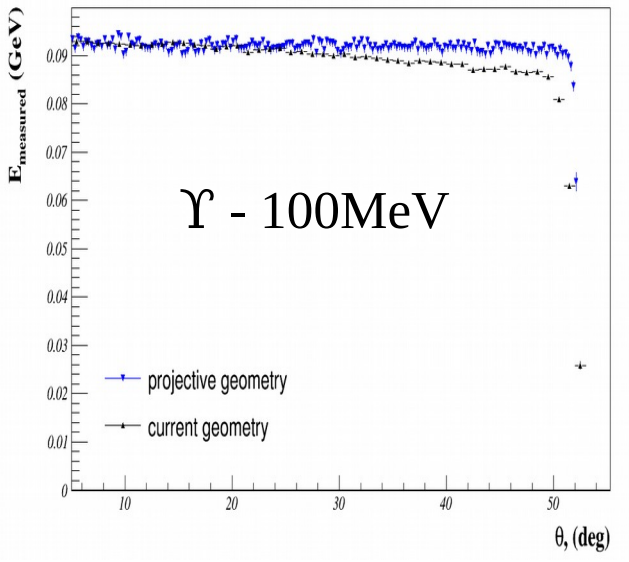

Figure 2.3.5: *Distribution of the energy measured of vs angle θ (Photons beam with energy 100MeV).*

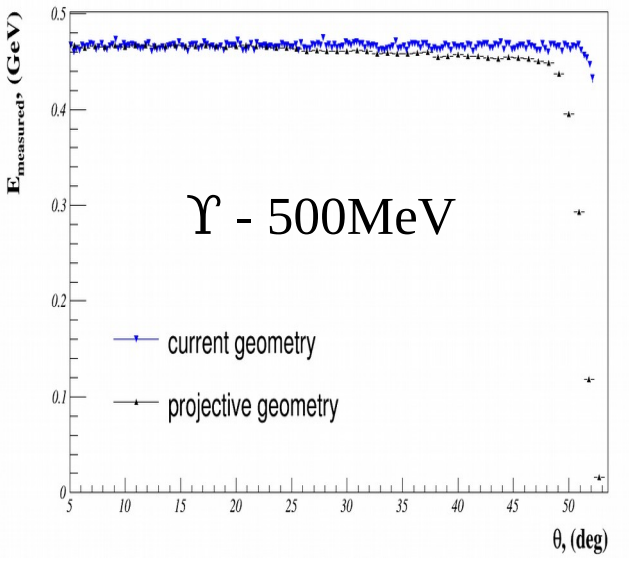

Figure 2.3.6: *Distribution of the energy measured of vs angle θ (Photons beam with energy 500MeV).*

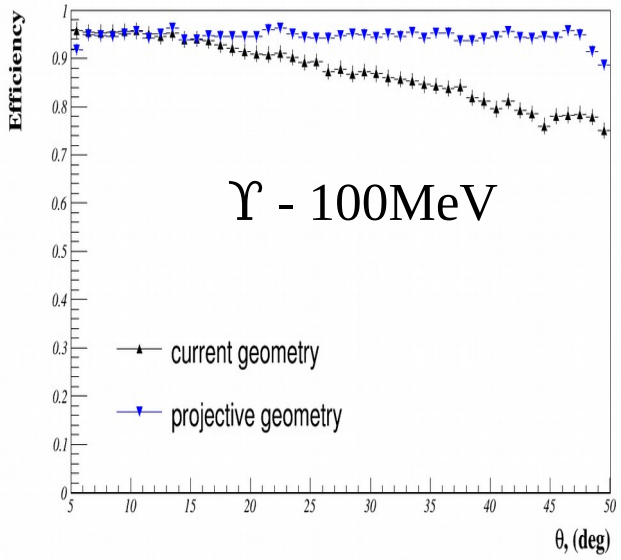

Figure 2.3.7: *Distribution of the efficiency of vs angle θ (Photons beam with energy 100MeV).*

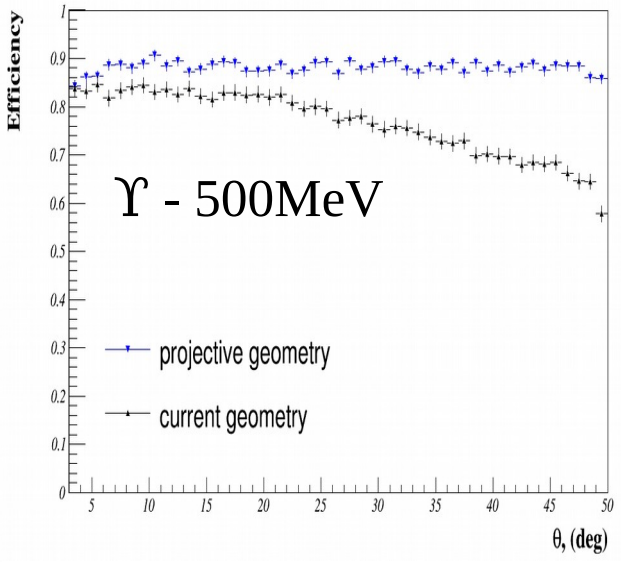

Figure 2.3.8: *Distribution of the efficiency of vs angle θ (Photons beam with energy 500MeV).*

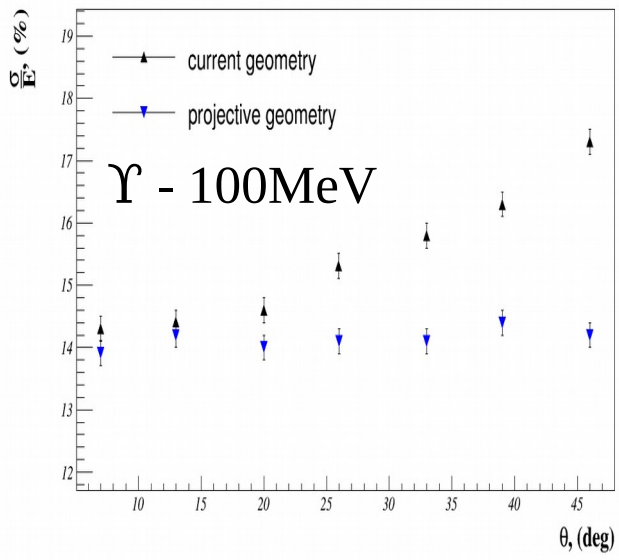

Figure 2.3.9: Distribution of the energy resolution of vs angle θ (Photons beam with energy 100MeV).

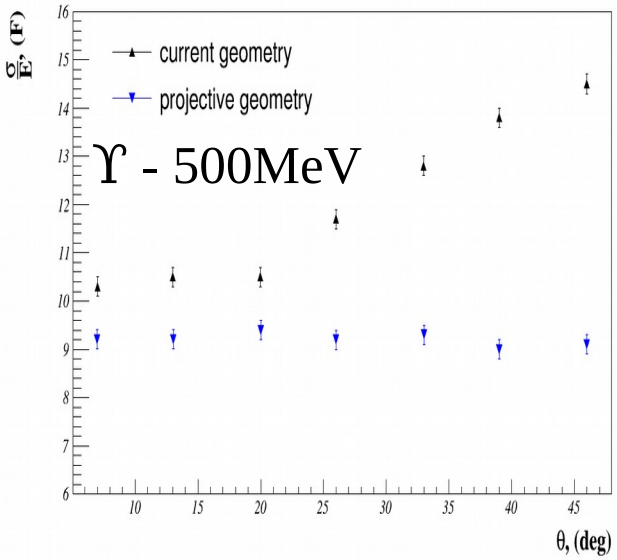

Figure 2.3.10: Distribution of the energy resolution of vs angle θ (Photons beam with energy 500MeV).

3 ECal design

As it is shown above, electromagnetic calorimeter is a essential component of the MPD detector which is making contributions in the different fields of physics. In making choice of the calorimeter type and its design, we take into account features of the experiment on the NICA collider, such as particles energy, particles flow, occupancy and some others. Technological aspects, possibility of integration to the whole MPD detector and a price of calorimeter are also taken into account in the choice of calorimeter design. Only the crystal calorimeter can make the real competition to the "shashlyk" one. But much higher price and usually much worse time resolution of crystal calorimeter forced us to make a choose in favor of "shashlyk" type calorimeter.

The first Shashlyk calorimeter was designed and manufactured at Institute for Nuclear Research (Moscow) in 1991 for the experiment 865 [31] (Search for the Lepton Number Violating Decay K+ → _+μ+e−) at the BNL AGS. During the five-year high intensity run of the experiment, the Shashlyk calorimeter was a very stable and reliable detector. Later Pb-scintillator electromagnetic calorimeter of the “shashlyk”-type were used in the PHENIX [32], KOPIO [30], LHCB [33], T2K [34], and some other detectors. The best resolution for the "shashlyk" type calorimeter has been achieved by the KOPIO collaboration. As an example, the energy-resolution measured in the KOPIO experiment for various readouts is shown in figure 3.0.1. A quadratic fit to these experimental data gives $\sigma(E)/E = (1.96 \pm 0.1)\% \otimes (2.74 \pm 0.05)\%/p(E)(GeV)$, where ⊗ means quadratic summation.

Time resolution for the "shashlyk" calorimeter has been measured and estimated first by the KOPIO collaboration (Figure 3.0.2). Our design is based on the experience of existing detectors and is oriented on the industrial possibilities of JINR member states.

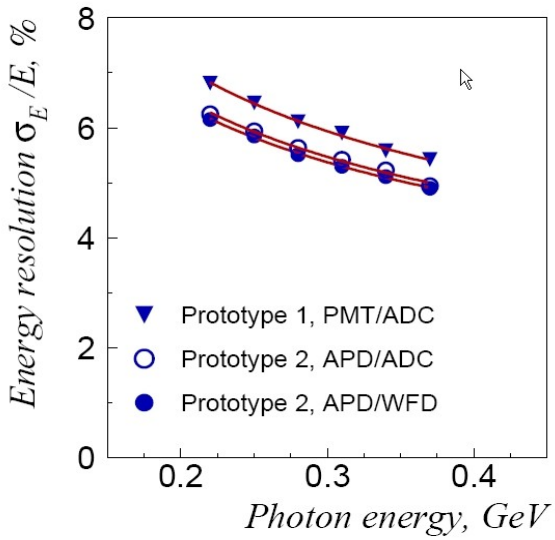

Figure 3.0.1: *Energy resolution of the "Shashlyk" type calorimeter measured in the beam test.*

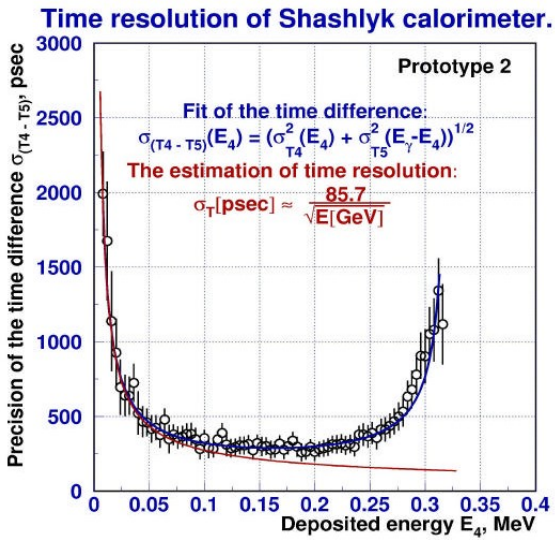

Figure 3.0.2: *Time resolution of the Shashlyk type calorimeter.*

Space allocated for the barrel part of ECal is shown on the figure 3.0.3 as a magenta area. More details concerning ECal place in the MPD detector can be seen on the figure 3.0.4.

The MPD electromagnetic calorimeter is proposed to be built of modules as basic building elements. Later, modules will be assembled to the sectors which will be a basic element for the ECal integration into MPD setup.

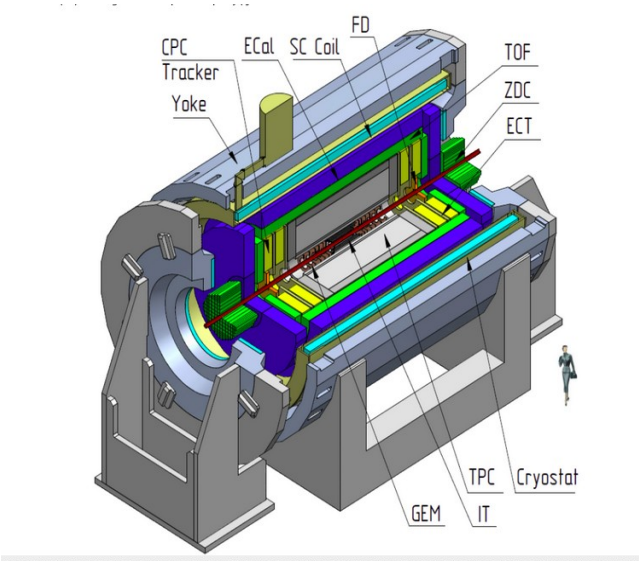

Figure 3.0.3: *General view of the MPD detector.*

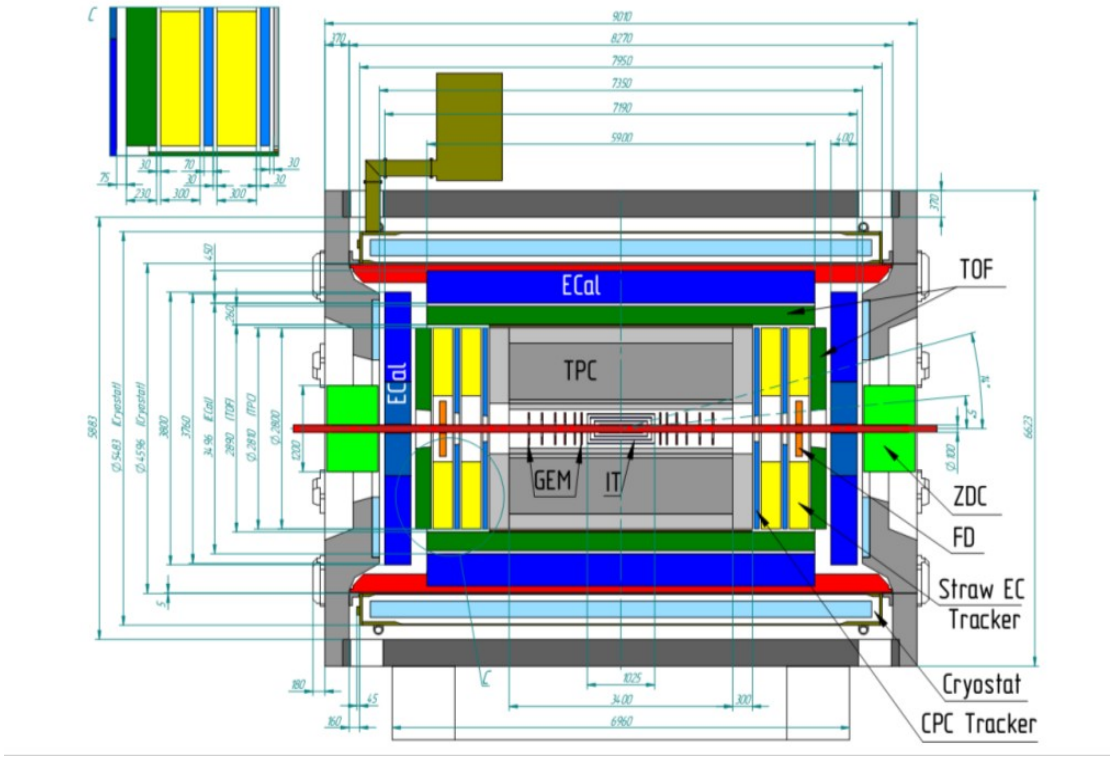

Figure 3.0.4: *Cutaway side view of the Central Detector of MPD with based dimensions.*

3.1 ECal module

The "shashlyk" module is a lead-scintillator sandwich which read out by means of Wave Length Shifting (WLS) fibers passing through the holes in scintillator and lead. An examples of the “shashlyk” calorimeter module is shown in figure 3.1.1.

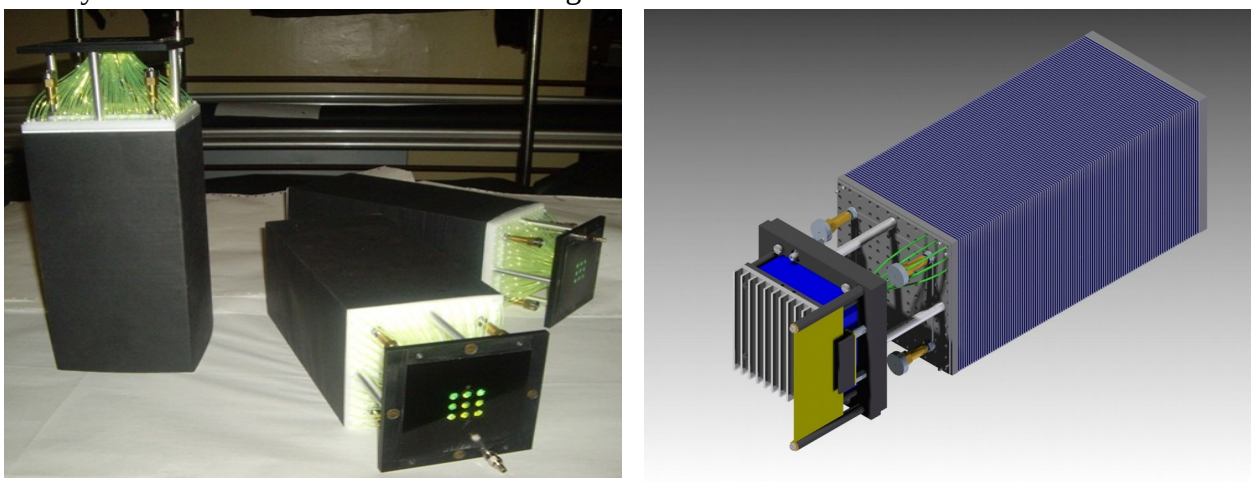

Figure 3.1.1: *Shashlyk calorimeter module (left) and schema of the ECal module (right).*

In contrast with shown examples the MPD electromagnetic calorimeter module is proposed to be built from one tower as basic building elements ($4cm^2$). Tower consist of 220 alternating tiles of Pb (0.3mm) and plastic scintillator (1.5mm). Each scintillator tile is optically isolated from the neighbor tiles. Lead layer is common for all nine tiles of one layer.

The module with a 12 radiation length thickness will be approximately 40cm long. The light collected with 16 fibers is read out by MAPD units with $3\times3mm^2$ sensitive areas. Assembling procedure in brief can be described as a following (In the description we used existing documentation for the nine towers module, Figure 3.1.2):

1. Assembly begins from the front supporting plane.
2. The first lead plate is set on the support plate. Correct positioning of all lead plates and all scintillating plates are assured by the pins and corresponding holes (lego like) on the surface of all plates of the sandwich.
3. The first scintillating tile is set on the position.
4. Following scintillating tiles, of the same plane (up to nine), are set on their positions.
5. Completing of the first scintillating tiles plane.
6. Second lead plate is set on place.
7. The first scintillating tile of the second scintillating plane is set on the position.
8. Completing of the second scintillating tiles plane.
9. Consecutive repetition of the above procedure up to 220 pairs of planes.
10. Completion of the construction of the calorimeter active part.
11. End plate is set on place to cover assembled sandwich.
12. Next two pictures are illustrating a coupling procedure of a calorimeter sandwich by means of the two steel strings which passed through openings in the calorimeter planes. First parts of the tension tools is set on the position on the end plate.
13. The planes of the module are pulled together with two loops of a steel string. Strings are are fixed by the four tension screws.
14. Sixteen WLS of first tower are inserted and connected in the dense sheaf on the read-out site.

15. Nine towers are equipped by the WLS, each of groups are connected in the dense sheaf and the these groups are fixed on the end plate of the module.
16. Light protecting cover is installed - module is assembled.

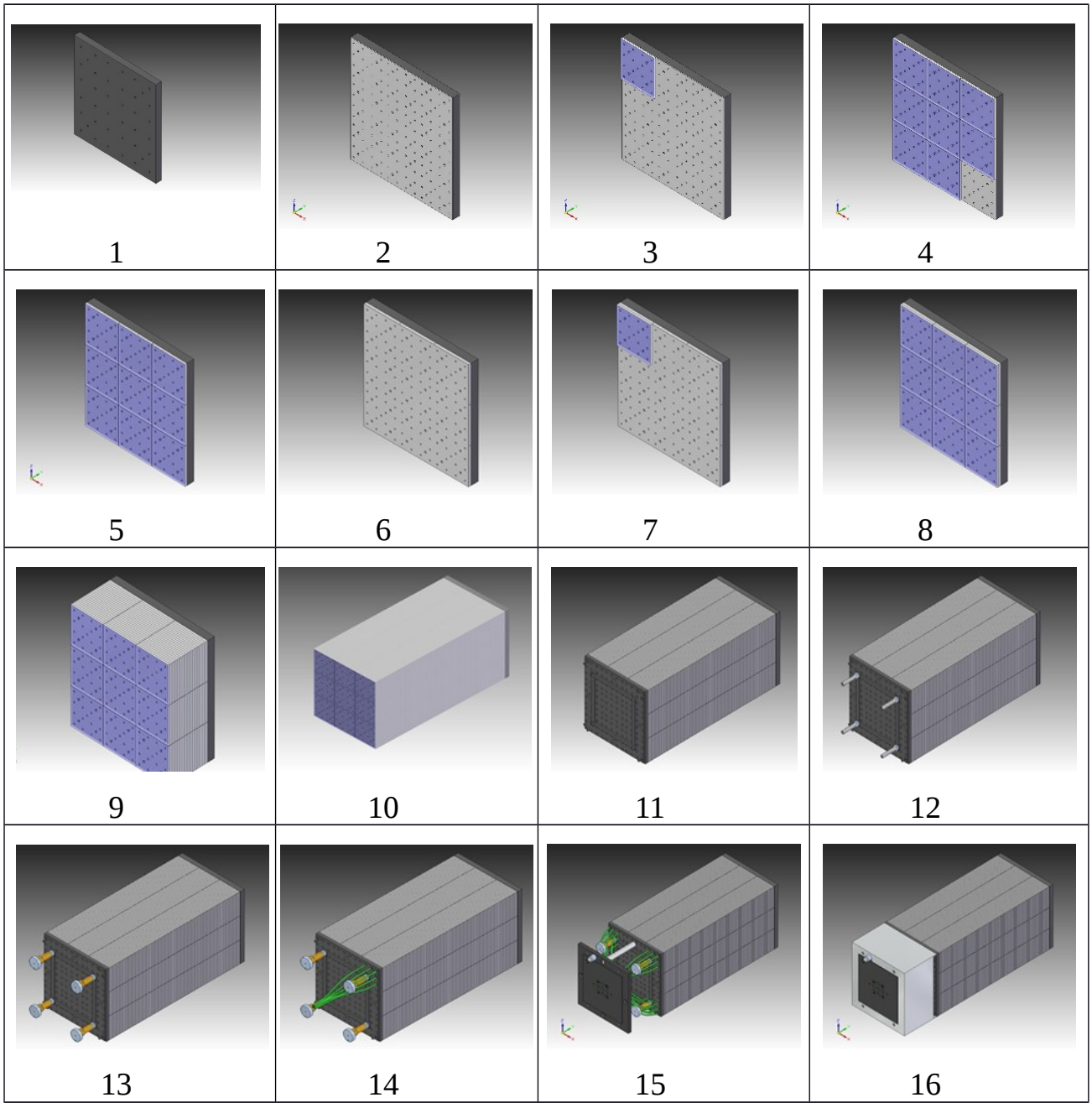

Figure 3.1.2: *Procedure of module assembling.*

The main parameters of ECal are listed below in the table 4.

Parameters	
Transverse size, mm^2	40x40
Module size, mm^2	120x120
Number of layers	220
Lead absorber thickness, mm	0.3
Thickness of Scintillator, mm	1.5
Effective radiation length, mm	32.4
Moliere radius, mm	62
Radiation length, X_0	11.8

Table 4: *Main parameters of ECal.*

To detect scintillating light, which is collected and transported by the WLS to the end plate of the module, special detecting head has been designed and produced.

The diameter of the bundle of 16 WLS fibers is about 8 mm but the size of the MAPD photon counter 3x3 mm^2. To collect all light coming from the bundle on the MAPD counter light concentrator (Winston-cone) is used. Due to full internal reflection on the surface of the cone, which is produced with a special shape, concentration of light at the exit from a cone is provided. Winston cone is concentrating light on the 3 mm^2 HAMAMATSU S13360-6025PE MAPD counter (Figure 3.1.3) [35].

The following characteristics were measured at the operation voltage that yields the listed gain (Table 5).

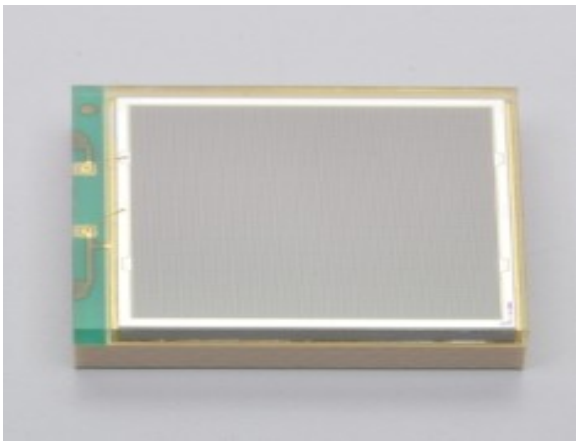

Figure 3.1.3: HAMAMATSU S13360-6025PE MAPD.

This MAPD device has been chosen due to many advantages with respect to the others MAPDs which we ever tried to use. Some of those advantages are:

- smd devices – compactness;
- higher photon detection efficiency;
- very low dead time;
- availability;
- identity of detectors of one type;

Type no.	Measure-ment conditions	Spectral response range λ (nm)	Peak sensitivity wavelength λp (nm)	Photon detection efficiency PDE*4 λ=λp (%)	Dark count*5 Typ. (kcps)	Dark count*5 Max. (kcps)	Terminal capaci-tance Ct (pF)	Gain M	Break-down voltage VBR (V)	Crosstalk probability (%)	Recom-mended operating voltage Vop (V)	Tem-perature coefficient at recom-mended operating voltage ΔTVop (mV/°C)
S13360-1325CS	Vover =5 V	270 to 900		25	70	210	60	7.0×10^5		1	VBR + 5	
S13360-1325PE		320 to 900										
S13360-3025CS		270 to 900			400	1200	320					
S13360-3025PE		320 to 900										
S13360-6025CS		270 to 900			1600	5000	1280					
S13360-6025PE		320 to 900										

Table 5: *Parameters HAMAMATSU MAPD s13360-6025.*

Each detector head after production will be tested and all MAPDs calibrated.

Then, calibrated heads will be assembled with module and on this stage module is ready for the tests. Each module should be calibrated on the cosmic muons. After calibration modules are ready for the assembling to the sectors.

3.2 FE electronics

Front-End (FE) electronics will be located directly on the calorimeter. This solution is chosen due to the evident advantages:

- Small path of analog signal to FE means less signal distortion and pickup noises.
- Much simpler transport of digital signal from the calorimeter to the event building electronics. Number of connectors between FE boards and electronics outside detector falls from 1536 (number of channels per sectors) in case of analog signal transport falls to 24 (number of channels per sector / number of channels in ADC board (64)) in case of digital signal transport. In the later case we use very thin optical cable.
- Very high event read out rate can be reached by using zero suppression and even signal processing directly on the FE board.
- One disadvantage of this solution is the need to extract the heat from the FE electronics out of MPD detector.

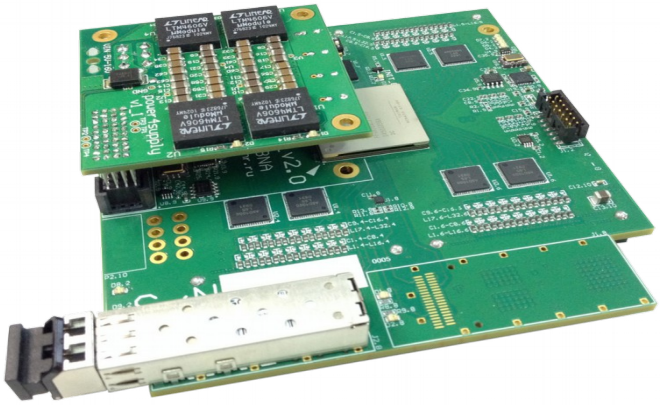

Figure 3.2.1: *ADC64s2 – Front-End board with ADCs amplifiers Ethernet communicator 2411 [37].*

As a FE electronics unit we have designed and constructed ADC 64 channel board (Figure 3.2.1). ADC board is a waveform digitizer. It quantize analogue input signal and samples it at fixed time intervals. Zero suppression logic is based on baseline estimation and threshold value. Signal shaping is performed in digital form with FIR filters. It allows to reduce the number of waveform points required for digital signal representation with minimum loss of accuracy. The ring type memory allows the read back of last 30 μs of waveforms. It sets the limit on trigger latency to

this value.

ADC board allows to be integrated to the White Rabbit system. White Rabbit provides sub-nanosecond accuracy and picoseconds precision of synchronization for large distributed systems. It also allows for deterministic and reliable data delivery.

3.3 Slow Control

The main objectives of system for monitoring of slowly changing parameters and management of auxiliary electronic systems in physical experiment (slow-control system) are:

- Monitoring of parameters of work of the equipment.
- Management of work of slow-control equipment. In our case - low-voltage and high-voltage power supplies, calibration system.
- Record of slow-control commands commands and data.
- The notification about problems (Alarms).

The aspects concerning SC system general logic, software and platform will be discussed in the special section. Here we give short description of hardware designed for the ECal SC system.

High voltage system has been designed especially for the MAPD based devices. Specific points of this system are:

- Multichannel (60 000 channels);
- Very precise voltage setting for each channel;
- Need of voltage correction depending of temperature of MAPD;

3.3.1 High Voltage

All this requirements have been realised by "HVSys” company in the HCal HV system including following components:

- 9 channel board;
- system unit;
- system bus;

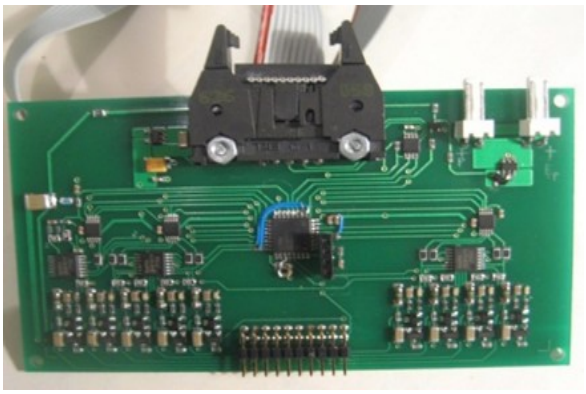

Figure 3.3.1.1: *HV module.*

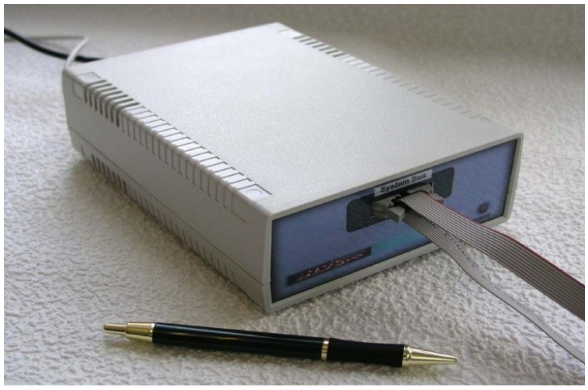

Figure 3.3.1.2: *Control Units (Communication base voltage generation).*

Each ECal module will be connected with one 9-channel HV board, which will be located in the ventilated box close to the module detection part. Via system bus each HV board receive base voltage 90 V and driving commands from the system unit.

Through the short (not more than 15cm) flat cable each HV board will deliver individually tuned voltage on nine sectors of the calorimeter module. One line of this flat cable dedicated to the temperature measurements on the detection head of the ECal module. On the basis of these

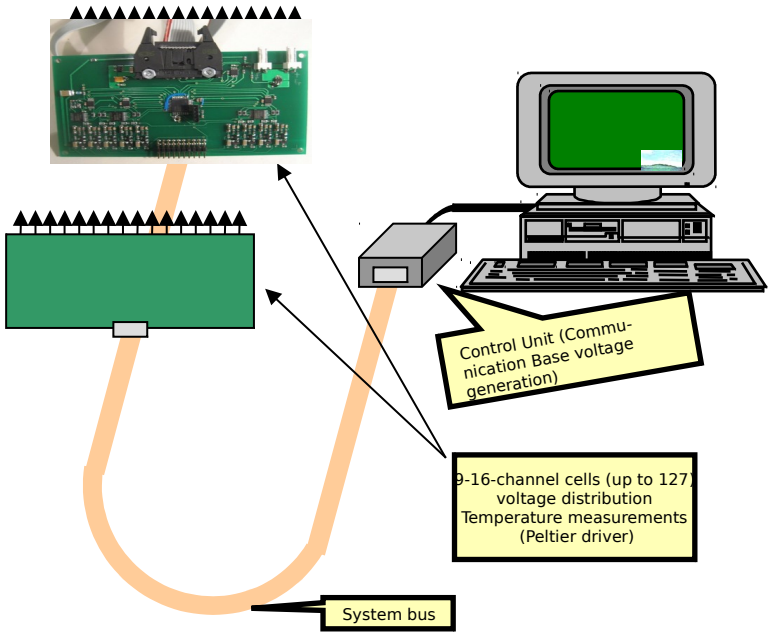

Figure 3.3.1.3: *HV system block diagram.*

1	Range of max output voltage	Up to 250V
2	Range of output voltage regulation	Umin - Umax
3	Precision of output voltage regulation	20v/10 bit
4	Output voltages spread (channel from channel)	1%
5	Stability of an output voltages	0,005 %
6	Temperature coefficient of an output voltage	200 ppm/K
7	Maximal average output current	10 mkA
8	Self-diagnosis of the BV channel	Yes
9	Current measurements	Possible
10	System bus	6 line flat cable
11	Max length of system bus	Up to 100 m
12	Number of cells per system bus	Up to 127

Table 6: *HV system parameters.*

measurements of temperature HV system will make voltage correction, to compensate temperature dependency of the MAPD amplification.

Most important HV system parameters are listed in the table 6.

2.3.2 LED Generator

To make a precise calibration of each ECal registration channel and also for the continuous

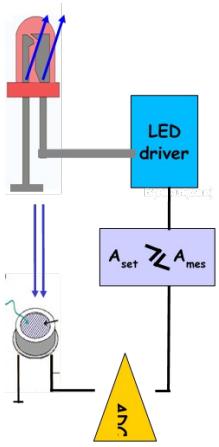

Figure 3.3.2.1: *Block diagram of the calibrator.*

monitoring of channel amplification LED generator of short bright blue light signals has been designed and built. Main requirement to this device is its stability. Light intensity variation should be below 1%. Block diagram of calibrator is shown on figure 3.3.2.1. To reach such stability two solutions have been realized in this device. First, special mode of operation for the LED driver was been found. In this high-charge mode LED operation becoming much more stable comparing with usual one. Second, to reduce residual variations of LED light intensity the feedback loop has been implemented to the device. The pin diode has been located on the LED back side. Light from the LED back side detected by this pin diode digitized by the ADC and analyzed by the comparator. Result of this analysis is used to correct the LED light intensity by changing the current in the driving signal. This correction allows to keep LED light constant and equal to the set value.

3.3.3 Temperature and pressure

Due to the sensitivity of MAPD detectors to the temperature it stability is the subject of our constant attention. Temperature sensors will be located along the ECal sectors. Through these sensors Slow Control system will take temperature conditions around ECal under constant attention. Pressure and temperature inside the ventilated duct with electronics is the subject not only registration but also control of these correlated parameters via the operated input/output valves .

3.4 Power consumption and cooling

The power consumption is estimated for the ECal subsystems as about 11.6 KW in total. This does not include DAQ systems outside the MPD barrel. All FE and Slow Control electronics located directly on the ECal module inside the MPD barrel. The heat from these electronics devices should be evacuated from the MPD barrel. Total power estimated as a 250mW/ch, that brings to about 207W per ECal sector. Even this small amount of heat cannot be left inside closed volume of the barrel. According our estimation (experimentally tested, see below) this amount of heat can be extracted by the air ventilation inside the closed duct with all electronic devices inside. It is duct 3 meters long with cross-section of 100x50 mm. To minimize cross-section of inlet and outlet pipes

connecting duct with the outside barrel equipment the air pumped inside with some overpressure and evacuated by the intensive pumping out. To avoid over/under pressure inside duct pressure inside duct measured by the Slow Control system and controlled by this system via input/output valves.

According our calculations, to have a guaranteed cooling and even some spare power in the cooling system size of inlet-outlet pipes should be about 10 cm^2. This size easily fit dedicated to ECal space in the cable holes in the detector body.

4 Test results

All parts of ECal detector have been produced some of them in few iterations. ECal "Shashlyk" modules have been produced in Kharkov (Ukraine). The FE and Slow Control electronics was designed at JINR. Many tests with all elements of ECal detector was performed during last three years.

4.1 Calibration

Despite that all MAPD detectors are calibrated and certified by the producer, the verification procedure should be developed. This procedure should be almost automatic, taking into account huge number of channels in the MPD ECal detector. The MAPD detectors was lit by the short light

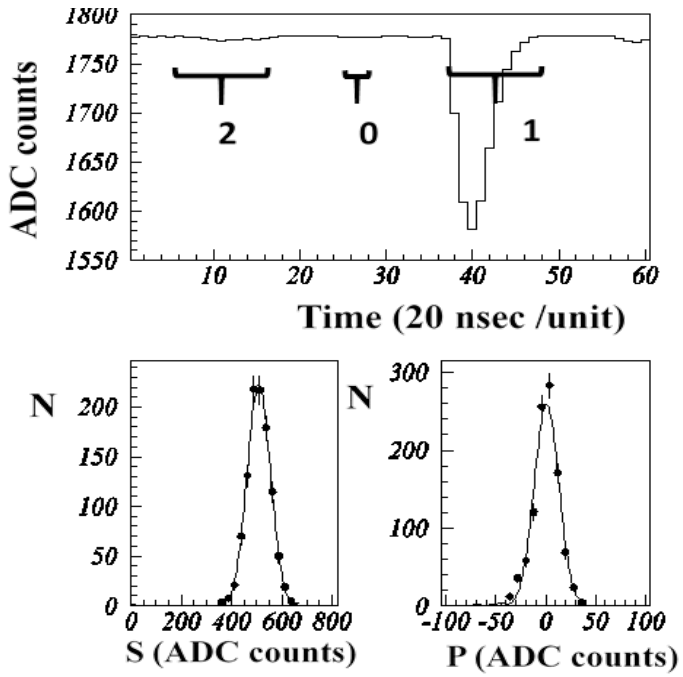

Figure 4.1.1: *Up – measured signal from LED pulse light. Region "0" - measurements of the pedestal, "1" - measurements o the signal, "2" - background. Bottom left – signal amplitude distribution. Bottom right – pedestal distribution.*

impulses generated by the LED generator. Such impulse is registered by the FE electronics –

figure 4.1.1.

Amplitude of the LED pulse was chosen to have number of fired MAPD pixels big enough to be well detected above noise, but not too big in order to be sensitive to the statistical fluctuations of this number. Measurements of these statistical fluctuations is the basis to calculate MAPD characteristics. In each event, we are calculating first the pedestal, as an average of the measurements in the region "0" before the signal (Figure 4.1.1). This pedestal is used then as a zero level in calculation of the signal integral (region "1" Figure 4.1.1) and the pedestal integral (region "2" Figure 4.1.1). As a result of many such measurements under the same conditions (HV and temperature) we are getting two distributions - signal and pedestal (Figure 4.1.1). Fit of this distributions by the Gaussian give us four numbers - average (A_s, A_p) and sigma (σ_s ,σ_p) for both distributions. From these numbers we are calculating few variables, which are characterizing operation of the given MAPD in the given conditions. According statistical laws:

$$N_{pix} = \frac{A^2}{\sigma^2} \tag{1}$$

$$U = \frac{\sigma^2}{A} \tag{2}$$

$$SB = \frac{A}{\sigma} \tag{3}$$

where (1) is number of fired pixels, (2) - amplification (ADC bit per one fired pixel), (3) - signal to background ratio, A and σ are the effective average and sigma ($A = A_s - A_p$ $\sigma = \sqrt{\sigma_s^2 - \sigma_p^2}$).

In reality only three measured variables are in the game, A_p is by definition very close to zero. To determine working point for each of MAPD the HV scan should be done starting from the HV where LED light signal is becoming visible till the HV then the MAPD passes the working limit of current. Current limit is set to 1 μa for all examined photo-detectors. In each point of the HV scan the variables listed above are calculated and plotted. Example of such plot is shown on the figure 4.1.2.

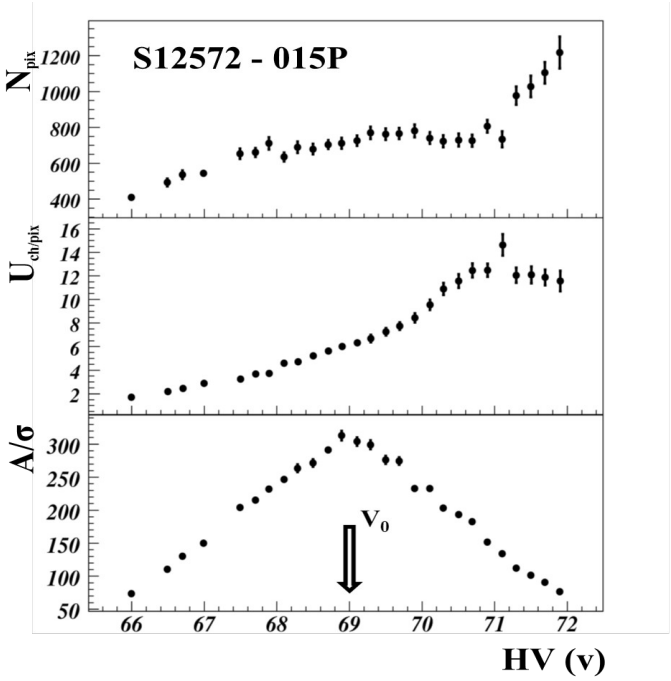

Figure 4.1.2: *MAPD parameters versus HV (one channel)*

From the behavior of the variables on the figure 4.1.2 the choice of the working point is quite evident - best signal to noise ratio around HV= 69V. Later, detector becomes more noisy. At lower

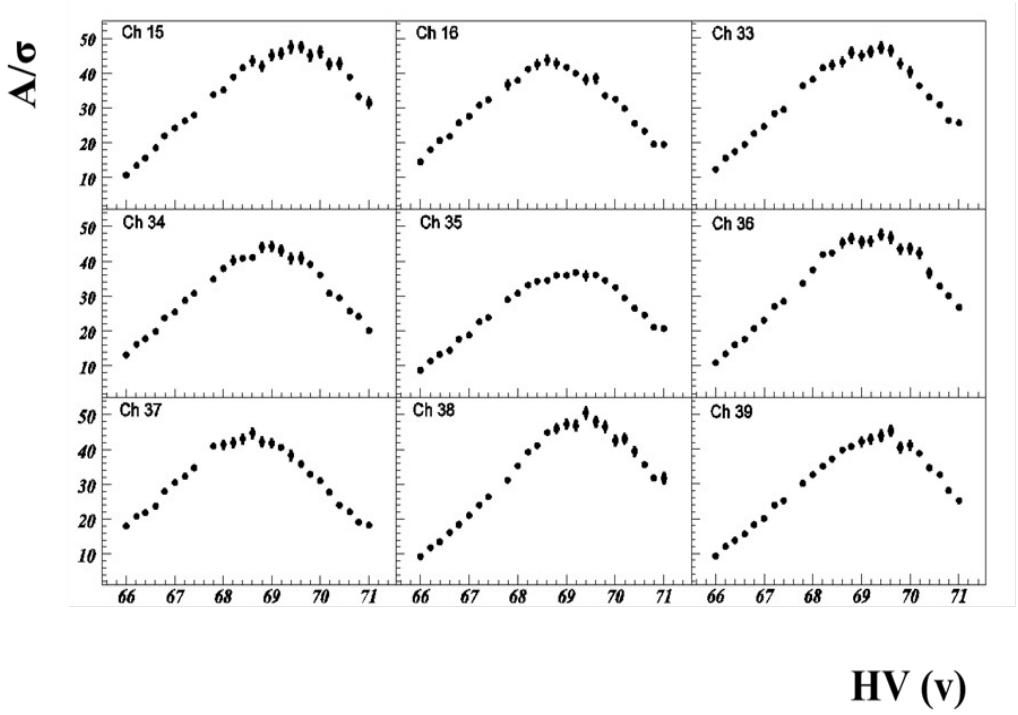

Figure 4.1.3: *Signal to background ration versus HV for the MAPDs of ECal module.*

HV the MAPD amplification is lower, what is also undesirable. The behavior of all MAPD detectors is very similar (Figure 4.1.3 as an example - nine MAPD detectors from one ECal module) and the search of working points can be done almost automatically. Only final control of HV working points search is expected.

4.2 Temperature compensation

Amplification of all MAPD detectors depends from the temperature. To make precise measurements with the devices based on the MAPD detectors we need to stabilize temperature around MAPD or compensate temperature drift of MAPD amplification by the corresponding shift of HV. The dependency of the voltage compensation versus temperature shift is a convolution of two functions - dependency of the MAPD amplification from the temperature (Figure 4.2.1) and the dependency of the MAPD amplification from the HV (Figure 4.2.2). As a result of these measurements linear correction with slope of 0.045V/deg is implemented in the HV source. On the figure 4.2.3 the amplitude of the signal from the LED source is shown as a function of temperature without temperature compensation. While on the figure 4.2.4 the temperature compensation is activated.

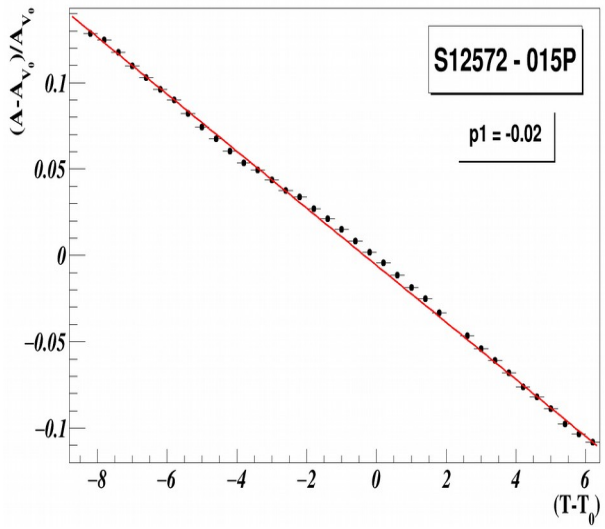

Figure 4.2.1: *Dependency of the MAPD amplification from the temperature.*

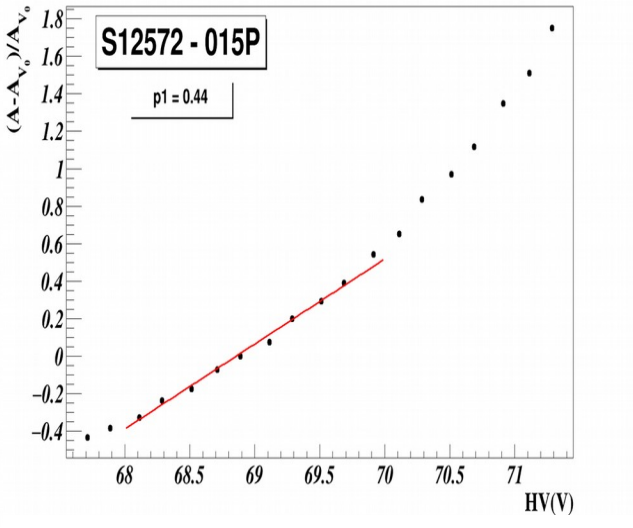

Figure 4.2.2: *Dependency of the MAPD amplification from the HV.*

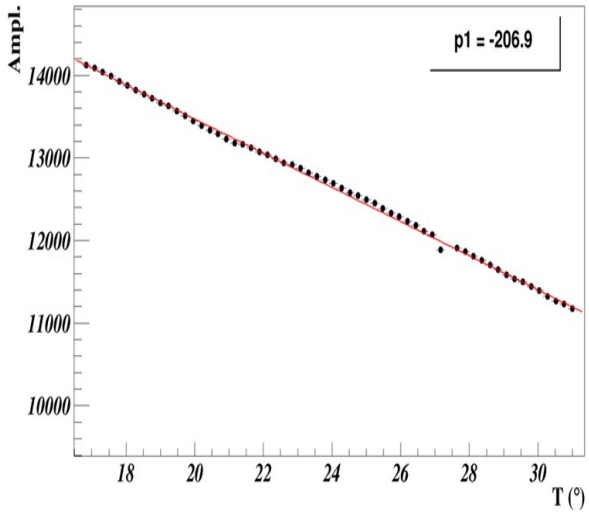

Figure 4.2.3: *Signal amplitude versus temperature (without temperature correction).*

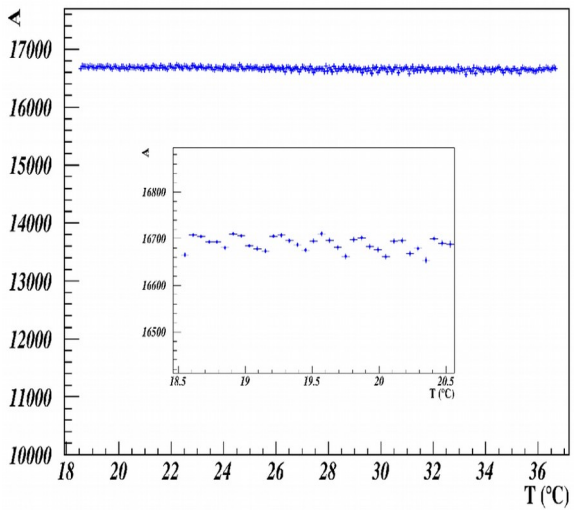

Figure 4.2.4: *Signal amlitude versus temperature (with temperature correction). Zoom inside shows the change of the signal due to one bit (25mV) voltage correction.*

Variation of the signal on the figure 4.2.4 is below 1%, what is quite admissible in our case. Zoom inside figure 4.2.4 illustrating small amplitude variation corresponding to the change of the HV on minimal possible value (1 DAC bit = 10 mV).

4.3 Energy resolution

Many beam tests has been performed during last years. Electron beams available now at CERN and at DESY and both these facilities was used to study MPD ECal.

Advantage of DESY test area is availability and wide electrons energy range (1-6 GeV). At CERN it is possibility to use muons and very small energy spread in the beam.

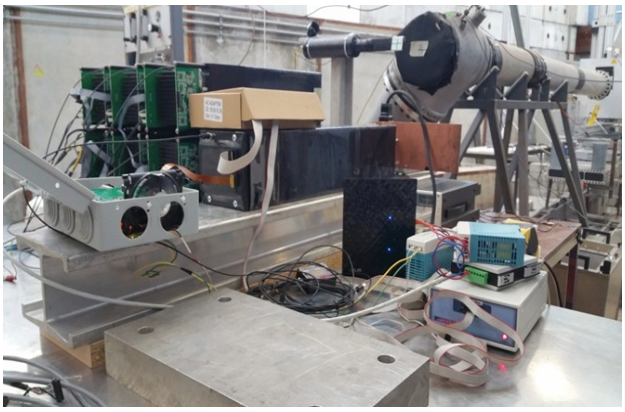

Figure 4.3.1: *Stand with electromagnetic calorimeter in test area in CERN.*

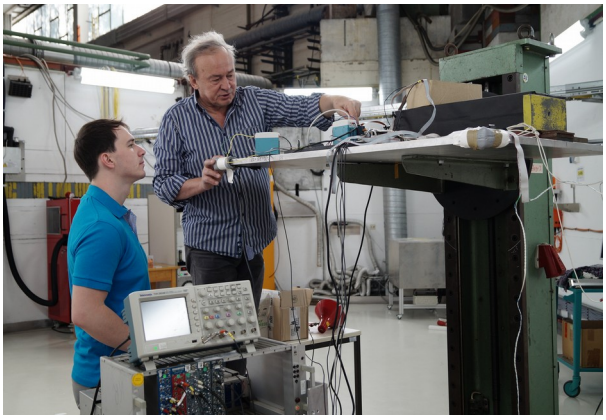

Figure 4.3.2: *Stand with electromagnetic calorimeter in test area in DESY.*

Energy resolution is the most important feature of the ECal was measured at CERN

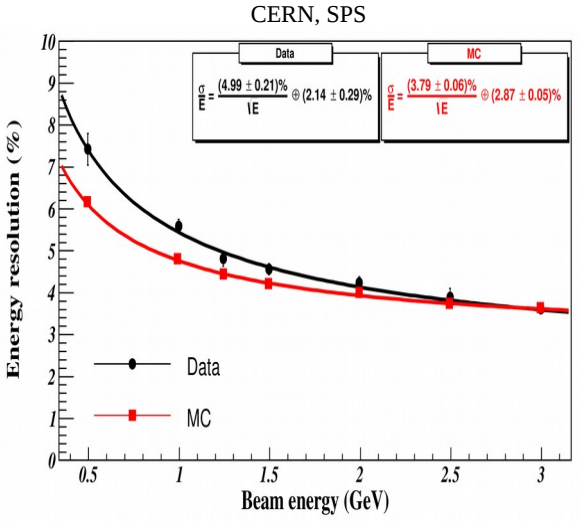

Figure 4.3.3: *Energy resolution vs electron energy for data and MC.*

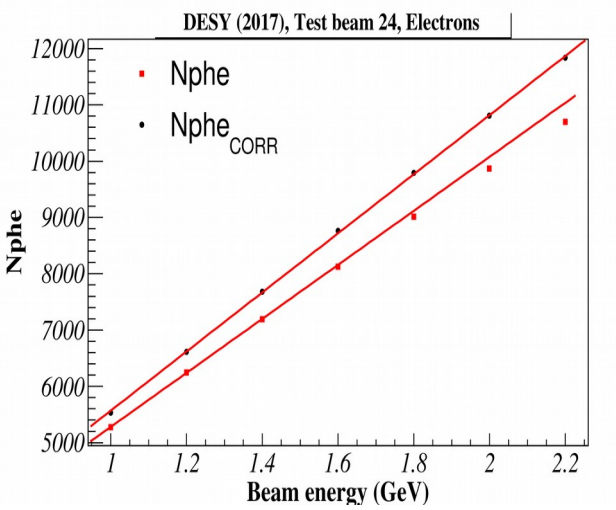

Figure 4.3.4: *Detector response to the hitting electrons of different energies.*

(Figure 4.3.3). Experimental results are slightly worse of the MC expectations in the energy region below 2 GeV. The reason of this disagreement is the matter for the future study.

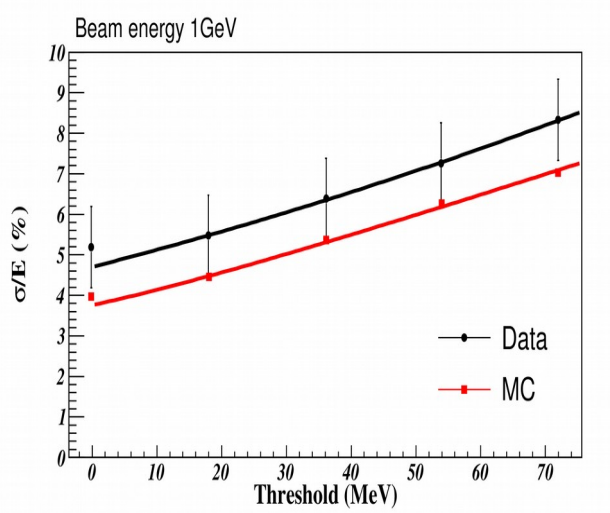

Figure 4.3.5: *Energy resolution versus threshold.*

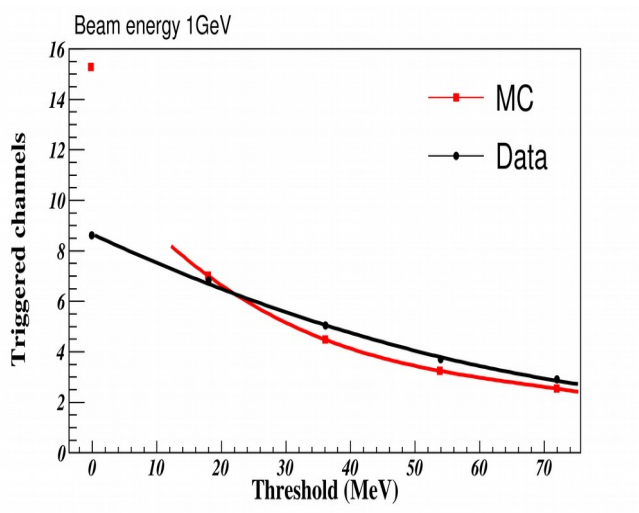

Figure 4.3.6: *Triggered channels versus threshold.*

The test was done to make a choice of the registration threshold for the DAQ electronics. Here the choice is a compromise between better energy resolution for the low threshold (Figure 4.3.5) and

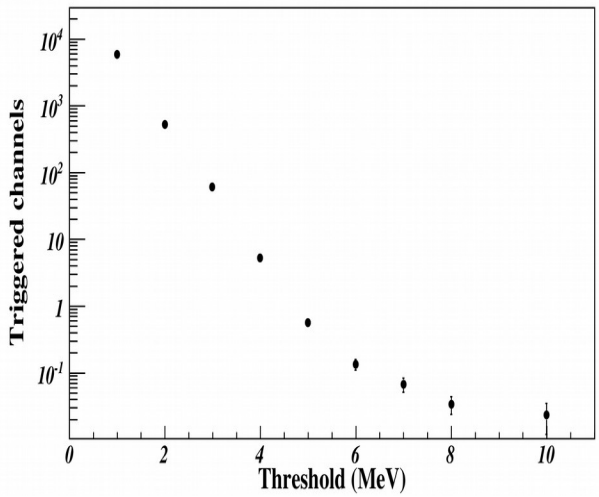

Figure 4.3.7: *Number of noise channel per event for the whole ECal (40230 channels) versus threshold.*

reduction of number of active channels per particle, reduction of data flow per events, reduction of number of noise hits in the case of increase of the registration threshold (Figure 4.3.6). From the data shown in figure 4.3.7 we conclude that threshold in our case should be in the region 5-10 MeV. Further reduction of the threshold does not improve energy resolution too much, but increasing

number of hits per shower a lot with all negative consequences.

Calorimeter responses to the incident muon. 0.5 GeV electron and 3 GeV electron are shown in the figure 4.3.8 and figure 4.3.9. Slightly wider spectra in the low energy region is seen here as it is follow from the figure 4.3.3.

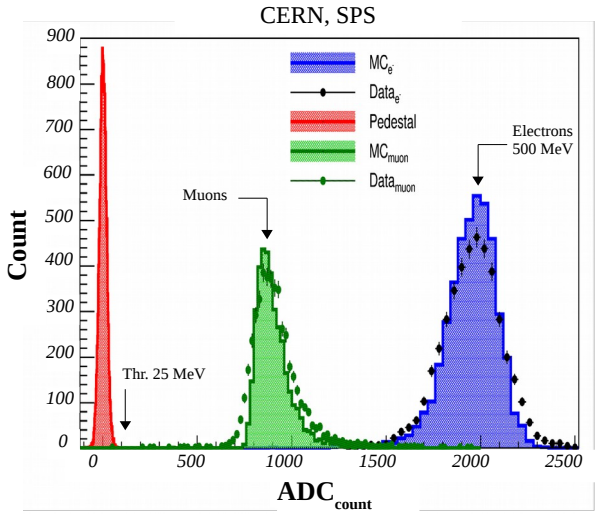

Figure 4.3.8: *Signal spectrum for the pedestal, muons, electrons 0.5GeV.*

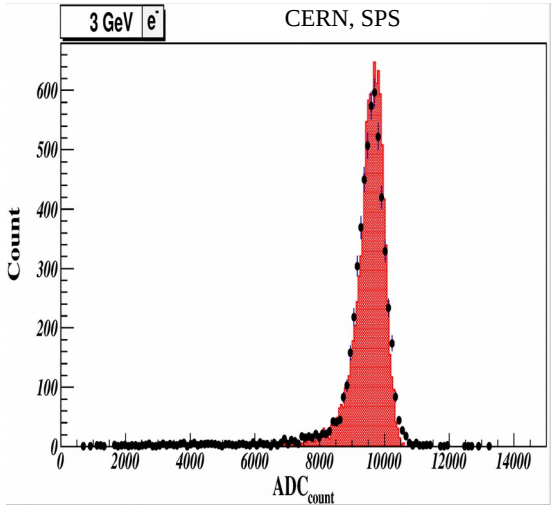

Figure 4.3.9: *Signal spectrum for electrons 3GeV.*

As it is clear from the figure 4.3.8 MIP energy deposition is much higher than the noise of electronics (pedestal) and such particles can be effectively restarted by the calorimeter. Electronics threshold clearly can be set below 25 MeV. To choose electronics threshold more precisely the special tests was done Figure 4.3.7. The time window in this test have been chosen quite wide - 5 time bins (100 ns). These tests is used to choose a compromise value of the threshold, low enough to obtain good energy resolution and high enough to reduce the number of triggered channels (both real and noise).

The calorimeter modules were tested on the beam of the Nuclotron in the installation of the BM@N. A scintillation counter has been used to allocate primary hadrons and their spectra are presented in figure 4.3.10 and figure 4.3.11. The background of the graphs is associated with the inefficient allocation of primary hadrons. Despite considerable background data and MC agreement is quite good.

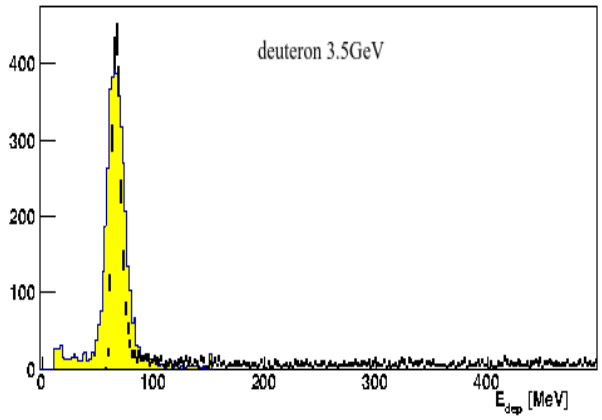

Figure 4.3.10: *Detector response to deuterium.*

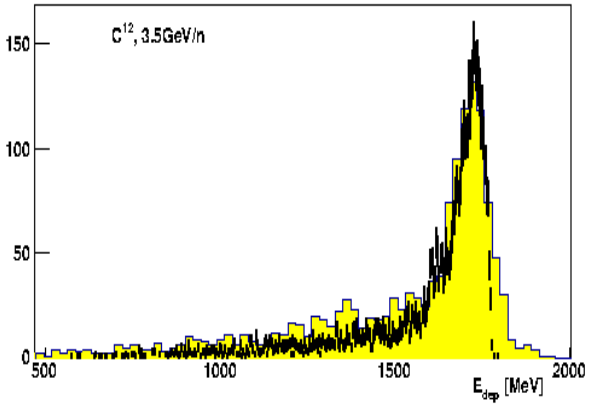

Figure 4.3.11: *Detector response to C^{12}.*

4.4 Time resolution

The tests of time resolution of the calorimeter using various type of electronics have been performed. The results of previous studies (Figure 4.4.1 and Figure 4.4.2) have been confirmed . It is shown that the dependence of time resolution from the number of registered photoelectrons

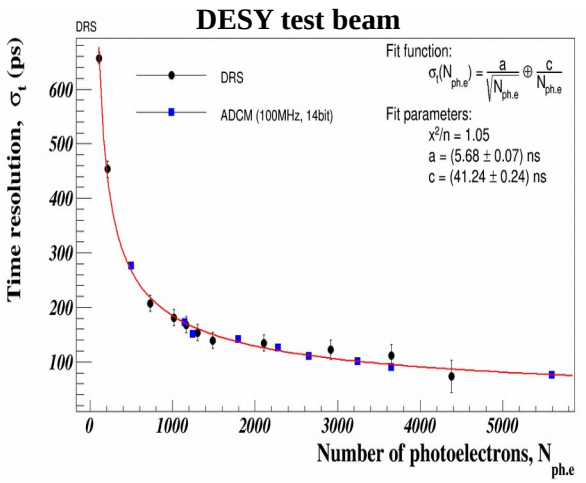

Figure 4.4.1: *Time resolution vs number of detected photoelectrons measured with different methods and different electronics. Time bin: DRS -200 ps [36] and ADCM-10ns [37].*

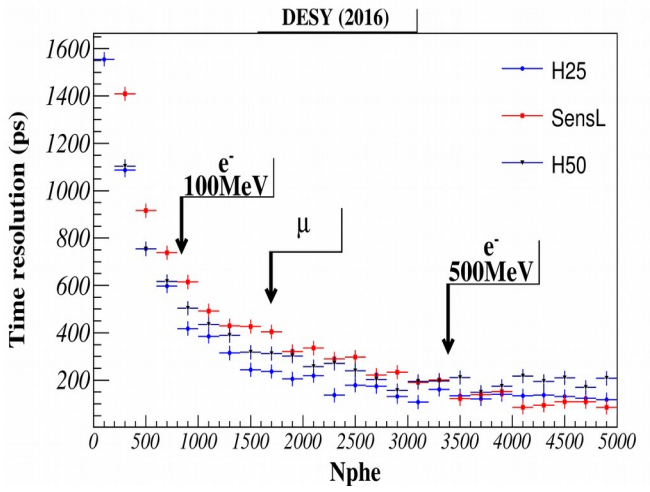

Figure 4.4.2: *Time resolution vs number of detected photoelectrons of different photo-detectors.*

displays the properties of the calorimeter but not the effect of electronics channel. As a result we are expecting time resolution for the MIP on the level of 150 ps.

4.5 Coordinate resolution

Calorimeter prototypes tests done at DESY discovered another unexpected feature - sampling of proposed for MPD calorimeter allow quite accurate measure the position of electromagnetic shower. For the first time the possibility of precise measurements of coordinates of particles in the calorimeter was studied (Figure 4.5.1). It was shown that the response function of the calorimeter at coordinate is not linear. The deviation from linearity is very close to sinusoidal with zeros in the center and at the edges of the module (Figure 4.5.2). The possibility to correct this nonlinearity (Figure 4.5.3) and to achieve a coordinate resolution on level 4-1 mm (Figure 4.5.4) depending on the energy deposited in the electromagnetic shower have been demonstrated.

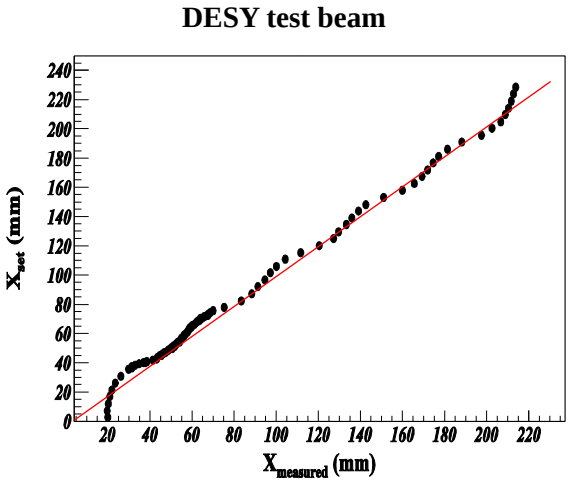

Figure 4.5.1: *Correlation between set and measured coordinates.*

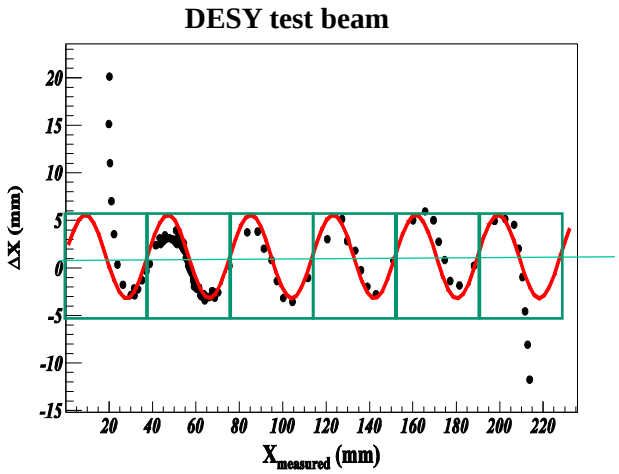

Figure 4.5.2: *Deviation of the measured coordinates from the linear dependence.*

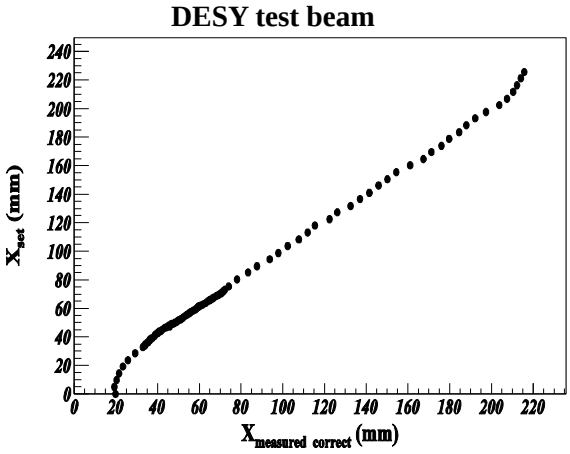

Figure 4.5.3: *Correlation between set and measured coordinates – after corrections.*

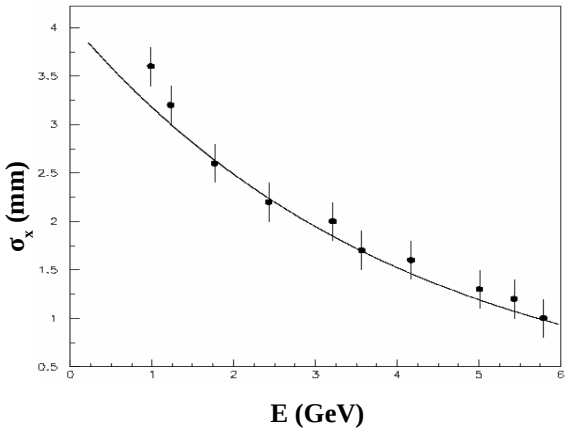

Figure 4.5.4: *Space resolution versus energy of electromagnetic shower.*

4.6 Heat extraction

Special attention we pay to the problem of heat extraction from the MPD barrel due to the possible influence of the mistakes in this operation on the operation not only ECal detector but also on the all detectors around. To verify the ideas which are placed in the basis of the ECal heat extraction system we have carried out tests with prototype of such system. Boards with resistors have been distributed along the ventilation duct to simulate the real electronics. Power supply is able to assure production of heat in the wide region, but for tests we have used current producing roughly twice more heat than it is expected in the real experiment. Temperature sensors was used to registrate with high accuracy temperature of the air on the input and output of the ventilation duct. One temperature sensor located far away from the heating part of setup was used as a reference , and one to measure the temperature of the outer wall of the ventilation duct. Air flow and pressure was steered through the electronic valves connected to the computer.

Results are shown on the figure 4.6.2 and figure 4.6.3 for two different intensities of air flow inside the ventilation duct. In both cases first 300 s the ventilation was not activated and temperature inside the ventilation duct was going up. After 300 s ventilation was activated an temperature starts to go down along all channel of ventilation. Minimal air flow through the one ECal sector which

guarantees normal conditions inside all duct is estimated 1000 l/min.

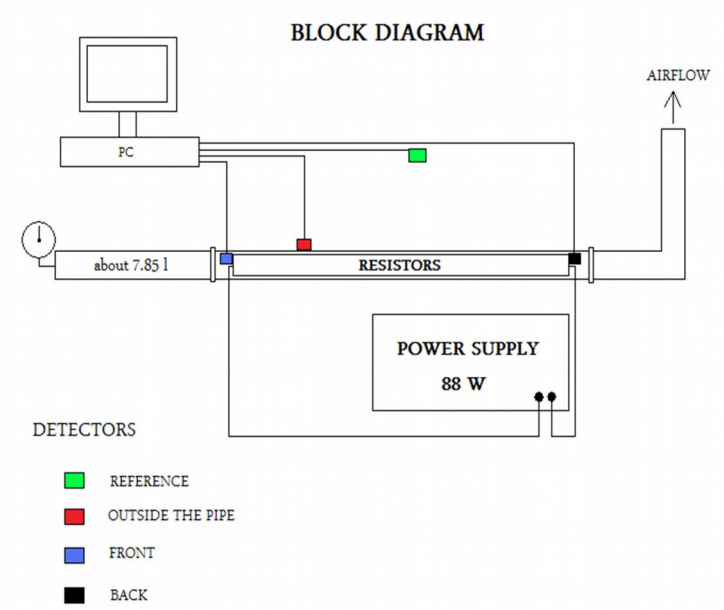

Figure 4.6.1: *Prototype set up of hit extraction system.*

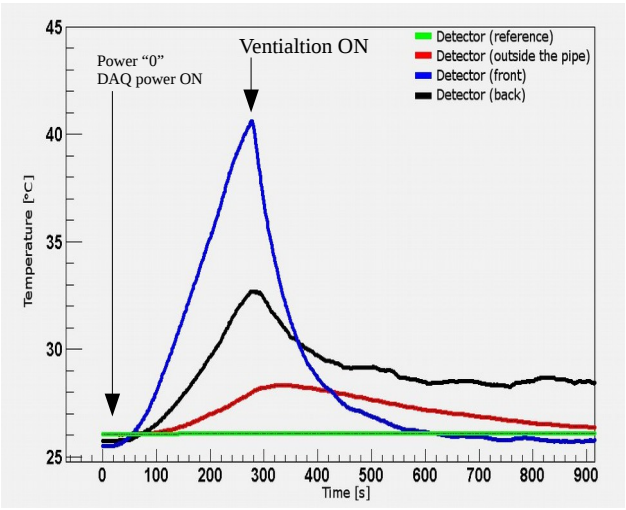

Figure 4.6.2: *Temperature dependency in different points of test set up versus time. Slow ventilation (AirFlowVelosity 2 m/s = 16 l/s).*

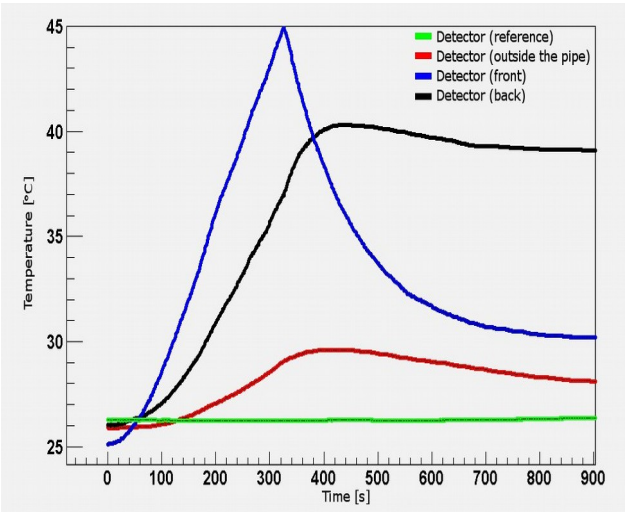

Figure 4.6.3: *Temperature dependency in different points of test set up versus time. Faster ventilation (AirFlowVelosity 1.2 m/s = 9.6 l/s).*

In the test set-up the size of the inlet pipe is about 4 cm^2. To have a guaranteed cooling and even some spare power in the cooling system size of inlet-outlet pipes can be increased up to 10 cm^2. This size easily fit dedicated to ECal space in the cable holes in the detector body.

5 Projective geometry

5.1 Fundamentals of the Design of the ECal

The change of the calorimeter design to the with a projective arrangement of the modules (Figure 5.1.1 and Figure 5.2.2) led to several important consequences. Improving the performance of the calorimeter, the emergence of additional stiffening elements in the form of a honeycomb, the possibility of placing additional components on the edges of the sectors. There is a need to make some changes in the module design, redesign readout electronics.

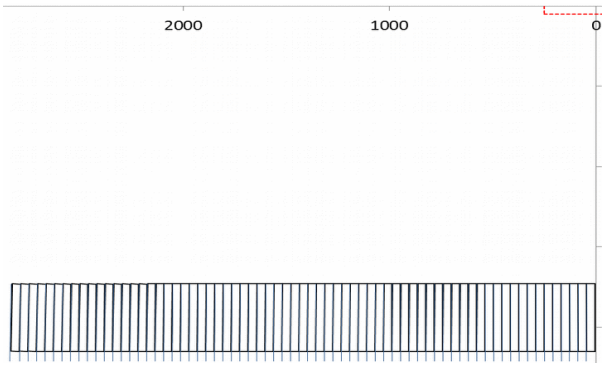

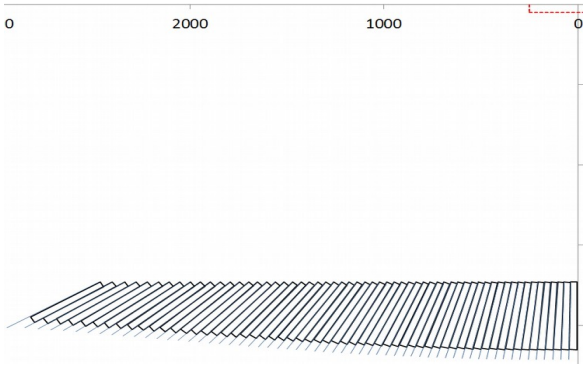

Figure 5.1.1: *Z plane of the no projective geometry.* **Figure 5.1.2:** *Z plane of the projective geometry.*

Calculations have been made on the choice of the angle of inclination for the modules. The aim of the calculations is to select a single for all modules tilt angle at which the deviation of the aiming

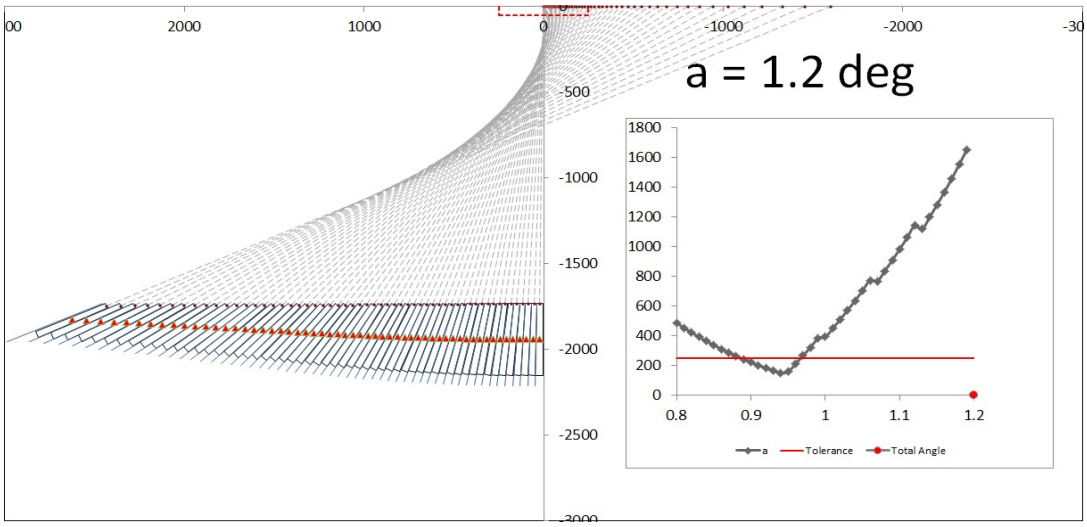

Figure 5.1.3: *Optimization of the location of ECal modules in the Z plane (a = 1.2 deg).*

point from the center of the MPD will be minimal (Figure 5.1.3 and Figure 5.1.4).

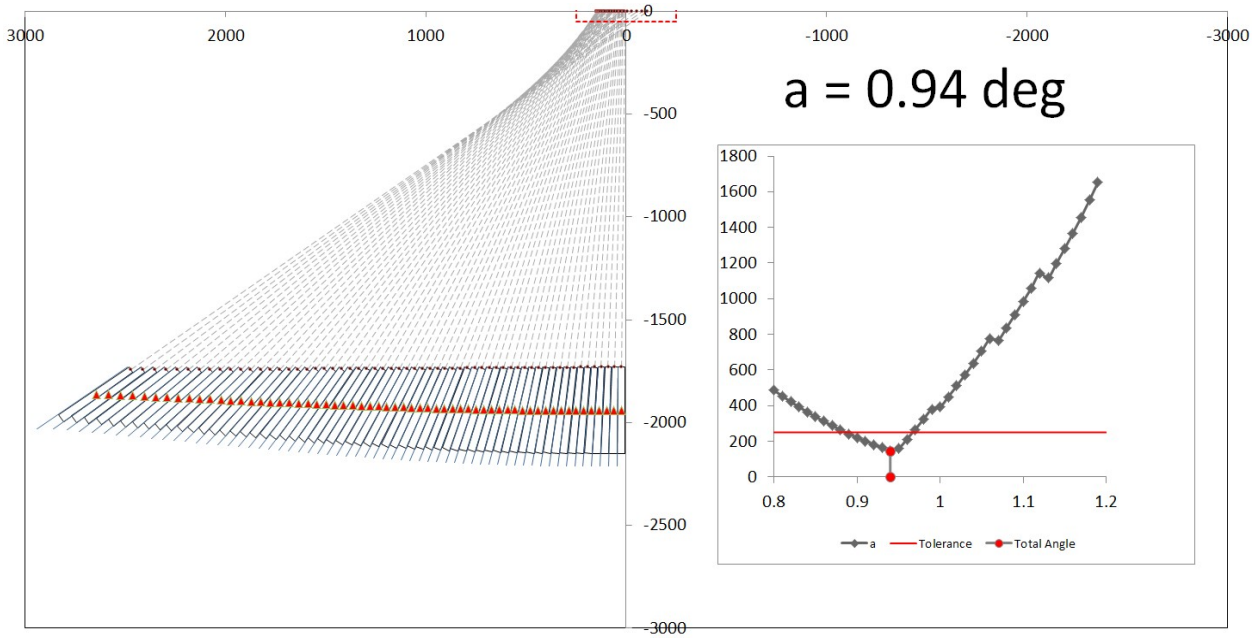

Figure 5.1.4: *Optimization of the location of ECal modules in the Z plane (a = 0.94 deg).*

Despite the fact that the minimum deviation is achieved when the tilt angle is 0.94 degrees, for simplicity it was decided to adopt this angle as 0.9 degrees.

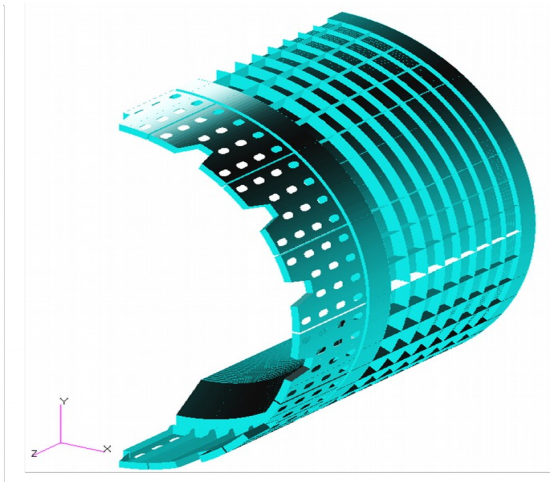

Figure 5.1.5: *Organization of the power structures fixing sectors.*

Calorimeter modules are collected in the cassette of 16 units - 2 rows of 8. Such a segmentation is not fundamentally important, these numbers are selected for easier organization of electronics readout. The primary support structure is the pencil case, which consist of the mounting plate and honeycomb structure. Honeycomb have a thickness of about 0.3 mm, which ensures sufficient rigidity of the entire structure and has no significant impact on the characteristics of the calorimeter. Mounting plate provides a rigid connection of honeycomb, filled by the calorimeter modules, and the next structure element - the block. Inside the mounting panel is reserved enough space for the electronic board serving all 16 channels of the calorimeter which are supported by one panel.

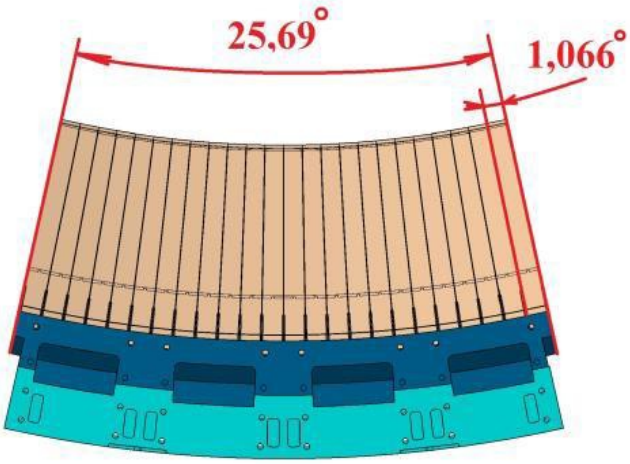

Figure 5.1.7: *One block.*

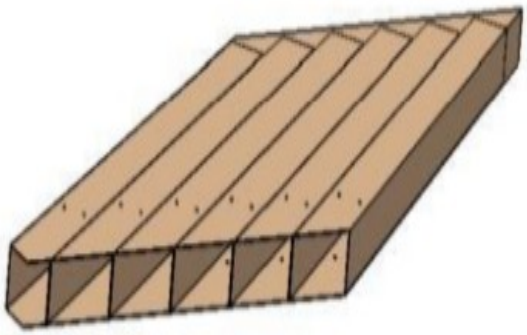

Figure 5.1.8: *The honeycomb structure.*

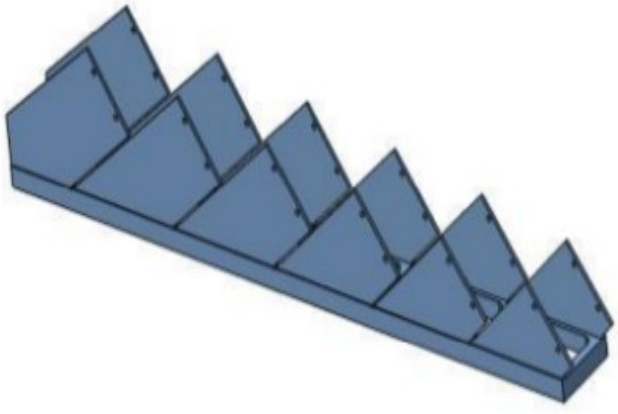

Figure 5.1.9: *The mounting plate (supporting frame).*

Figure 5.1.10: *The ECal module.*

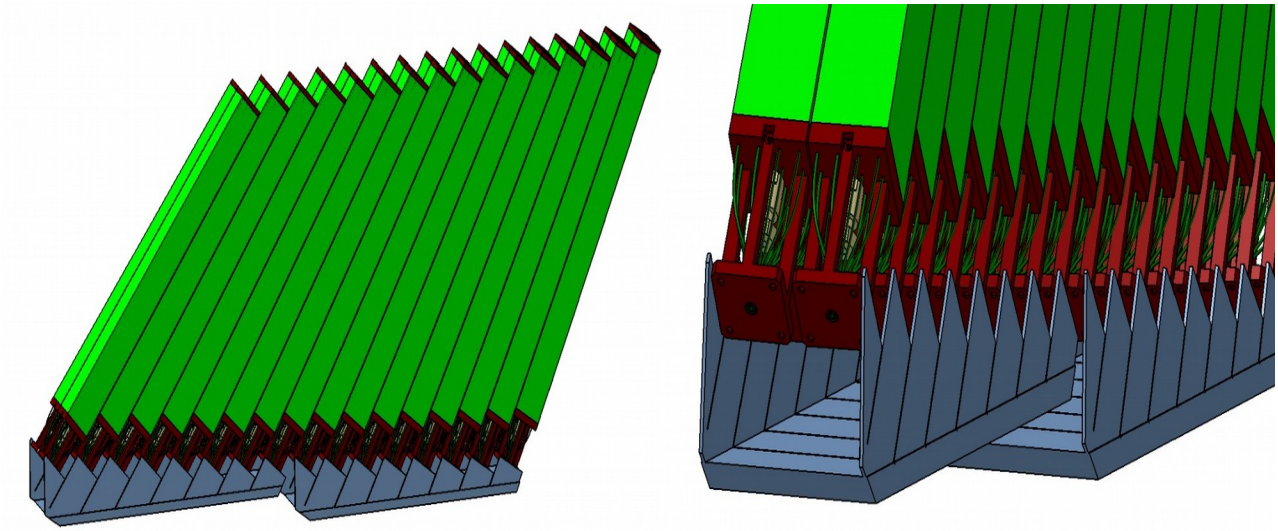

Figure 5.1.11: *Assembled unit.*

The block consists from 2 and 4 cassettes in the longitudinal dimension and 12 cassettes in the transverse dimension. Three types of blocks are distinguished from each other by its geometry, which varies with distance from the detector center. These three blocks are form pro-sector with 1536 calorimeter modules, as shown in figure 5.1.12.

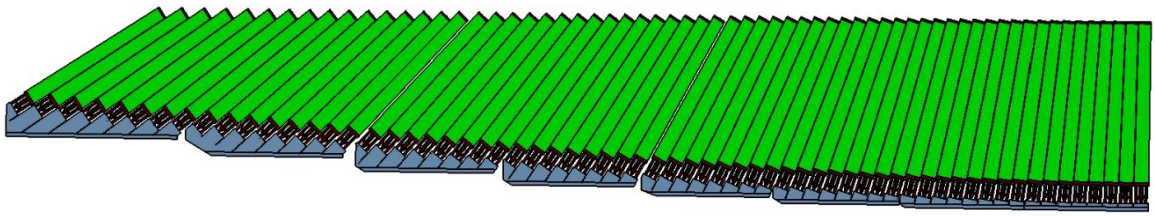

Figure 5.1.12: *One pro-sector.*

Each block is mounted on a rigid base (Figure 5.1.13), for the external blocks this base is even reinforced by stiffeners (Figure 5. 1. 14).

Figure 5.1.13: *Base of central block.*

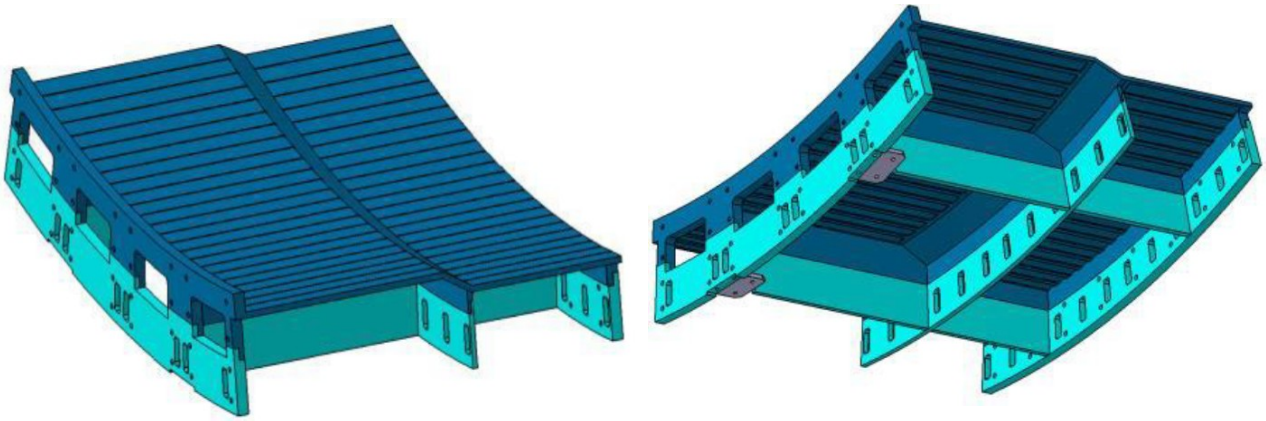

Figure 5.1.14: *Base of side blocks.*

The inner surface of each block closed by the reinforced panel which later (after Assembly of the calorimeter) will form the internal power cylinder of the calorimeter. The side surface of the block

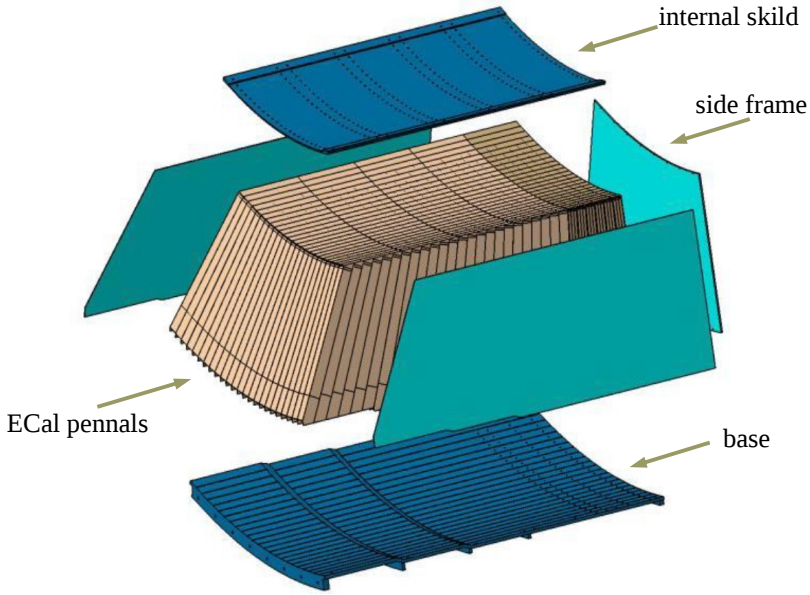

Figure 5.1.15: *Power structure element.*

closed by the panel which is also the power structure element (Figure 5.1.15). Assembling of the calorimeter sector is produced on the frame (Figure 5.1.17) starting from the inner blocks and ended by the outer blocks (Figure 5.1.16).

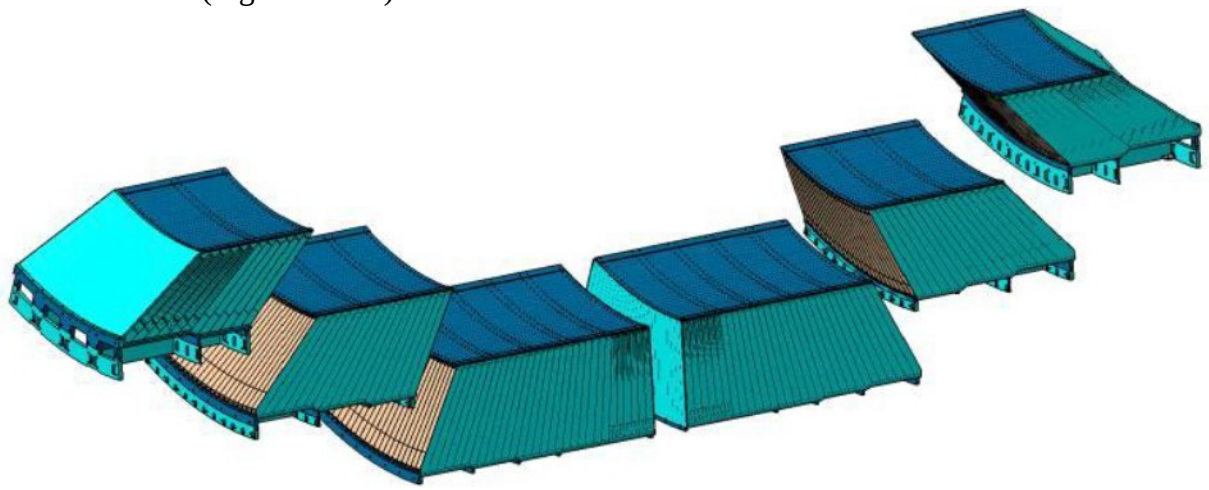

Figure 5.1.16: *Implantation of the modules.*

Figure 5.1.17: *Frame of the sector.*

After assembling sector is a single element with the necessary rigidity to enable transportation to the place of assembling of the calorimeter and manipulation during calorimeter assembling (Figure 5.1.18).

Figure 5.1.18: *The sector is ready for introduction.*

5.2 Block assembling

Assembling is going on the turning slipway (Figure 5.2.1). The assembling procedure includes both mechanical Association of modules of the calorimeter and installation of electronics and testing in conjunction with the modules of the calorimeter.

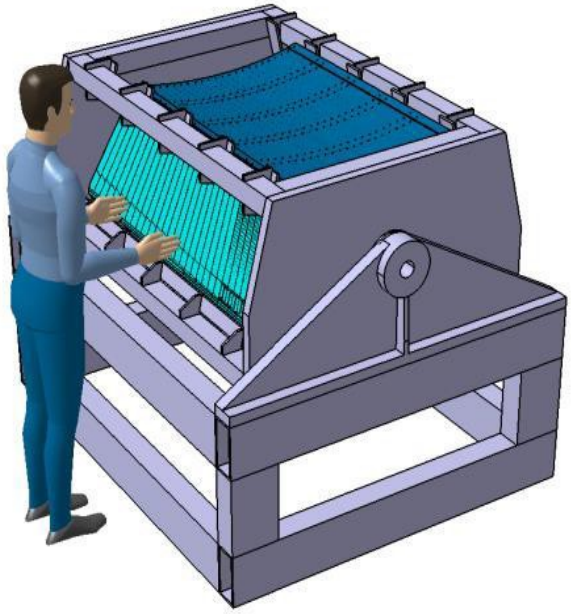

Figure 5.2.1: *The turning slipway.*

Outer screen of the block, which is part of the power structure supporting the 70-ton calorimeter, is installed in the first place (Figure 5.2.2).

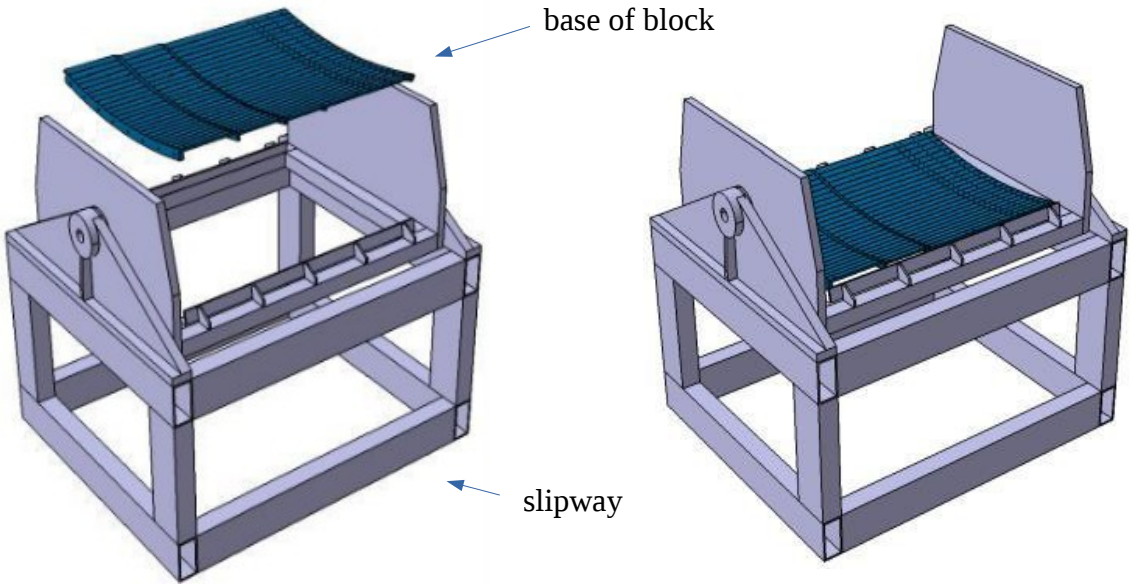

Figure 5.2.2: *The turning slipway.*

Next is the sequential installation of the ECal modules at the base of the block.

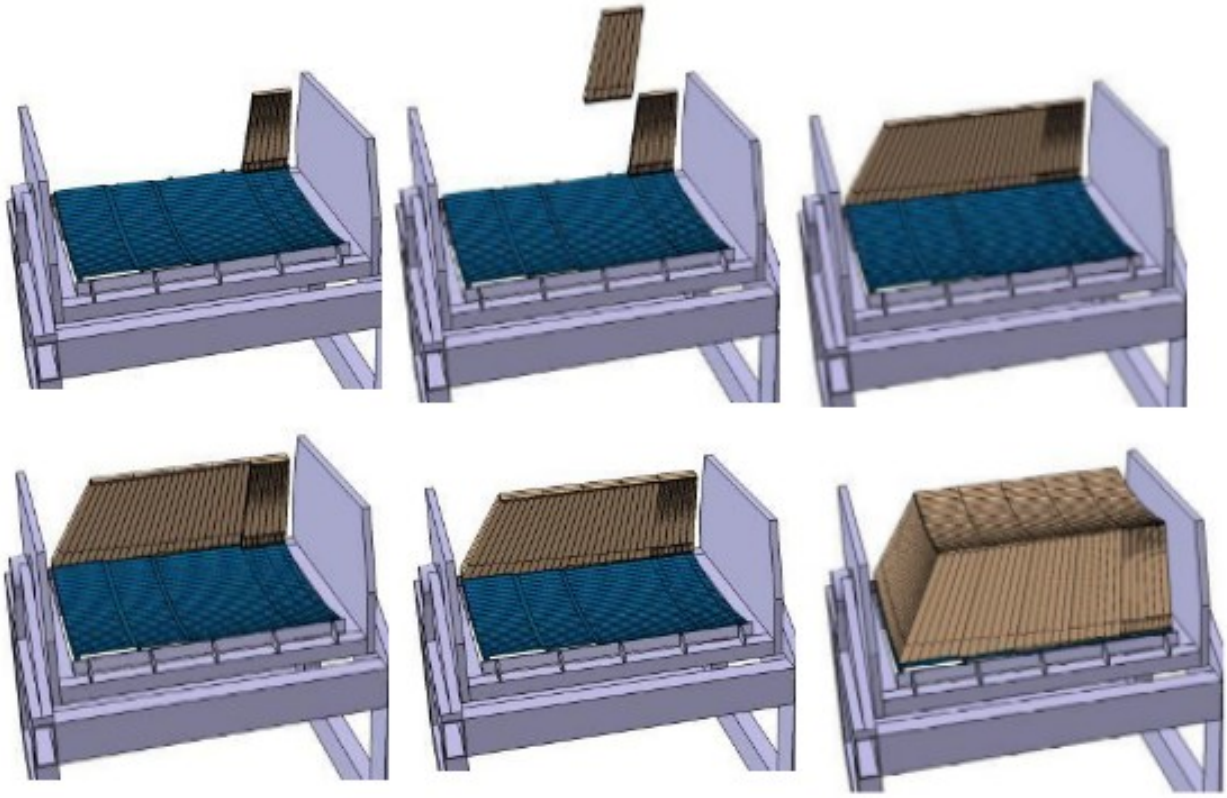

Figure 5.2.3: *Assembling stages.*

The pinning of the cassettes is provided by installation of the panels, which are further bolted to the base of the unit.

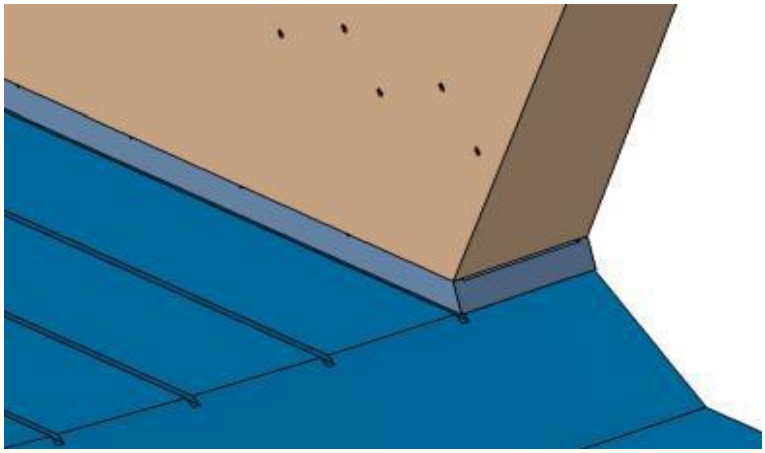

Figure 5.2.4: *Mounrika plate.*

After installing all of the cassettes unit are installed side walls, the inner shell and the frames. This allows to flip the unit 180 degrees.

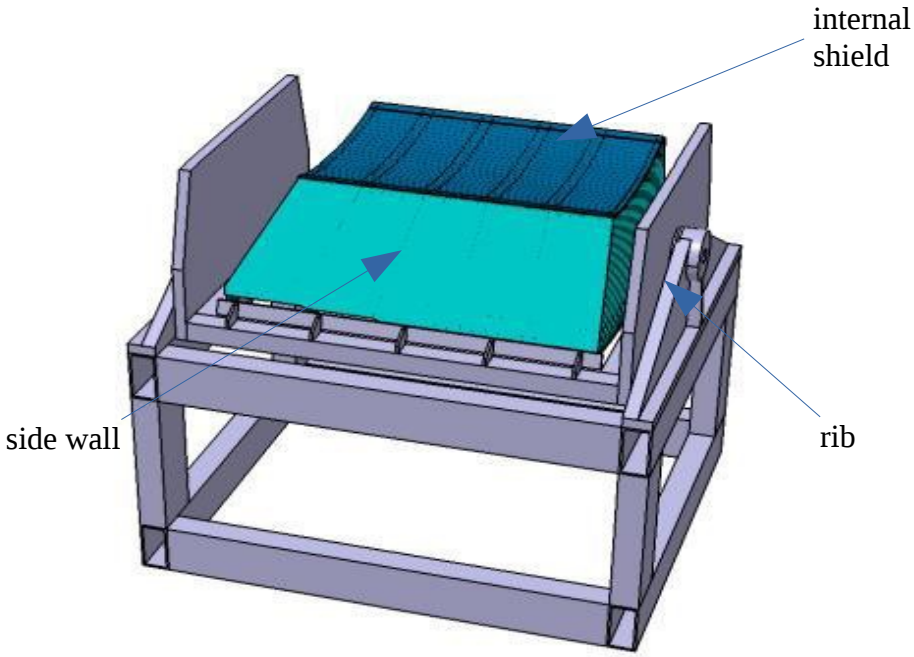

Figure 5.2.5: *Stand collection module.*

The upper frame has a supporting surface, which preclude the lowering of the cassettes upon rotation of the block.

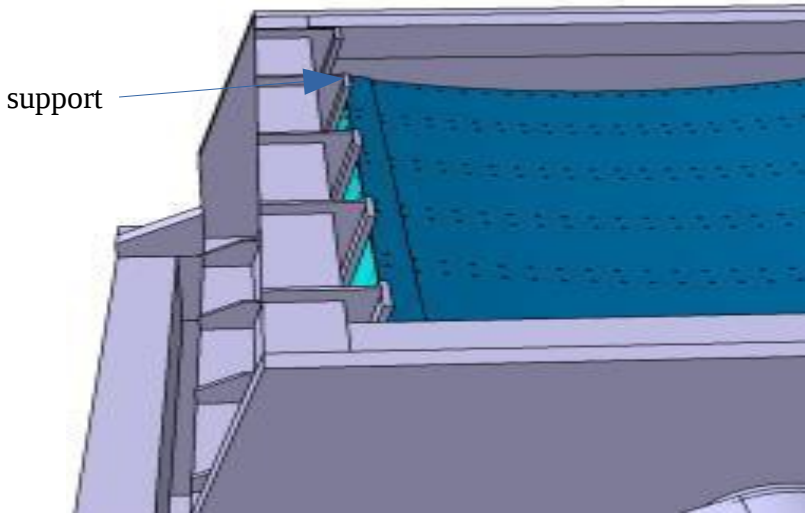

Figure 5.2.6: *The upper frame with supporting surface.*

Next, turn the block ECal on 180 degrees.

Figure 5.2.7: *Rotation of the block.*

After rotating the block using the frame of the turntable as the beam, dismantle the unit from the fixture for further assembling in the sector and the installation in the transport container.

5.3 Sector assembling

In the assembling of ECal blocks in the sector use transportation containers. The blocks are installed from the edges to the center from two sides.

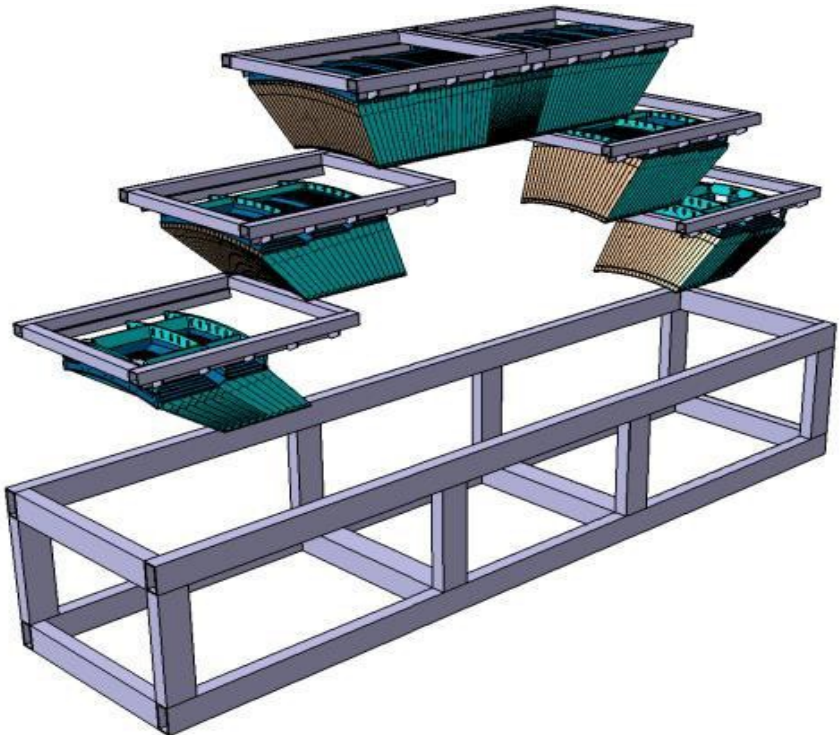

Figure 5.3.1: *The transportation containers.*

Before installing the blocks, the shipping container side walls are set in the sector.

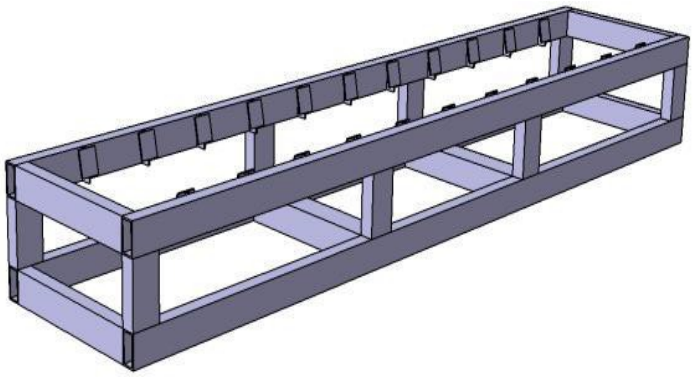

Figure 5.3.2: *The transportation containers.*

After that, the download of external blocks of ECal.

Figure 5.3.4: *Up down.*

After connecting the blocks with the side walls of the sector and their fixing to the transport container is carried out dismantling of the frame of the turntable. The same procedure are carried

out with blocks 2 and 3.

Figure 5.3.5: *Blocks 2 and 3.*

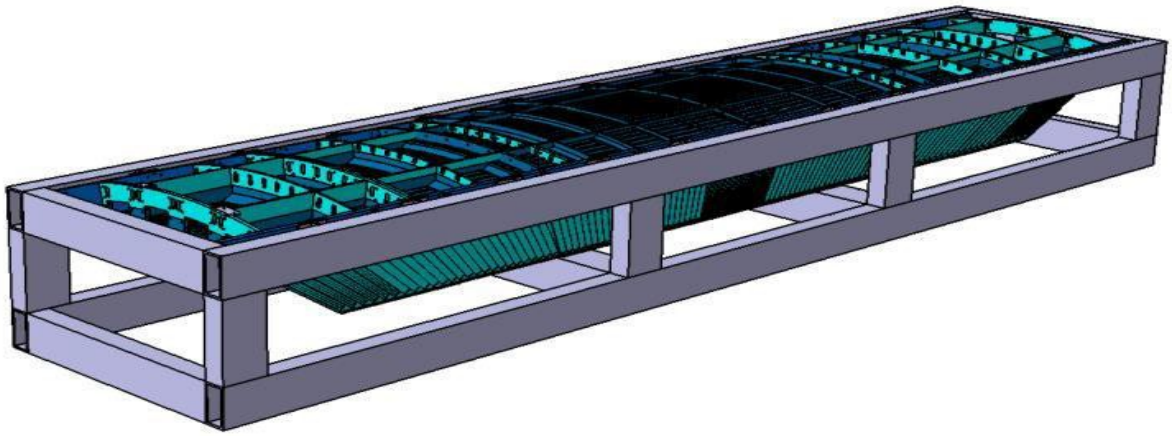

Figure 5.3.6: *All sector.*

After assembling of the blocks in the sector ECal it is possible to make final installation of the electronics.

6 Time table and cost estimation

First stage of ECal construction is include period till 2020 and will cost about 16378.61k$.

Task Name	Total (k$)	2015				2016				2017				2018				2019				2020			
		I	II	III	IV	I	II	III	IV	I	II	III	IV	I	II	III	IV	I	II	III	IV	I	II	III	IV
ECal sector design																									
Detector R&D, prototyping	100.00																								
FEE R&D and prototyping	50.00																								
Pilot modules production and test	70.00																								
Slow Control R&D and prototyping	7.63																								
Infrastructure	352.62																								
Sectors assembling line test	10.00																								
ECal modules mass production	4 991.51																								
Pilot sector production, test	5.00																								
ECal sector mass production	900.00																								
Detector head production	3 200 .00																								
FEE production	4 691.51																								
Slow control production	1 400.00																								
ECal Cooling system production	300.00																								
ECal installation	150.00																								
Commissioning of ECal	150.34																								
Total (2015-2020): 16.4M$	16 378.61																								

R&D, Design, Prototyping	227.63	2010 - 2018
Production Cost	15 497.98	2016 - 2020
Infrastructure Cost	653.00	2016 - 2018
Total (k$):	16 378.61	

. Reference

[1] The MultiPurpose Detector – MPD to study Heavy Ion Collisions at NICA (Conceptual Design Report), Version1.4.

[2] G. Trubnikov, A. Kovalenko, V. Kekelidze, I. Meshkov, R. Lednicky, A. Sissakian, A. Sorin, PoS (ICHEP 2010) 523.

[3] G. Trubnikov, N. Agapov, V.Kekelidze, A. Kovalenko, V. Matveev, I.Meshkov, R. Lednicky, A. Sorin, PoS 36th International Conference of High Energy Physics (ICHEP2012), July 4-11,Melbourne, Australia.

[4] V.Kekelidze, A. Kovalenko, R. Lednicky, V. Matveev, I.Meshkov, A. Sorin, G. Trubnikov, 37th International Conference on High Energy Physics, ICHEP 2014, Valencia, Spain, 2 Jul 2014 - 9 Jul 2014 Nuclear physics B Proceedings supplements (2014).

[5] C. Alt et al, Phys. Rev. C77, 024903 (2008).

[6] R. Rapp and J. Wambach, Adv. Nucl. Phys. 25, 1 (2000).

[7] G.E. Brown and M. Rho, Phys. Rev. Lett. 66, 2720 (1991).

[8] A. A. Anselm and M. G. Ryskin, Phys. Lett. B266, 482 (1989).

[9] J.-P. Blaizot and A. Krzywicki, Phys. Rev. D46, 246 (1992).

[10] G. Agakichiev et al. (CERES Collaboration) Phys. Lett. B 422 (1998) 405.

[11] D. Adamova et al. (CERES Collaboration) Phys. Rev. Lett. 91 (2003) 042301.

[12] G. Agakichiev et al. (CERES Collaboration) Eur. Phys. J. C 41 (2005) 475.

[13] D. Adamova et al. (CERES Collaboration) Phys. Lett. 666 (2008) 425.

[14] R. Arnaldi et al. (NA60 Collaboration) Phys. Rev. Lett. 2006. V.96. P.162302.

[15] A. Adare et al. (PHENIX Collaboration) Phys. Rev. C. 2010. V.81. P.034911.

[16] F. Geurts, Di-Lepton Physics Program at STAR. Quark Matter 2012 Conference.

[17] R.J. Porter et al. (DLS Collaboration) Phys. Rev. Lett. 79 (1997). 1229.

[18] A. Rustamov et al. (HADES Collaboration)} Int. Jour. Mod. Phys. A 26, 384.

[19] J. Randrup and J. Cleymans, Phys. Rev. C 74 (2006) 047901.

[20] D. Kharzeev,Phys. Lett. B633, 260 (2006).

[21]Y. Burnier, D. E. Kharzeev, J. Liao, and H.-U. Yee, Phys. Rev. Lett. 107, 052303 (2011)

[22]L. Adamczyk et al (STAR Collaboration), Phys. Rev. Lett. 114,252302 (2015)

[23] J. C. Dunlop, M. A. Lisa, and P. Sorensen, Phys. Rev. C84, 044914 (2011).

[24] J. Xu, L.-W. Chen, C. M. Ko, and Z.-W. Lin, Phys. Rev. C85, 041901 (2012).

[25]. T. Csorgo, Journal of Physics Conferences Series 50(1):259, November 2006.

[26] D.K.Srivastava and J.I.Kapusta, Phys. Rev. C 48, 1335(1993).

[27] A.Timmermann, M.Plumer, L.Razumov and R.M.Weiner,Phys.Rev.C 50, 3060(1994).

[28] J.Alam, B.Mohanty, P.Roy, S.Sarkar and B.Sinha, Phys. Rev. C 67, 054902(2003).

[29] I.Chirikov-Zorin et al, Part.Nucl., Lett 11(2014) 412-417

[30] G. Atoian et al., Nucl.Instrum.Meth. A531, 467 (2004).

[31] G. Atoian et al., Nucl.Instrum.Meth. A320, 144 (1992).

[32] L. Aphecetche et al., NIM A499, 521 (2003).

[33] S. Barsuk, in XI Int.Conf. Calorimetry in High Energy Physics, Italy, 2004.

[34] D. Karlen et al., Nuclear Physics B 159, 91 (2006).

[35] http:// www.hamamatsu.com

[36] http://psi.ch/drs/

[37] http://afi.jinr.ru/